DEVELOPMENT AND EVALUATION OF AN HMA FRACTURE MECHANICS BASED MODEL TO PREDICT TOP-DOWN CRACKING IN HMA LAYERS

By

JIAN ZOU

A DISSERTATION PRESENTED TO THE GRADUATE SCHOOL
OF THE UNIVERSITY OF FLORIDA IN PARTIAL FULFILLMENT
OF THE REQUIREMENTS FOR THE DEGREE OF
DOCTOR OF PHILOSOPHY

UNIVERSITY OF FLORIDA

2009

To my wife and parents

ACKNOWLEDGMENTS

It is a great pleasure for me to thank and acknowledge the many individuals who assisted and supported me during the course of my doctoral program. First of all, I would like to express my sincere appreciation to my committee chairman, Dr. Reynaldo Roque for his invaluable guidance and support throughout my studies at the University of Florida. I would not have been able to reach this milestone if it was not for his advice and understanding. I would also like to express my gratitude to other committee members, Dr. Dennis R. Hiltunen, Dr. Mang Tia, and Dr. Bhavani V. Sankar, for their support in accomplishing my work.

Many thanks should also be given to all former and current colleagues in the material and geotechnical group for their help and friendship during my stay in the Department of Civil and Coastal Engineering at the University of Florida.

I would also like to express my appreciation to the Federal Highway Administration and the Florida Department of Transportation for the ongoing financial support to the study of top-down cracking.

And lastly, I would like to thank my parents for understanding and supporting my long pursuit of the Ph.D. degree, and special thanks to my wife, Lin Du and her parents for support and enduring love.

TABLE OF CONTENTS

LIST OF TABLES

LIST OF FIGURES

Abstract of Dissertation Presented to the Graduate School
of the University of Florida in Partial Fulfillment of the
Requirements for the Degree of Doctor of Philosophy

DEVELOPMENT AND EVALUATION OF AN HMA FRACTURE MECHANICS BASED MODEL TO PREDICT TOP-DOWN CRACKING IN HMA LAYERS

By

Jian Zou

December 2009

Chair: Reynaldo Roque
Major: Civil Engineering

It is well recognized that load-related top-down cracking commonly occurs in HMA pavements. This phenomenon has been reported to occur in many parts of the United States, as well as in Europe, Japan, and other countries. This mode of failure, however, cannot be explained by traditional fatigue mechanisms used to explain fatigue cracking that initiates at the bottom of the pavement. The primary objective of this research is therefore to identify the causes of top-down cracking and to develop mechanistic-based models for predicting this type of distress in HMA layers.

The HMA fracture mechanics (HMA-FM) model developed at the University of Florida (UF) was determined as necessary to form the basis of this study because of its associated threshold concept that is suitable for developing rules for both top-down cracking initiation and propagation, and its ability to model the presence of macro cracks and their effect on response. However, the effect of aging and healing on top-down cracking performance during the entire service life of asphalt concrete pavement had not been considered. Also, the effect of transverse, as opposed to longitudinal, thermal stresses had not been addressed. Therefore, the framework of the existing HMA-FM model was modified by identifying and including appropriate sub-models to address these key factors, based on which the framework of the targeted model was formed.

Consequently, the targeted model/system, which was termed the HMA-FM-based model, was completed by development and integration of several key elements into the finalized framework, including material property sub-models that accounts for changes in mixture properties (e.g., fracture energy, creep rate, and healing potential) with aging, and a thermal response model that predicts transverse thermal stresses.

The HMA-FM-based model placed emphasis on the bending mechanism. A systematic parametric study showed that the model provided reasonable predictions and expected trends for both crack initiation and propagation. Furthermore, a full calibration of field sections indicated that the predictive system adequately represents and accounts for the most significant factors that influence top-down cracking in the field. The validation efforts using the prediction sum of squares (PRESS) procedure further established the viability of the predictive system. In conclusion, the work performed clearly indicates that the HMA-FM-based model developed and evaluated in this study should form the basis for a top-down cracking model suitable for use in the mechanistic-empirical pavement design guide (MEPDG).

CHAPTER 1
INTRODUCTION

Background

It is now well accepted that load-related top-down cracking (i.e., cracking that initiates at or near the surface of the pavement and propagates downward) commonly occurs in hot-mix asphalt (HMA) pavements. The phenomenon has been reported to occur in many parts of the United States (1, 2, 3), as well as in Europe (4, 5), Japan (6), and other countries (7). This mode of failure cannot be explained by traditional fatigue mechanisms used to explain load-associated fatigue cracking that initiated at the bottom of the HMA layer. The lack of an appropriately verified description (i.e., model) of the mechanisms that lead to this type of cracking makes it difficult to effectively mitigate this costly form of distress.

Several researchers (8) have developed hypotheses regarding the mechanisms of top-down cracking. Some researchers (9, 10) have also proposed experimental methods that may provide the properties necessary to evaluate the susceptibility of HMA mixtures to this type of distress. In addition, researchers (8, 11, 12) have performed analytical work that has led to the development of preliminary models that offer the potential to predict the initiation and propagation of top-down cracks. However, only limited research has been performed to evaluate and validate these hypotheses, test methods, and models.

Research is needed to further evaluate the causes of top-down fatigue cracking and to develop effective laboratory testing systems and models that can assist material and pavement engineers to mitigate this problem. Suitable systems and models would also help to provide guidance for pavement engineers to select HMA mixtures and pavement structures that are the most resistant to top-down fatigue cracking in specified loading and environmental conditions.

Objectives

The objectives of this research were:

- To develop a mechanistic-based model for predicting top-down cracking performance in asphalt concrete pavement.
- To show that the developed model adequately represents and accounts for the significant factors (e.g., aging, healing, and transverse thermal stresses) that influence top-down cracking.
- To assess the ability of the developed model to accurately predict top-down cracking in the field.
- To demonstrate that the model developed and evaluated in this study can form the basis for a top-down cracking model suitable for use in the MEPDG.

Scope

For years, many researchers have made efforts to identify key factors and fundamental mechanisms that may lead to top-down cracking. Based on these efforts, two major mechanisms for top-down cracking initiation were identified for consideration in this study:

- The first mechanism is related to the bending-induced surface tension away from the tire (i.e., bending mechanism), which governs crack initiation in HMA layers of thin to medium thickness.
- The second mechanism is associated with the shear-induced near-surface tension at the tire edge (i.e., near-tire mechanism), which explains crack initiation in thick HMA layers.

Of these two mechanisms, emphasis was placed on the bending mechanism because most of the pavement sections evaluated in this study have thickness values within the thin to medium range. However, preliminary investigations were also conducted using the near-tire mechanism.

The HMA fracture mechanics (HMA-FM) model developed at the University of Florida (UF) has a threshold concept that is suitable for developing rules for both top-down cracking initiation and propagation, and can model the presence of macro cracks and their effect on response. In fact, these characteristics make the HMA-FM model uniquely suited to address the

mechanisms associated with top-down cracking. Therefore, it was selected as the basis for model development in this study.

Field sections from which performance data and field cores for determining mixture properties were obtained for use in calibration and validation were mainly selected from available Florida sections. Only two of the sections were obtained from Minnesota. In addition, one full-scale test was used to estimate two critical stiffness values for use in the healing model. The test was conducted in the Accelerated Pavement Testing (APT) facility at Florida Department of Transportation (FDOT) using the Heavy Vehicle Simulator (HVS).

Research Approach

The research approach taken for the development of a mechanistic-based model for prediction of top-down cracking is described in the following five phases:

- Determine key elements that must be part of the top-down cracking predictive system. The HMA-FM model developed at UF was selected to form the basis of the system because of its ability to model the presence of macro cracks which are essentially discontinuities that reduce the effective cross-section of the pavement layer, and their effect on the stress, strain, and energy distribution within the layer. However, the HMA-FM model in its existing form did not account for several key factors (e.g., aging, healing, and thermal stress) critical to properly represent the dominant top-down cracking mechanisms. Therefore, several appropriate sub-models were also identified for incorporation into the predictive system. A finalized framework of the predictive system is presented in Chapter 3 (Section One).

- Develop sub-models for incorporation into the predictive system. In this phase, several key elements were developed including material property sub-models that accounts for changes in mixture properties (e.g., fracture energy, creep rate, and healing potential) with aging, and a thermal response model that predicts transverse thermal stresses.

- Integrate model components into the predictive system. First, two core modulus, i.e., the crack initiation simulation (CIS) and crack propagation simulation (CGS) modules were formed on the basis of a critical condition concept. The sub-models developed in the second phase were then integrated into the framework of the predictive system. Consequently, an enhanced model, i.e., an HMA-FM-based model was formed.

- Evaluate the HMA-FM-based model. A parametric study was conducted using the integrated model to determine whether important factors that affect top-down cracking performance were appropriately captured by the predictive system.

- Calibrate and validate the HMA-FM-based model. The integrated system was calibrated and validated using field sections to show that it can reasonably predict top-down cracking performance of HMA pavements using rheological and fracture properties of HMA mixtures.

CHAPTER 2
LITERATURE REVIEW

The primary purpose of this chapter was to summarize the current understanding of cracking mechanisms and damage criteria in the area of design and evaluation of asphalt concrete pavement. The following subjects were examined:

- Classical fatigue approach
- Continuum damage model
- HMA fracture mechanics model
- Material property models

Emphasis was placed on the published works on existing HMA facture mechanics model and on material property models, which are crucial to the development of a mechanics-based model to predict top-down cracking in HMA layers.

Classical Fatigue Approach

Earlier work to predict fatigue cracking of asphalt mixtures was primarily performed using fatigue tests. The allowable number of load repetition determined at failure of a test specimen was considered the life of the asphalt mixture. A more advanced approach, able to account for the effect of pavement structure was developed by calibrating on the basis of tensile strains at the bottom of the asphalt concrete layer. Different types of equations proposed by many researchers have been widely used as fatigue criteria. A typical predictive equation (13) for fatigue cracking is given as

$$N_f = f_1(\varepsilon_t)^{f_2}(E_1)^{f_3} \tag{2-1}$$

where E_1 = elastic modulus of asphalt concrete layer
ε_t = tensile strain at the bottom of asphalt concrete layer
f_1, f_2, f_3 = constants determined from laboratory fatigue tests
N_f = allowable number of load repetitions

These constants (i.e., f_1, f_2, and f_3), which relate HMA tensile strain or modulus to the allowable number of load repetitions, vary between investigators. However, due to lack of a fundamental mechanism, the approach is somewhat limited, and more mechanistic approaches are being employed.

Viscoelastic Continuum Damage Model

The evolution of the viscoelastic continuum damage (VECD) model started with the work of Kim and Little (14), in which they successfully applied Schapery's theory (15) for composite materials to sand asphalt concrete under cyclic loading. In their work, a viscoelastic problem was transformed to an elastic case by replacing physical strains by pseudo strains based on the extended elastic-viscoelastic correspondence principle.

The above initial work was further developed and applied to asphalt concrete under monotonic loading (16) and cyclic loading (17 - 20). A fifty percent reduction in initial pseudo stiffness was generally used as a failure criterion for asphalt mixtures. Damage functions developed under a cyclic stress or strain controlled loading test of asphalt mixture were used as input parameters to evaluate cracking performance. Based on experimental data of asphalt concrete subjected to continuous and uniaxial cyclic loading in tension, Kim et al. (18) proposed a constitutive model that describes the mechanical behavior of the material under these conditions:

$$\sigma = I\left(\varepsilon_e^R\right)\left[F + G + H\right] \tag{2-2}$$

where I = initial pseudo stiffness
ε_e^R = effective pseudo strain
F = damage function
G = hysteresis function
H = microdamage healing function

The effective pseudo strain accounts for the difference in fatigue mechanisms between controlled-strain and controlled-stress modes. The parameter, I is used to account for sample-to-sample stiffness variation in the asphalt specimens. The damage function, F represents the change in slope of the stress-pseudo strain loop as damage accumulates in the specimen. A mode factor is also applied to the damage function, F, to allow a single expression for both modes of loading. The hysteresis function, G describes the difference between the loading and unloading paths. The healing function, H accounts for change in pseudo stiffness due to healing. More details of this model can be found in Kim et al. (17, 18), and Lee et al. (19).

To determine the fatigue life for a controlled-strain testing mode, Lee et al. (20) found that the hysteresis function, G need not be considered and that stress and pseudo strain values (ε_m^R) at peak loads alone were sufficient.

$$\sigma_m = IC(S)(\varepsilon_m^R) \tag{2-3}$$

where I = initial pseudo stiffness
C = coefficient of pseudo stiffness reduction (or, normalized pseudo stiffness)
S = internal state variable

A framework for including the effect of aging on the pseudo strain calculation was later developed by Daniel, et al. (21) to extend the model for prediction of field performance of mixtures over years. Subsequently, the VECD model was enhanced to incorporate characterization of viscoplastic behavior that might exist at slow loading rates and/or at high temperatures (22, 23, 24). Recently, a simplified fatigue test and analysis procedure (25) was also developed to identify a single characteristic curve that describes the reduction in material integrity as damage grows in the specimen regardless of applied loading conditions.

However, the viscoelastic continuum damage based model does not consider a real physical crack in a material; therefore it cannot specifically address the stress redistribution due

to cracking. Also, failure of a material is generally assumed to coincide with a 50 percent reduction in pseudo stiffness, since damage mechanics does not provide a realistic physical interpretation of failure.

HMA Fracture Mechanics Model

The continuing development of the HMA fracture mechanics (HMA-FM) model, which was determined to be necessary to include effects of aging, healing, and thermal stress on top-down cracking performance, represented a significant proportion of the effort of the researchers at the University of Florida (UF). The enhancements made to this model to make it suitable for use in a MEPDG framework will be reviewed following the sequence of each new development.

HMA Fracture Mechanics

Recently, researchers at UF (26, 27) developed the HMA fracture mechanics model. In this model, a fundamental crack growth law (named HMA fracture mechanics) was developed that allows for predicting the initiation and propagation of cracking, including top-down cracking, in asphalt mixture. This law is based on the fact that asphalt mixture has been determined to have a dissipated creep strain energy threshold ($DCSE_f$). Once the damage in asphalt mixture is equal to (or larger than) the threshold, a critical condition is triggered, which results in crack initiation (or propagation).

HMA Fracture Mechanics-based Crack Growth Simulator

Sangpetngam (28, 29) developed a HMA fracture mechanics-based crack growth simulator, which is based on the displacement discontinuity boundary element method (DDBEM). The resulting simulator is capable of predicting relative cracking performance among asphalt pavements of similar age.

Energy Ratio Approach

Roque et al. (30) derived a parameter termed the energy ratio (ER) based on a detailed analysis and evaluation of 22 field test sections in Florida using the HMA fracture mechanics model. The ER, which is defined as $DCSE_f$ of the mixture divided by the minimum dissipated creep strain energy ($DCSE_{min}$), is determined on the basis of properties that can be obtained from modulus, creep and strength tests performed with the Superpave IDT at a temperature of 10 °C. This parameter accounts for effects of both damage and fracture properties on top-down cracking performance. A higher ER implies better cracking performance.

Modified Energy Ratio Approach

Since ER is limited to the evaluation of load-induced cracking performance, it may not provide a reliable basis to assess pavements located in areas where the thermal effect cannot be neglected. Therefore, Kim et al. (31) derived a system of equations to calculate thermally induced damage and then developed a modified energy ratio (MER) approach by introducing a correction factor into the ER equation accounting for effects of thermally induced damage on top-down cracking.

In summary, these research efforts essentially formed the existing HMA fracture mechanics model. However, the effect of aging and healing on top-down cracking performance during the entire service life of asphalt concrete pavements was not considered, which certainly cannot be ignored for more accurate prediction of top-down cracking. Therefore, several mixture property sub-models that were suitable for further development into mixture aging and healing models for incorporation into the HMA-FM model were reviewed in the following subsection. In addition, transverse, instead of longitudinal, thermal stresses needed to be considered for prediction of top-down cracking, since unlike thermal cracking, top-down cracking generally occurs in the longitudinal direction. Furthermore, the thermally induced damage needed to be

directly involved in the computation of damage accumulation, so that damage recovery due to healing can be applied in a more consistent way as compared to the indirect approach used in the MER method.

Material Property Models

In this part, several existing mixture property sub-models, which were suitable for further development, are reviewed.

Binder Aging Model

Asphalt aging is sometimes quantified by change in binder viscosity, which is directly related to the prediction of dynamic modulus and the creep properties, as discussed below. The binder viscosity at mix/laydown condition (t = 0) is estimated using the following equation (32):

$$\log\log(\eta) = A + VTS \times \log(T_R) \tag{2-4}$$

where η is the binder viscosity in centipoises (10^{-2} poise), T_R is the temperature in Rankine, and A and VTS are regression constants. Typical values of A and VTS for three commonly used asphalt binders are given below (see NCHRP 1-37A design guide):

PG 64-22:	A = 10.98	VTS = –3.68
PG 67-22:	A = 10.6316	VTS = –3.548
PG 76-22:	A = 9.715	VTS = –3.208

For aged conditions, the viscosity of the asphalt binder at the pavement surface (depth z = ¼ in) can be estimated from the following in-service surface aging model (32):

$$\log\log(\eta_{aged}) = F_{AV} \times \frac{\log\ \log\ (\eta_{t=0})\ +\ A_f\ t}{1\ +\ B_f\ t} \tag{2-5}$$

where t is the time in months, F_{AV} is the air void adjustment factor, and A_f and B_f are field aging parameters that are functions of the in-service temperature and the mean annual air temperature (MAAT). The expressions for these parameters can be found in the current design guide (33). The viscosity-depth relation is given as:

$$\eta_{t,z} = \frac{\eta_t(4+E) - E(\eta_{t=0})(1-4z)}{4(1+E\cdot z)} \quad and \quad E = 23.82\exp(-0.0308\cdot Maat) \tag{2-6}$$

Dynamic Modulus Model

The dynamic modulus $|E^*|$ of asphalt concrete is used to analyze the response of pavement systems. Numerous attempts have been made to develop regression equations to calculate the dynamic modulus from conventional mixture volumetric properties. The predictive equation developed by Witczak and Fonseca (34) is one of the most comprehensive mixture dynamic modulus models available today. This model is used in the current ME design guide. According to Witczak's model, the dynamic modulus $|E^*|$ can be represented by a sigmoidal function as follows:

$$\log\left|E^*\right| = \delta + \frac{\alpha}{1 + \exp(\beta + \gamma \log t_r)} \tag{2-7}$$

where $|E^*|$ is in psi; t_r is reduced time in seconds (1/f, f is loading frequency) at a reference temperature; δ, α, β, γ are fitting parameters. Detailed expressions for δ, α, β, γ in terms of the gradation and volumetric properties of the mixture can be found in Witczak and Fonseca (34).

Tensile Strength Model

In their work on evaluation of mixture low temperature cracking performance, Deme and Young (35) found that the tensile strength of mixture (S_t) is well correlated with the mixture stiffness at a loading time of 1800 second, i.e., S_{1800}. They had extensive data in the temperature range of -40 to 25 °C. Based on these data, the following relation was obtained between the mixture stiffness (in psi) and the tensile strength (in Mpa) through regression:

$$S_t = \sum_{n=0}^{5} a_n \cdot \left(\log S_f\right)^n \tag{2-8}$$

Where S_f is the tensile stiffness that can be obtained from the dynamic modulus $|E^*|$ by taking t = 1800 s. The constants a_n are shown as follows,

$$a_0 = 284.01, \quad a_1 = -330.02, \quad a_2 = 151.02, \quad a_3 = -34.03,$$
$$a_4 = 3.7786, \quad a_5 = -0.1652$$

Healing Model

The concept of healing to increase mixture fatigue life has been observed and has been more widely accepted by researchers (36 - 41) in recent years. Button et al. (36) conducted controlled displacement crack growth testing in asphalt concrete mixes modified with various additives. They found an increase in work was required to open cracks after rest periods due to both relaxation in the uncracked body and chemical healing at the micro-crack and macro-crack interface. Zhang (37) conducted fracture tests using the Indirect Tensile Test and showed there is a critical energy level that distinguishes micro-damage from macro-damage; micro-damage is healable and macro-damage is not. Daniel and Kim (38) used a third point bending beam machine to induce flexural damage in beam specimens subjected to cyclic loading. They found the calculated flexural stiffness increased after the specimens were subject to rest periods. Figure 2-1 shows that healing increased the ultimate number of cycles the specimen endured before failure at 20 °C.

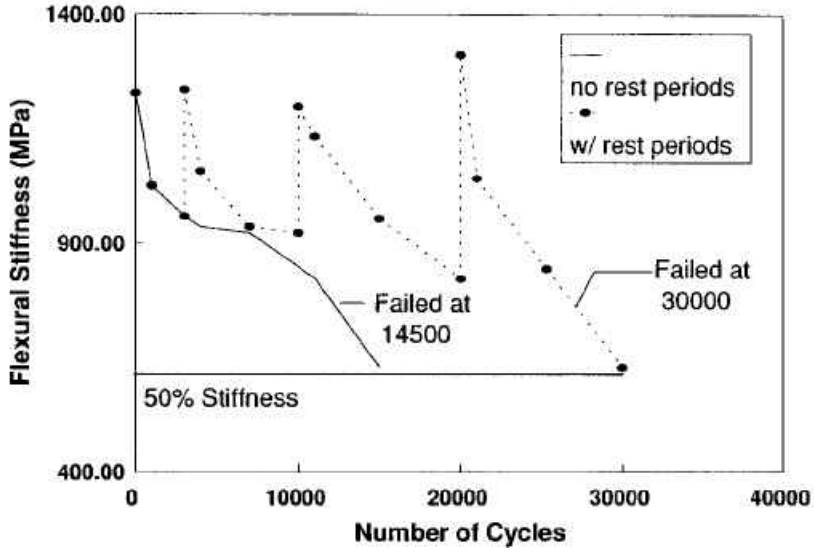

Figure 2-1. Flexural stiffness versus number of cycles to failure with and without rest periods (after Daniel and Kim, 2001)

Recent research by Kim and Roque (39) focused on development of experimental methods to evaluate healing properties of asphalt mixture. First, the DCSE associated with healing during unloading was determined by developing relationships between changes in resilient deformation and DCSE. The healing process was then expressed in terms of DCSE versus time. Figure 2-2 presents healing results at 20 °C for different applied DCSEs in the same mixture. Based on these results, they defined a healing rate h_r, which can be expressed as

$$h_r = DCSE_{healed}(t)/\ln(t) \tag{2-9}$$

where, $DCSE_{healed}(t)$ is the recovered DCSE at time t, which is defined as,

$$DCSE_{healed}(t) = DCSE_{induced} - DCSE_{remain}(t) \tag{2-10}$$

where, $DCSE_{induced}$ is the total energy dissipated at the end of the loading period, and $DCSE_{remain}(t)$ is the dissipated energy remaining at time t during the rest period. As a further step, they identified a normalized healing rate h_{nr}, which was defined as,

$$h_{nr} = h_r / DCSE_{induced} \tag{2-11}$$

Substituting Eqn (2-9) into Eqn (2-11), leads to the following form,

$$h_{nr} = \left[1 - \frac{DCSE_{remain}(t)}{DCSE_{induced}} \right] / \ln(t) \tag{2-12}$$

The normalized healing rate was found to be independent of the amount of damage incurred in the asphalt mixture. It was also found to increase with increasing temperature.

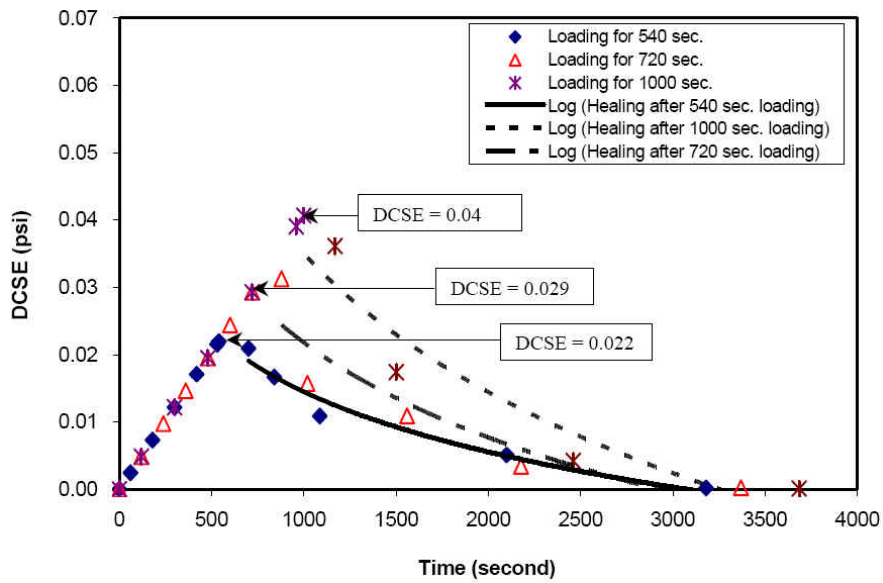

Figure 2-2. Healing tests at different DCSE for modified mixture: loading with 55 psi & healing at 20 °C (after Kim and Roque, 2006)

CHAPTER 3
DEVELOPMENT OF MODEL FRAMEWORK AND COMPONENTS

In this chapter, the finalized model framework was presented, followed by a detailed description of three major components of the HMA-FM-based model (also termed the top-down cracking performance model): material property model, pavement response model, and pavement fracture model.

Model Framework

As shown in Figure 3-1, the finalized framework of the performance model includes five main parts: 1) inputs module, 2) SuperPave indirect tensile test (IDT), 3) material property model, 4) pavement response model, and 5) pavement fracture model.

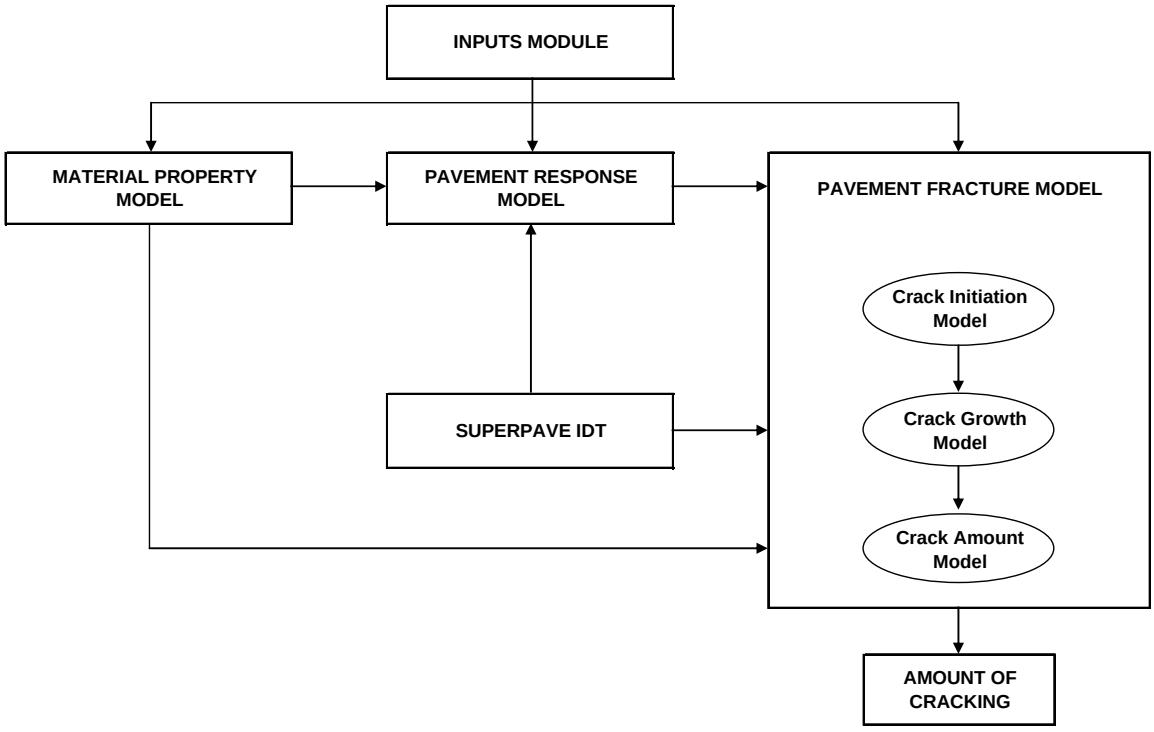

Figure 3-1. Framework of the Top-down cracking performance model

Inputs Module and Indirect Tensile Test

The inputs module provides traffic volume (in ESALs), temperatures within HMA layer (as predicted using enhanced integrated climatic model), and pavement material and structural properties. The required input for material and structural properties includes three parts:

- HMA material property, including basic mixture characteristics (gradation etc.) and damage and fracture properties (Superpave IDT).
- Modulus of base, subbase, and subgrade
- Layer thickness

The Superpave IDT developed as part of the Strategic Highway Research Program (SHRP) was used to determine damage and fracture properties on field cores as part of the calibration efforts. Three types of tests were performed with the Superpave IDT: resilient modulus, creep compliance (for damage rate), and tensile strength (for fracture energy limit).

Material Property Model

Based on a brief review of the existing HMA-FM model and material property models relevant to the targeted top-down cracking performance model, four important sub-models were identified and developed, including aging models for asphalt concrete (AC) stiffness, tensile strength, and fracture energy (FE) limit, and a healing model. These sub-models formed the material property model as one key component of targeted predictive system. Details for each new development is presented in Chapter 3 (Section Two).

Pavement Response Model

The pavement response model is composed of two sub-models: 1) load response model that predicts load-induced surface tensile stresses away from the tire, and 2) thermal response model that accounts for the fact that transverse thermal stresses are limited by the maximum

frictional resistance that can develop between the HMA surface and base layers. A detailed illustration of these two sub-models is given in Chapter 3 (Section Three).

Pavement Fracture Model

The pavement fracture model consists of three sub-models: 1) crack initiation model, which is a simplified approach (without considering damage zone effects) to predict the onset of crack in HMA layers, 2) crack growth model that predicts increase of crack depth with time, and 3) crack amount model that converts the relationship of crack depth versus time to that of crack amount versus time. Details regarding each of these sub-models are presented in Chapter 3 (Section Four).

Output

The output for the predictive system is presented in one of the following two forms: 1) crack depth versus time, or 2) crack amount versus time.

Material Property Model

As can be seen from the literature review, no existing model is available to predict damage and fracture properties, or the changes of these properties with aging. However, development, calibration, and validation of a mixture model to predict damage, healing, and fracture properties is clearly a major research effort in its own right, and well beyond the scope of the current study. Therefore, the goal of this research was to develop rudimentary (place-holder) relationships between basic mixture characteristic and these properties for use when measured properties cannot be obtained.

The material property aging models and healing model developed for this purpose will be introduced in the following sub-sections. The plots used to illustrate the implementation of the models were generated using material and structural properties of one pavement section in the Washington D.C. area (see Chapter 4, Section Three for detailed information of that pavement).

AC Stiffness (Creep Compliance) Aging Model

An AC stiffness aging model was developed on the basis of binder aging model and dynamic modulus model (at a loading time of 0.1 s). In this model, the aging effect on mixture stiffness was considered using the following empirical equation,

$$|E^*|_t = |E^*|_0 \frac{\log \eta_t}{\log \eta_0} \tag{3-1}$$

where $|E^*|_t$ and $|E^*|_0$ represent the stiffnesses corresponding to aged and unaged conditions, respectively; η_t and η_0 correspond to the aged and unaged binder viscosity.

As an example, Figure 3-2 gives three predicted AC stiffness curves as a function of time (in days), i.e., daily lowest, mean, and highest AC stiffness at surface of the pavement section of Washington D.C. area during Year one (started from July 1st). The AC stiffness curves of the same mixture at Year five (i.e., after being aged for five years), are shown in Figure 3-3. It can be seen from a comparison of these two plots that the effect of aging on AC stiffness is considerable, as expected.

With the AC stiffness aging model, creep compliance curves at three different temperatures (e.g., 0, 10, and 20°C) can be obtained by simply assuming an inverse relationship between creep compliance and AC stiffness. Figure 3-4 shows the predicted creep compliance curves at multiple temperatures for the same pavement section at Year one. These were used to generate master curve (42) to obtain creep compliance rate, and to predict thermal stresses (43, 44, 45).

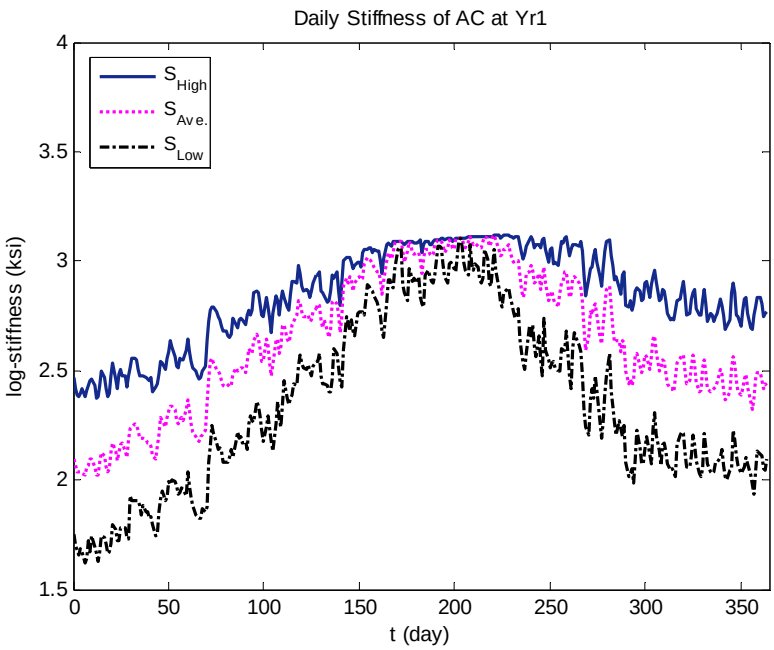

Figure 3-2. Daily AC stiffness of one pavement section in Washington D.C. area (Year one)

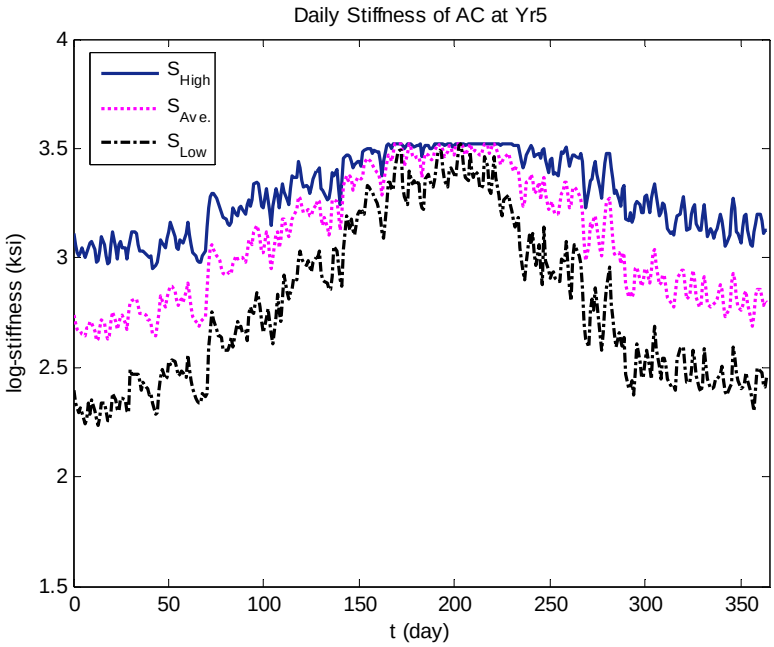

Figure 3-3. Daily AC stiffness of one pavement section in Washington D.C. area (Year five)

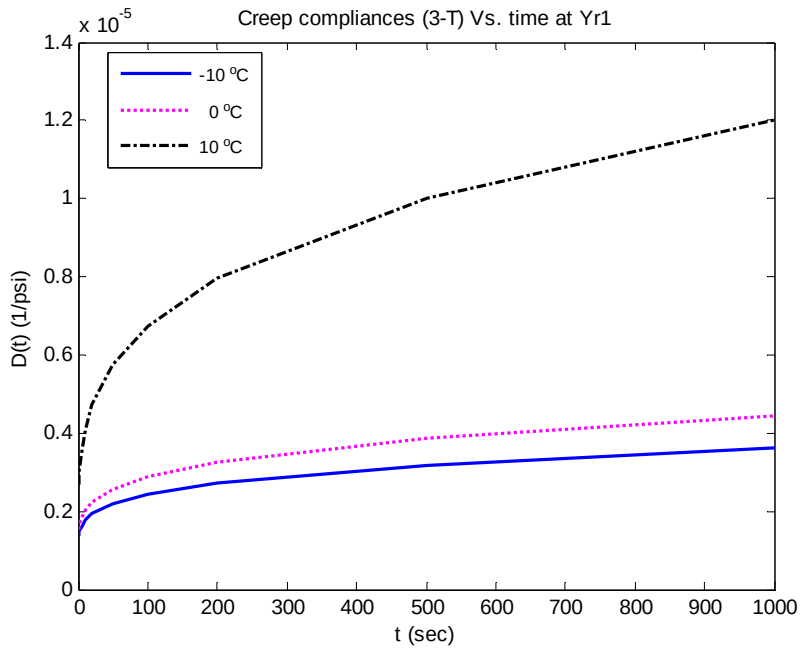

Figure 3-4. 1000 second creep compliance curves at three temperatures

AC Tensile Strength Aging Model

The AC tensile strength aging model was developed by directly relating tensile strength to the AC stiffness aging model based on the relationship developed by Deme and Young (35). As an example, Figure 3-5 (c) shows the variation of AC tensile strength with age at the surface of the pavement section. It was obtained based on the AC stiffness aging curve determined at 10°C, as shown in Figure 3-5 (d).

FE Limit (DCSE Limit) Aging Model

The FE limit surface aging model was conceived and expressed in the following form:

$$FE_f(t) = FE_i - \left(FE_i - FE_{\min}\right) \cdot \left[S_n(t)\right]^{k1} \tag{3-2}$$

where, FE_i is the initial fracture energy. FE_{min} is the minimum value of FE limit after a sufficiently long aging period t_{inf}. In this research, FE_{min} was determined based on experience (field specimens) to be 0.2 kJ/m3, and t_{inf} was chosen as 50 years. k_1 is an aging parameter to be

determined from calibration. $S_n(t)$ is the normalized stiffness at the surface of the AC layer, and is expressed as,

$$S_n(t) = \frac{S(t,0) - S_0}{S_{\max} - S_0} \tag{3-3}$$

where, S(t,0) is the stiffness at the surface of the AC layer. S_0 and S_{max} are S(t,0) when t is set as 1 year and 51 years, respectively. Therefore, it can be seen that $S_n(t)$ is a variable between zero and one. The following relationship was conceived to describe the FE limit versus depth relation:

$$FE_f(t,z) = FE_i - \left[FE_i - FE_f(t)\right] \cdot S(t,z) / S(t,0) \tag{3-4}$$

where S(t,z) is the general expression for AC stiffness. Based on the FE limit aging model, the DCSE limit aging model was developed accordingly. It is expressed as follows,

$$DCSE_f(t,z) = FE_f(t,z) - \left[S_t(t,z)\right]^2 / \left[2 \cdot S(t,z)\right] \tag{3-5}$$

where, $S_t(t,z)$ is the general expression for AC tensile strength.

As an example, Figure 3-5 (a) shows the variation of FE limit with age at the surface of the pavement in the Washington D.C. area. Correspondingly, the DCSE limit aging curve is given in Figure 3-5 (b).

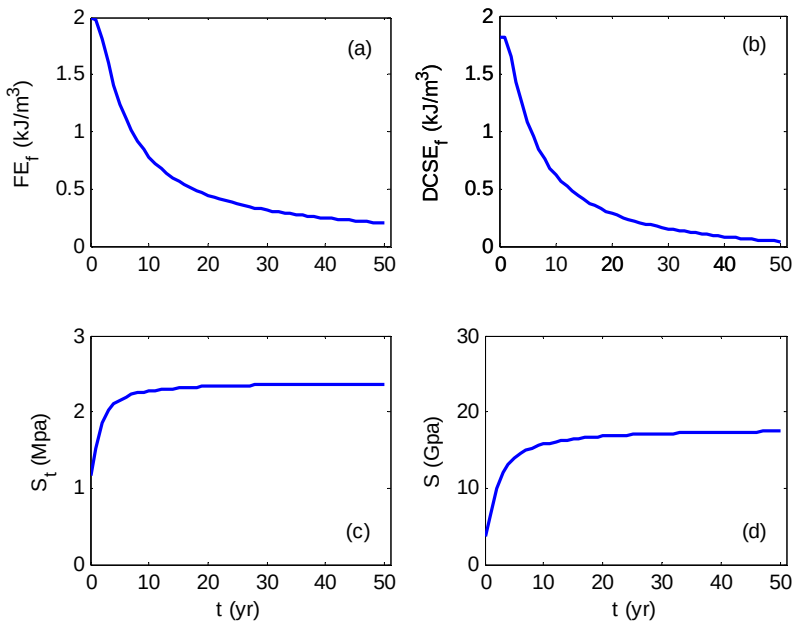

Figure 3-5. Variation of energy limits, tensile strength and stiffness with age

Clearly, the initial fracture energy FE_i and aging parameter k_1 of Equation (3-2) are key parameters that govern the trend of the FE limit aging curve. Figure 3-6 gives FE limit curves at three different values of FE_i (for a constant k_1 value of 3). As shown, generally the FE limit value decreases with time. For a larger FE_i, the entire FE limit curve moves upward (in the plot). But, the initial degradation rate of the curve also becomes larger. Figure 3-7 presents FE limit curves at three different values of k_1 for a constant FE_i value of 2. It can be seen that a larger FE limit value is associated with a larger k_1. And, the initial degradation rate of the curve is smaller for a larger k_1 value.

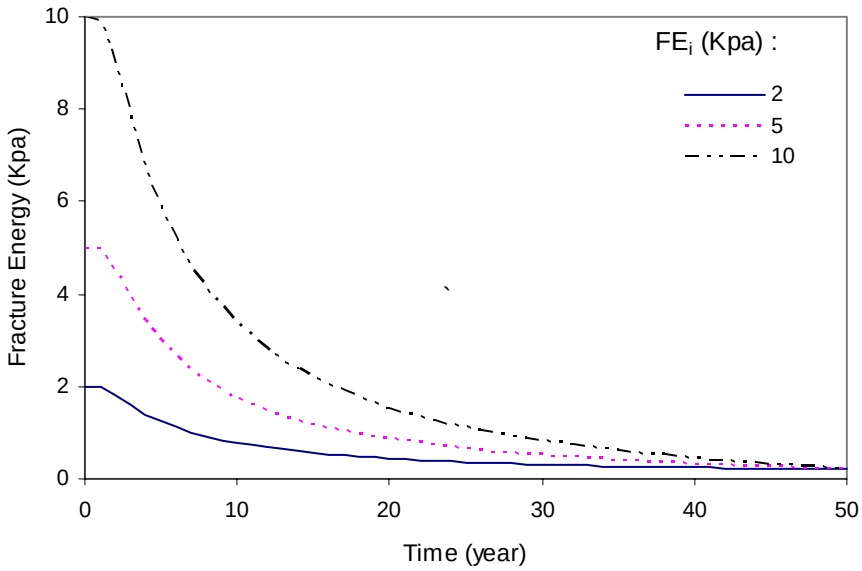

Figure 3-6. FE limit aging curves at different FE_i (k_1 = 3)

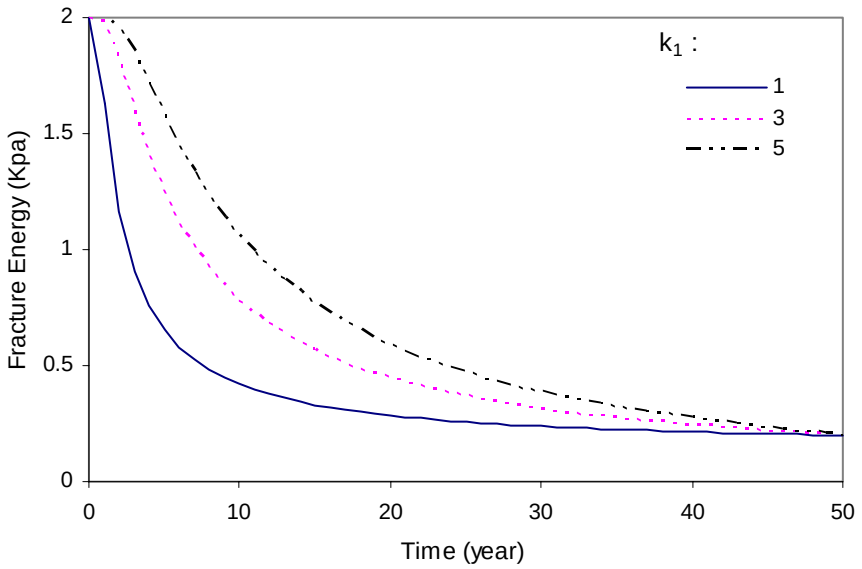

Figure 3-7. FE limit aging curves at different k_1 (FE_i = 2 Kpa)

Healing Model

The development of a healing model for use in this research was completed in two steps. First, a mixture level healing model was obtained based on the research by Kim and Roque (39). The application of this model was illustrated using a simulated SuperPave IDT repeated load test on an HMA specimen.

As a further step, possible improvements on the basis of this model for application in real pavement sections were investigated, which resulted in the development of a simplified empirically-based healing model for use in this research.

A model based on laboratory healing tests

As stated in the literature review, the normalized healing rate h_{nr} is a mixture-dependent material property, which can be determined using the laboratory healing test developed at the University of Florida (39).

If h_{nr} is known a priori, the remaining dissipated energy after healing time t can be estimated using the following equation, which was derived from Equation (2-12),

$$DCSE_{remain}(t) = DCSE_{induced} \cdot [1 - h_{nr} \cdot \ln(t)] \tag{3-6}$$

where, $DCSE_{induced}$ is the dissipated energy at the end of the loading period.

Based on Equation (3-6), a healing model was developed with the following assumptions,

- Micro-damage can only be healed during rest periods.
- For cyclic loading condition with more than one rest period, the damage induced during one loading period continuous to be healed during any successive rest period, until it vanishes.
- A constant temperature condition was assumed for this healing model since shift factors for computing normalized healing rate at different temperatures had not been established because of limited test results.
- The normalized healing rate is independent of mixture aging.

This model was then used in conjunction with the existing HMA-FM model to predict crack initiation for an HMA specimen during a simulated IDT repeated load fracture test. The input information is given in Table 3-1.

As shown in the table, a constant healing period of 300 s was introduced between every 300 loading cycles. Each of the loading cycles was composed of 0.1 s of haversine loading and 0.9 s rest period. It was assumed that no healing occurred during loading.

Table 3-1. Input for a synthetic IDT test

Parameter	Value
Loading period* (sec)	300
Healing period (sec)	300
Temperature (°C)	10
m	0.505
D1 (10^{-6} 1/Kpa)	0.101
$DCSE_f$ (Kpa)	0.978
h_{nr} (1/ln(sec))	0.1

* It includes 300 loading cycles. Each cycle lasts 1-second.

Figure 3-8 shows the predicted DCSE versus number of load cycles for the with and without healing conditions. As shown, the damage accumulation when healing was accounted for is much slower than that without considering healing. The healing model based on Equation (3-6) was then incorporated into the existing HMA-FM model to more accurately predict cracking performance.

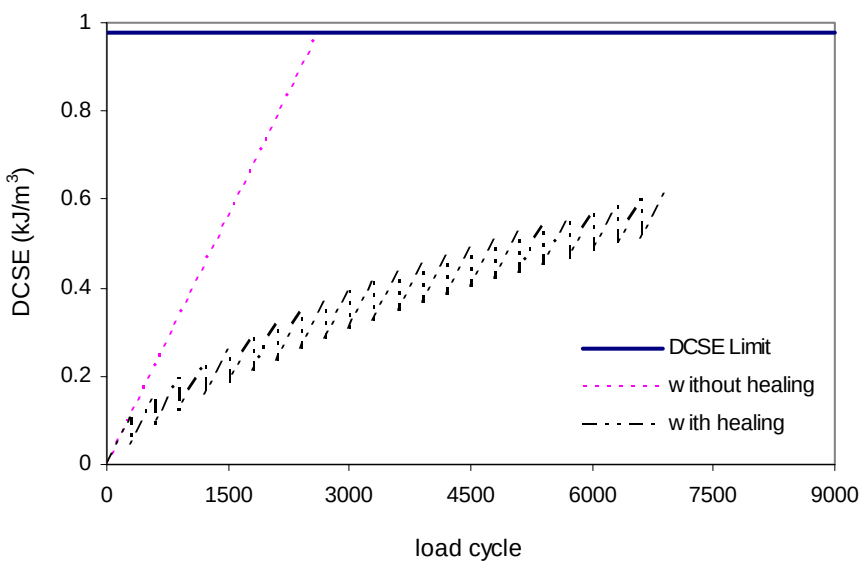

Figure 3-8. Predicted damage accumulations with and without healing

However, it is emphasized that this model may not be suitable for direct application in field conditions due to the following reasons:

- Variation of h_{nr} (i.e., healing rate) with age was not taken into account in the model.
- Similarly, variation of h_{nr} with temperature was not considered in the model.

- It is very hard to determine healing period and loading period in the field, which have varying lengths and are randomly distributed.
- Even if constant healing periods and loading periods are assumed, it is not trivial to track the decrement of damage generated in each loading period with time. In other words, the current model is somewhat computationally inefficient.

Healing model for use in this research

Since the lab test based healing model is not suitable for application in real pavements, possible improvements were investigated, which resulted in the development of an empirically-based and less computationally involved healing model, which is composed of three components:

- Maximum healing potential aging model.
- Daily-based healing criterion.
- Yearly-based healing criterion.

Each of the components is introduced as follows.

Maximum healing potential aging model

The following relationship describes the maximum healing potential surface aging model:

$$h_{ym}(t) = 1 - [S_n(t)]^{FE_i/1.67} \tag{3-7}$$

where, FE_i is the initial fracture energy, $S_n(t)$ is the normalized stiffness at the surface of the AC layer, and t is time in years. The maximum healing potential versus depth relation is:

$$h_{ym}(t,z) = 1 - [1 - h_{ym}(t)] \cdot \frac{S(t,z)}{S(t,0)} \tag{3-8}$$

where, S(t,z) is the general expression for AC stiffness, and S(t,0) is the stiffness at surface of AC layer.

As shown in Eqn (3-7), the maximum healing potential h_{ym} was controlled by the initial fracture energy. As an example, Figure 3-9 gives maximum healing potential surface aging

curves for three different values of FE_i. As shown, a higher h_{ym} is generally associated with a larger FE_i. And, the initial degradation rate of h_{ym} decreases with the increase of FE_i value.

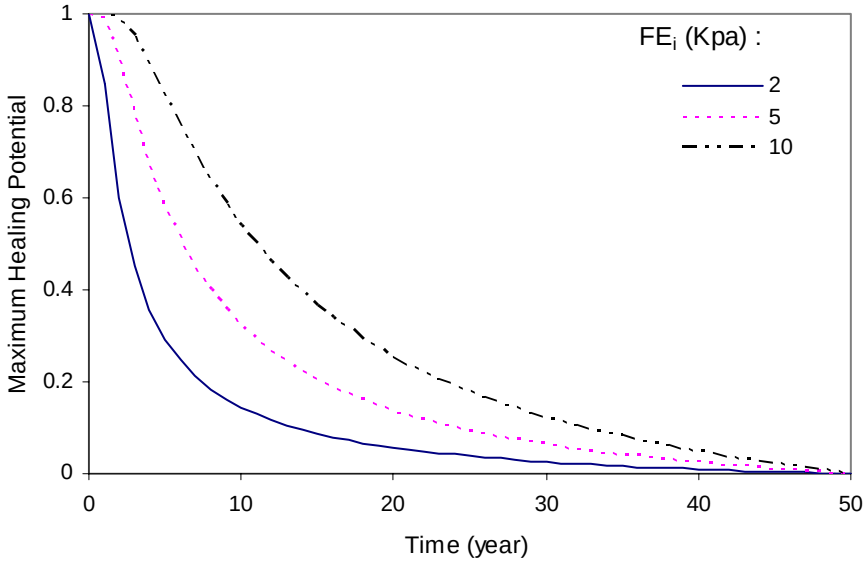

Figure 3-9. Max. healing potential surface aging curves at different FE_i

Daily-based healing criterion

A daily-based healing criterion was developed to estimate the recovered damage on any particular day. It was assumed that the damage generated in a day would be healed according to a daily normalized healing parameter h_{dn} which was defined as,

$$h_{dn} = 1 - \frac{DCSE_{d\_remain}}{DCSE_{d\_induced}} \tag{3-9}$$

where, $DCSE_{d\_induced}$ is the dissipated energy induced during the day, and $DCSE_{d\_remain}$ is the dissipated energy remaining at the end of the day after healing, which can be obtained from Eqn (3-9) as follows,

$$DCSE_{d\_remain} = DCSE_{d\_induced} \cdot (1 - h_{dn}) \tag{3-10}$$

The daily normalized healing parameter is dependent on depth, time, and temperature. In this study, h_{dn} was correlated with the daily lowest stiffness S_{low} of the AC layer. The rationale is

that healing potential is believed to be closely related to the flow capability of the AC material. Since S_{low} is the lowest stiffness of a day, it represents the highest flow capability of the material on that day. Therefore, it was used to estimate the material's healing potential.

The daily lowest stiffness can be determined using the daily highest temperature at any depth of the AC layer (refer to AC stiffness aging model). As an example, Figure 3-10 gives the variation of daily highest temperature at the surface of the pavement in the Washington D.C. area.

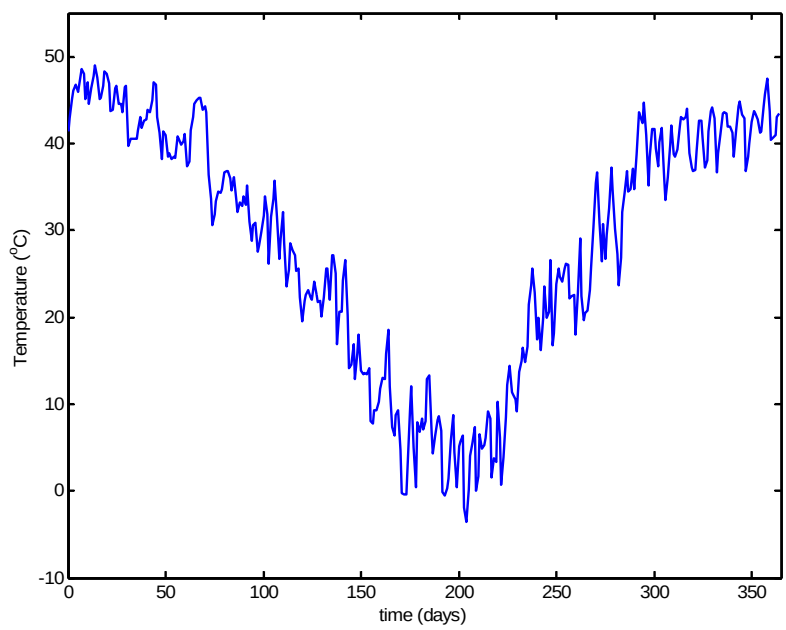

Figure 3-10. Variation of daily highest temperature

The corresponding daily lowest stiffness S_{low} for five successive years (each year was started from July 1st), after taking the effects of aging into account, are plotted in Figure 3-11. In addition, two critical stiffness values S_{cr1} and S_{cr2} are also shown in the figure, which divide the S_{low} profile into three zones,

- S_{cr1} is the Lower Bound Value. It was assumed that the daily normalized healing parameter h_{dn} reached the maximum value of a year, i.e., h_{ym} representing the highest healing potential of the mixture for that year, when: $S_{low} \leq S_{cr1}$ (i.e., when S_{low} falls into Zone A). h_{ym} was determined using the maximum healing potential aging model.

- S_{cr2} is the Upper Bound Value. It was assumed that h_{dn} reached the minimum value of a year, i.e., zero representing the lowest healing potential of the mixture, when: $S_{low} \geq S_{cr2}$ (i.e., when S_{low} falls into Zone C).

- For any S_{low} value that is between S_{cr1} and S_{cr2} (i.e., when S_{low} is in Zone B), h_{dn} can be determined by linear interpolation between zero and h_{ym}, representing intermediate healing potentials.

- Determination of S_{cr1} and S_{cr2} is discussed in Chapter 4 (Section Two).

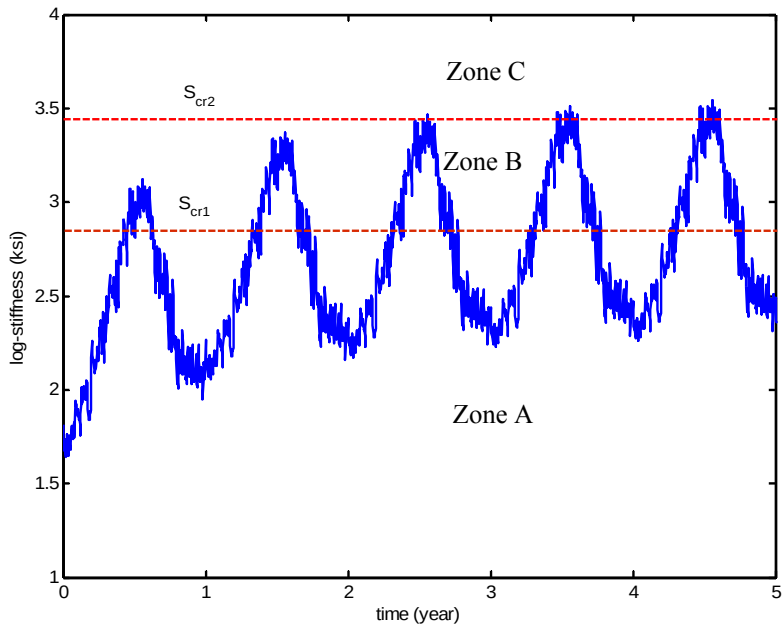

Figure 3-11. Daily lowest AC stiffness (S_{low}) profile and two critical values (S_{cr1} & S_{cr2})

Yearly-based healing criterion

In the daily-based healing criterion, the damage generated in any particular day will be healed only once during that day, after which no healing will be applied to remaining damage. This does not agree well with the observation from laboratory healing tests (39) which indicated that damage can be healed successively during any rest period that follows. Thus, a yearly-based healing criterion was developed to address continuous healing.

In this healing criterion, it was assumed that all damage accumulated during a yearly period (started from July 1st) can be at least partially healed according to a yearly normalized healing parameter h_{yn} which was defined as,

$$h_{yn} = 1 - \frac{DCSE_{y\_remain}}{DCSE_{y\_induced}} \tag{3-11}$$

where, $DCSE_{y\_induced}$ is the dissipated energy induced during the year, and $DCSE_{y\_remain}$ is the dissipated energy remaining at the end of the year after healing, which can be obtained from Eqn (3-11) as follows,

$$DCSE_{y\_remain} = DCSE_{y\_induced} \cdot \left(1 - h_{yn}\right) \tag{3-12}$$

The yearly normalized healing parameter h_{yn} was determined based on an averaged daily lowest stiffness S_{lowa} over a prolonged period T_p (i.e., the last 40 days of the yearly period being analyzed).

Pavement Response Model

The pavement response model developed as part of this study is composed of two sub-models: load response model and thermal response model. Details of each are explained below.

Load Response Model

The load response model was primarily aimed to predict bending-induced maximum surface tensile stresses, since the bending mechanism was the main focus of the HMA-FM-based model. A 9-kip circular load was applied repeatedly to the surface of a pavement to simulate the cyclic traffic load. Each cycle included 0.1 s haversine loading period and 0.9 s resting period. The model first estimated the AC modulus (see Chapter 3, Section Two) based on the temperature profiles and aging conditions. The stiffness gradient due to the temperature and aging effects was taken into account by dividing the AC layer into multiple sub-layers with different stiffnesses. The bending-induced tensile stresses at the pavement surface were then predicted using 3-dimensional (3-D) linear elastic analyses (LEA). The model also automatically searched for the maximum tensile stress on the surface of the AC layer. Figure 3-12 shows the bending-induced surface tensile stress away from the tire.

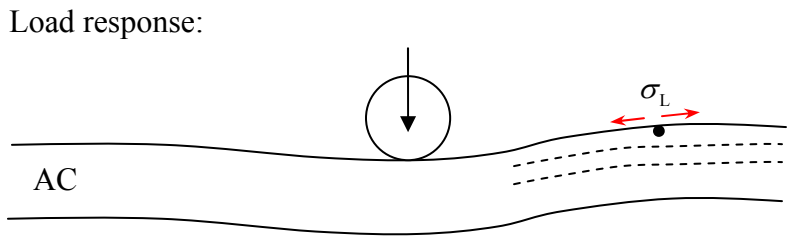

Figure 3-12. Schematic plot for load response at the surface of the AC layer

Thermal Response Model

The thermal response model predicts the thermally induced stresses in the transverse direction of asphalt concrete pavement. It was developed based on a thermal stress model for predicting thermal cracking (43).

The existing thermal stress model was developed on the basis of the theory of linear viscoelasticity. In this model, the asphalt layer was modeled as a thermorheologically simple material. Based upon Boltzmann superposition principle for linear viscoelastic materials, the time-temperature constitutive equation at time t can be expressed as follows,

$$\sigma(t) = \int_0^t E(\xi(t) - \xi(t')) \cdot \frac{d\varepsilon(t')}{dt'} dt' \tag{3-13}$$

where $E(\xi - \xi')$ is the relaxation modulus at reduced time $\xi - \xi'$; and the reduced time ξ is:

$$\xi = t / a_T$$

where a_T is the temperature shift factor. The strain $\varepsilon(t')$ can be expressed as

$$\varepsilon(t') = \alpha \left[T(t') - T_0 \right]$$

where α is the linear coefficient of thermal contraction, T(t') and T_0 are pavement temperature at time t' and the reference temperature corresponding to stress-free condition.

The following finite difference solution to Equation (3-13) can be obtained by using the Prony series representation for creep compliance,

$$\sigma(t) = \sum_{i=1}^{N+1} \sigma_i(t) \tag{3-14}$$

where

$$\sigma_i(t) = e^{-\Delta\xi/\lambda_i}\sigma_i(t-\Delta t) + \Delta\varepsilon\, E_i \frac{\lambda_i}{\Delta\xi}\left(1 - e^{-\Delta\xi/\lambda_i}\right)$$

and $\Delta\varepsilon$, $\Delta\xi$ are the changes in strain and reduced time, respectively.

The existing model was intended to predict thermal stresses in the longitudinal direction. However, top-down cracking is known to occur in the longitudinal direction, so transverse, as opposed to longitudinal, thermal stresses are of particular relevance. The difference in transverse and longitudinal thermal stresses was caused by different boundary conditions to which the AC layer is subjected in these two directions:

- The AC layer is subjected to a fixed boundary condition in the longitudinal direction, which can induce very high longitudinal thermal stresses, which are the main cause of thermal cracking.
- However, the AC layer can move in the transverse direction once the maximum friction provided by the base is reached.

Therefore, the transverse thermal stress, which contributes to top-down cracking, cannot exceed the friction limit. The limit value was determined to be 10 psi for typical HMA and base materials based on a separate calculation. Figure 3-13 shows the transverse thermal stresses due to change of temperature in an AC layer.

Thermal response:

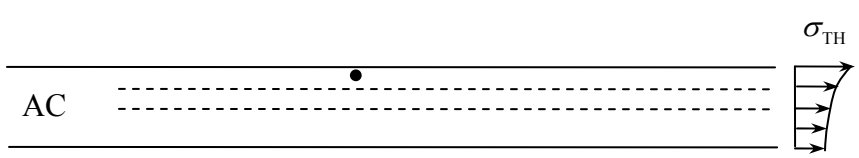

Figure 3-13. Schematic plot for thermal response in the AC layer

Pavement Fracture Model

The pavement fracture model consists of three sub-models: (i) crack initiation model, (ii) crack growth model, and (iii) crack amount model.

Crack Initiation Model

The crack initiation model was developed on the basis of the threshold concept of the existing HMA fracture model. It was used to predict the crack initiation time and location in asphalt pavement sections, in conjunction with the material property model and pavement response model. Details regarding the joint use of all mentioned models were presented in Chapter 4 (Section One).

In the crack initiation model, the load-associated damage and thermal-associated damage can be obtained based on the pavement response models as follows,

- The load-associated damage per cycle (or, $DCSE_L$/cycle) is calculated as:

$$DCSE_L / cycle = \int_0^{0.1} \sigma_{AVE} \sin(10\pi t) \dot{\varepsilon}_{p\max} \sin(10\pi t) dt \tag{3-15}$$

where σ_{AVE} is the average stress within the process zone being analyzed to determine crack initiation, and $\dot{\varepsilon}_{pmax}$ is the creep strain rate, which is determined from IDT creep tests at 1000 second loading time.

- The thermal-associated damage over time interval from (t - Δt) to t (or, $DCSE_T/\Delta t$) is expressed as:

$$DCSE_T / \Delta t = [\sigma(t) - \sigma(t - \Delta t)] \cdot [\varepsilon_{cr}(t) - \varepsilon_{cr}(t - \Delta t)] / 2 \tag{3-16}$$

where ε_{cr} is creep strain at time t. It can be expressed as:

$$\varepsilon_{cr}(t) = \varepsilon_{cr}(t - \Delta t) + \frac{1}{2 \cdot \eta} [\xi(t) - \xi(t - \Delta t)] \cdot [\sigma(t) + \sigma(t - \Delta t)]$$

In the crack initiation model, the rule for determination of crack initiation is given as follows,

$$DCSE_{norm}(t) = \frac{DCSE_{remain}(t)}{DCSE_f(t)} \geq 1.0 \tag{3-17}$$

where, $DCSE_{remain}$ is the accumulated dissipated energy when taking healing into account, $DCSE_f$ is the DCSE limit accounting for its degradation with aging, and $DCSE_{norm}$ was named due to the normalized form used for damage accumulation. The threshold for crack initiation is 1.0. The $DCSE_{remain}$ during each time interval Δt can be further expressed as follows,

$$DCSE_{remain}(\Delta t) = (1 - h_{dn}) \cdot [n \cdot (DCSE_L / cycle) + DCSE_T(\Delta t)] \tag{3-18}$$

where n is number of load cycles in Δt.

Crack Growth Model

The crack growth model was developed on the basis of a two-dimensional (2-D) displacement discontinuity boundary element (DDBE) program (46) and the threshold concept of the existing HMA fracture mechanics model. It was used in conjunction with the material property model and thermal response model to predict increase of crack depth with time in asphalt concrete pavement. Details regarding the joint use of all models were presented in Chapter 4 (Section One).

In the crack growth model, load induced tensile stresses ahead of the crack tip were predicted using the DDBE model as follows:

- The pavement structure was discretized using quadratic displacement discontinuity (DD) boundary elements.
- An initial crack was assumed to have a length of 6 mm (0.25 inch), which is about one half of the nominal maximum aggregate size of typical asphalt mixtures. It was placed vertically at the location of the maximum surface tensile stress and discretized using DD boundary elements.
- The load used for the 2-D model was adjusted so that the maximum tensile stress at surface of the pavement predicted by the 2-D model can be matched with the prediction by the 3-D LEA program. A similar strategy was used by Myers et al. (47) to account for 3-D effects on stress distribution by adjusting load applied to a 2-D pavement model.

Meanwhile, the near-tip thermal stresses were estimated by applying the stress intensity factor (SIF) of an edge crack to the thermal stresses predicted using the thermal response model.

The load associated damage and thermal associated damage were then calculated in a same manner as introduced in the crack initiation model. The same rule as used for determination of crack initiation was adopted in the crack growth model. Once the rule was satisfied (i.e., the $DCSE_{norm}$ reached 1.0), the crack started to grow. Some key terms used during simulation of step-wise crack growth are explained below:

- Potential crack growth path: The potential crack growth path was predefined in front of the crack tip at the beginning of crack growth simulation. It was composed of a series of process zones heading toward the bottom of the AC layer.
- Process zone: The process zone was used as a unit for step-wise increment of crack depth. Each of the process zones was assumed to have a uniform length of 6 mm (0.25 inch). The summation of lengths of all process zones led to the critical crack depth.
- Critical crack depth (CD_c): The critical crack depth is the final crack depth in the crack growth model, which was preset to be one-half the depth of the AC layer, as field observations showed that top-down cracking generally does not exceed that depth.

Crack Amount Model

The crack amount model was developed based on the following assumptions:

- For a 100 feet long pavement section, the maximum crack amount was assumed to be 330 feet. In other words, the pavement was determined to be severely cracked if total crack amount exceeded 330 feet.
- The crack amount, between zero and the specified maximum value, was assumed to be linearly proportional to the crack depth over AC layer thickness ratio (C/D), which ranges from zero to 0.5 (i.e., when crack depth is equal to CD_c).
- In accordance with the definition for crack initiation in terms of the crack depth (refer to crack initiation model), the onset of a crack in terms of the crack amount was assumed to be triggered by observing an amount of cracking of at least 12 feet.

Based on the above assumptions, the crack amount versus time relationship can be obtained from the crack depth versus time relation predicted by the crack growth model. Using

this model, the predicted amount of cracking at initiation is greater than 12 feet for any pavement that has an HMA layer thickness of no more than 12 inch.

CHAPTER 4
INTEGRATION OF MODEL COMPONENTS

Critical Condition Concept

The critical condition concept is central to the cracking performance model. The concept, which was developed on the basis of HMA Fracture Mechanics and its associated threshold concept, specifies that crack initiation and growth only develop under specific loading, environmental and healing conditions that are critical enough to exceed the mixture's threshold. The concept is in direct contrast to traditional fatigue theory, which assumes that cracking is a continuous process.

The integration of sub-models was completed based on this concept in the following two phases:

In phase one, a critical condition identification (CCI) module was developed based on the critical condition concept. Figure 4-1 shows the flowchart of this module. As shown, all model components are involved in this module, including: i) material property model, ii) pavement response model, and iii) pavement fracture model. The module is intended to identify the critical condition by checking normalized dissipated creep strain energy ($DCSE_{norm}$) against the threshold, which was determined to be one in this study. On the basis of the CCI module, two follow-up modules i.e., crack initiation simulation (CIS) module and crack growth simulation (CGS) module were formed. These are described in the following two subsections.

During phase two, the integration was continued to illustrate effects of healing and thermal stress using two example simulations: 1) healing effects in one pavement section in FDOT's APT facility (see Chapter 4, Section Two), and 2) thermal effects in one pavement section in Washington D.C. area (see Chapter 4, Section Three).

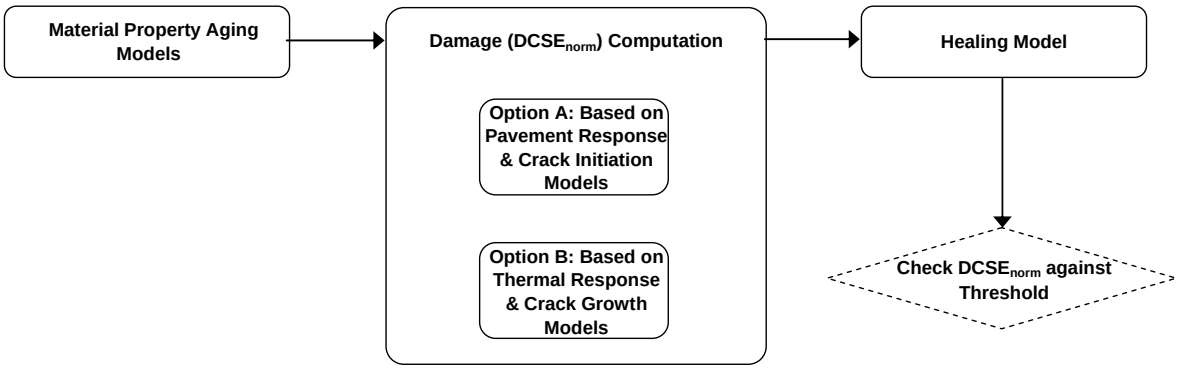

Figure 4-1. Flowchart of CCI module

Module for Crack Initiation Simulation (CIS)

The CIS module was developed by directly making use of the CCI module with option A (see Figure 4-1). The AC pavement structure is analyzed using a 3 dimensional (3-D) linear elastic analysis (LEA) program. As shown in Figure 4-2, the CCI module is called to compute the amount of induced damage, as well as damage recovery and accumulation in a step-wise manner until the critical condition is identified.

This process usually takes several years. Whenever starting a yearly period, mixture properties are updated with the material property aging models. Upon completion of the simulation, crack initiation time, as well as the location of the initial crack will be reported by this module.

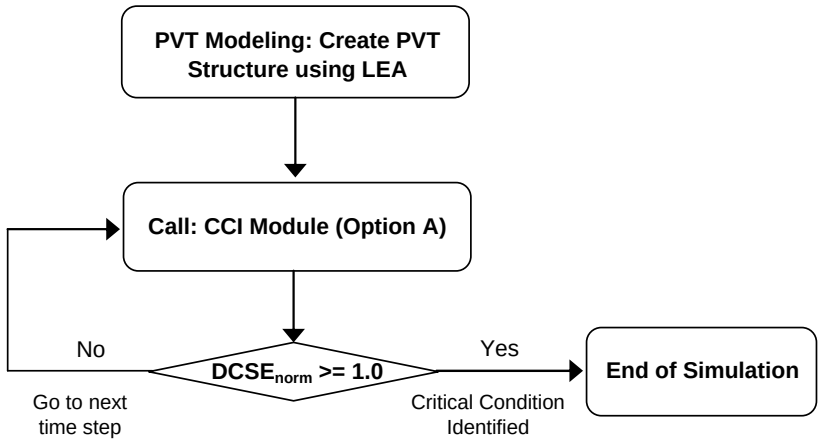

Figure 4-2. Flowchart of CIS module

Module for Crack Growth Simulation (CGS)

The CGS module was developed on the basis of CCI module with option B (see Figure 4-1). Figure 4-3 shows the flowchart for this module.

Knowing the initiation time and location of initial crack, the CGS module was started by discretizing the pavement structure using 2-D displacement discontinuity boundary elements. The CCI module is then called to compute damage accumulation for each time step. If the critical condition is identified, the crack depth increases by a distance of one process zone (assumed to be 6 mm or 0.25 inch). The updated crack depth is then checked against the critical crack depth (preset to be one-half the depth of the HMA layer as field observations showed that top-down cracking generally does not exceed one-half depth of the layer):

- If the crack depth is less than the critical crack depth, a new pavement structure with the updated crack depth will be discretized and another simulation is performed using the same steps as mentioned above. For modeling using the displacement discontinuity (DD) boundary element method (BEM), remeshing of the whole pavement structure is not required. The increase in crack depth can be simply addressed by replacing the process zone next to the current crack-tip with a few DD elements.

- Once the critical crack depth is reached, the simulation is completed. The time and applied loads corresponding to each crack depth increment will be reported at the end of this simulation.

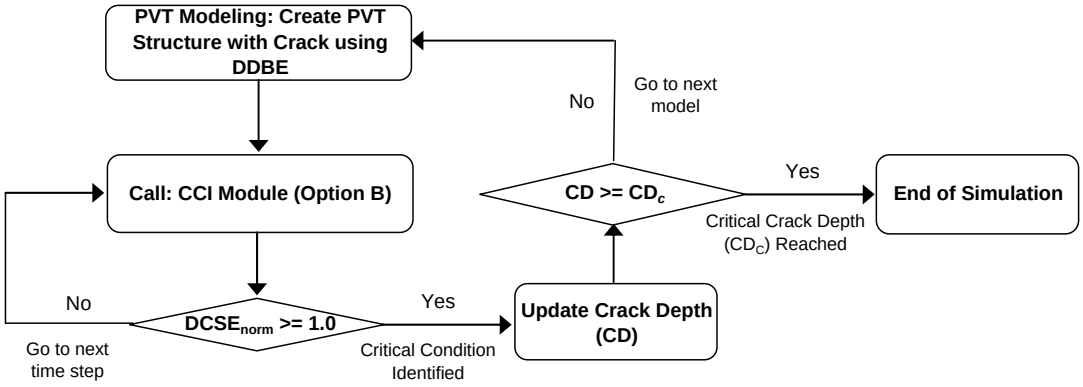

Figure 4-3. Flowchart of CGS module

Integration of Healing Model

The material healing model was integrated into the performance model by determining the two critical values for daily lowest AC stiffness on the basis of a full-scale test conducted in the FDOT's APT facility using the HVS.

Background of Experiments for Evaluating Healing Effect

Since Accelerated Pavement Testing (APT) offers great potential for evaluation of performance of asphalt mixture and pavement in relatively short periods of time, the Florida Department of Transportation (FDOT) has built an APT facility in Gainesville, Florida. The system includes a fully mobile Heavy Vehicle Simulator (HVS), and eight linear tracks (150 ft long by 12 ft wide). Figure 4-4 shows one typical test section subjected to HVS loading in FDOT's APT facility.


Figure 4-4. A typical HVS test section

The University of Florida (UF) has been working on a research project with FDOT to assess cracking potential of asphalt mixture (48). In an effort to simulate aging of in-service pavement, a unit called the Accelerated Pavement Aging System (APAS) was developed and used to induce artificial aging of asphalt pavement test sections in the APT facility. One lane (testing track 1) composed of a dense-graded mixture on limestone base and sand subgrade was divided into three test sections: 1A, 1B, and 1C. Each section was subjected to different levels of aging and HVS loading. Sections 1B and 1C were tested first to assess the capability of the APAS system and to determine whether top-down cracking could be induced within a reasonable period of time. It was found that these two sections, which were subjected to extensive loading with moderate aging, could not be cracked even after many heavy loads were applied. In addition to the excellent properties of the mixture and structure, healing was thought to be playing a major role.

Therefore, an experiment was devised to severely age one part of section 1A so as to minimize healing potential. This severely aged part and a companion unaged part were subjected

to the same loading conditions (load and temperature) to more definitively evaluate the effects of healing.

The paired portions of section 1A, which were simply called the aged and unaged sections for brevity, were subjected to 18-kip HVS loads to maximize the potential for cracking within a reasonable period of time. Loading on both sections started on February 06, 2007. During February 16 to 19, transverse surface cracks were found in the aged section after around 140,000 passes (see Figure 4-5). Loading was continued until March 27, 2007 with around 488,358 passes, when cracks in the aged section were believed to have approached about half-depth of the AC layer (this was later verified by coring the cracked AC layer). No crack was observed in the unaged section for the entire loading period.

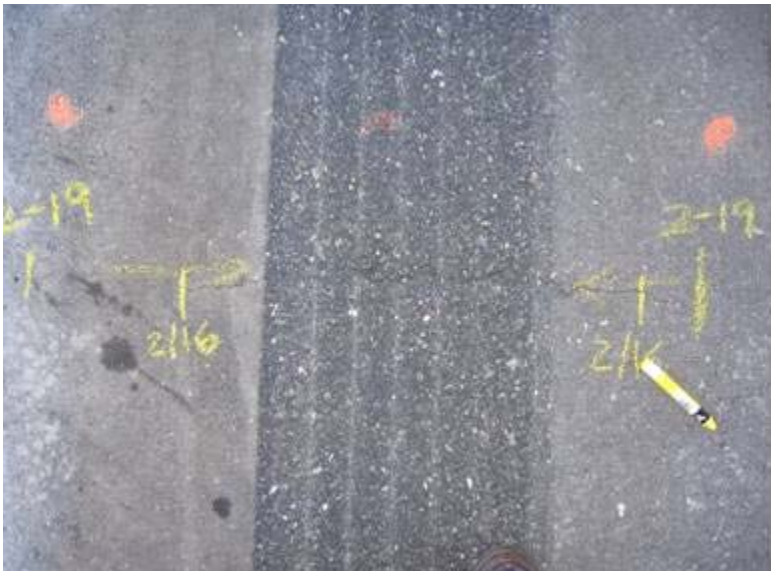

Figure 4-5. Cracks observed in the aged section

Material and Structural Properties

PG 67-22 binder was used in this study. Figure 4-6 shows binder recovery and viscosity measurements performed on cores obtained from the aged section at 0, 1, and 20 heating cycles of artificial aging. The binder viscosity of the unaged section corresponds to zero heating cycle (i.e., only slightly aged). As can be seen, the aging level induced in the top of the aged section

after 20 healing cycles was extremely high, the viscosity at which was much greater than any value determined from field cores in typical Florida pavement. Figure 4-6 also shows that the APAS was able to effectively create a stiffness gradient through the asphalt layer.

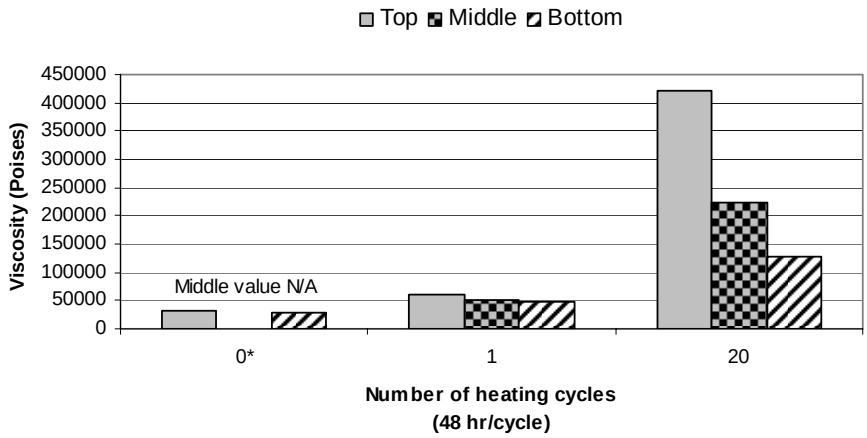

Figure 4-6. Recovered viscosity at different levels of aging

Table 4-1 summarizes the Superpave Indirect Tension Test (IDT) results on cores from the paired sections. The same asphalt mixture with Georgia granite aggregate and 4.6% binder content was used for both sections.

Table 4-1. IDT test results (at 10°C)

APAS		m-value	D_1	Creep compliance at 1000 sec	Creep rate 1/GPa	FE	DCSE HMA	ER
Unaged	Top	0.491	4.90E-07	2.15	7.13E-09	2.7	2.4	1.88
	Bottom	0.537	5.43E-07	3.27	1.19E-08	2.4	2.2	1.22
Aged	Top	0.355	1.40E-07	0.29	5.74E-10	1.0	0.8	5.68
	Bottom	0.377	4.16E-07	0.88	2.12E-09	1.1	1.0	2.03

The pavement structural and material properties for each layer of the aged section are given in Table 4-2. As shown, the AC layer was further divided into three sub-layers accounting for stiffness gradients due to aging and temperature. Table 4-3 shows creep compliance readings measured at 0, 10, and 20°C during 1000 second Superpave IDT creep tests. They were used to generate master curves for use in modeling viscoelastic material behavior.

Table 4-2. Pavement structure and material properties in the aged section

	E (psi)		H (in)
AC-Top	2.40E+06	0.35	1.5
AC-Mid	1.20E+06	0.35	1.5
AC-Bot	6.00E+05	0.35	3
Base	4.00E+04	0.35	10.5
Subgrade	3.10E+04	0.4	Inf.

Table 4-3. Creep compliance values for aged samples at 0, 10, and 20°C

	TOP			BOTTOM		
TIME (SEC)	0°C	10°C	20°C	0°C	10°C	20°C
1	0.054	0.069	0.129	0.076	0.126	0.248
2	0.059	0.075	0.152	0.076	0.145	0.296
5	0.057	0.084	0.169	0.096	0.171	0.379
10	0.059	0.096	0.196	0.098	0.198	0.443
20	0.065	0.114	0.262	0.111	0.257	0.503
50	0.085	0.126	0.328	0.127	0.296	0.828
100	0.092	0.148	0.425	0.136	0.378	1.154
200	0.095	0.176	0.597	0.146	0.471	1.607
500	0.109	0.238	0.873	0.162	0.669	2.484
1000	0.110	0.282	1.168	0.160	0.884	3.443

Model Predictions without Healing

Stage one: crack initiation

When healing effect was not considered, the predicted load passes to induce crack initiation for the aged and unaged sections are given in Figure 4-7. As seen in the figure, predicted number of loads to cracking for the unaged section was only about 41,700, which was much less than the 128,300 loads for the aged section. The predictions in Figure 4-8 in terms of $DCSE_{norm}$ versus time showed the same trend: the unaged section required less time for crack initiation than the aged one.

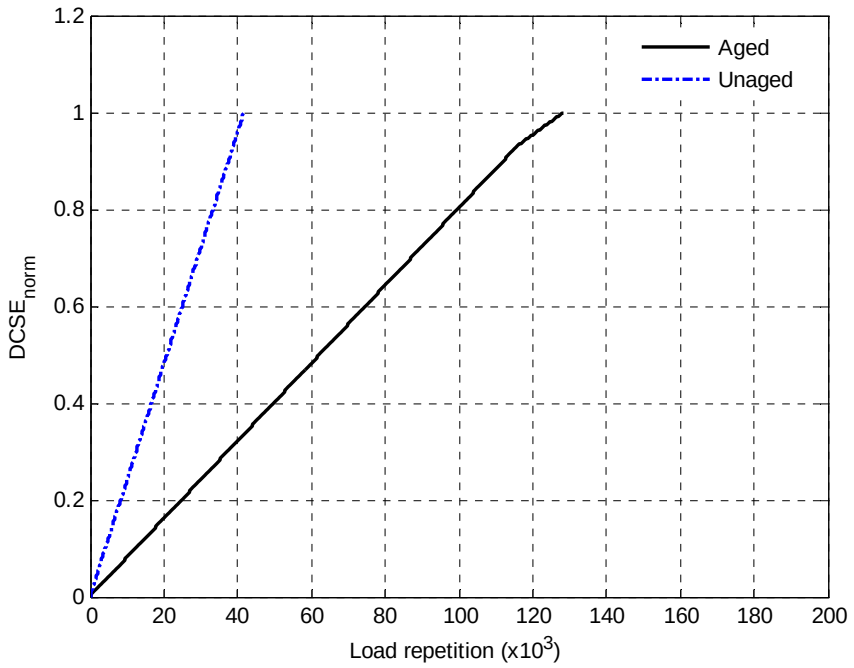

Figure 4-7. Prediction of crack initiation w/o healing: damage versus load repetition

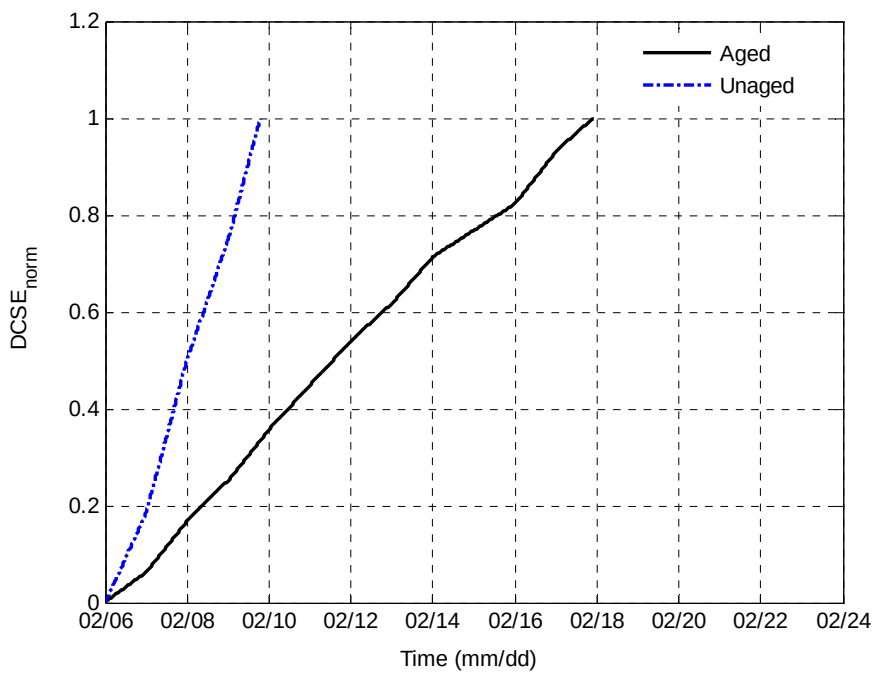

Figure 4-8. Prediction of crack initiation w/o healing: damage versus time

Stage two: crack propagation

Figure 4-9 shows the step-wise increase of crack depth with load passes for both the aged and unaged sections. In general, the crack propagates at a relatively low rate initially (e.g., for the first process zone). The rate of growth then increases for the next few zones, beyond which the rate slows down again. As also shown in Figure 4-9, the load repetition to the critical crack depth (i.e., 3 inch for these two sections) is about 129,200 for the unaged section. Meanwhile, the load to 3 inch depth of the aged section is about 295,900, which was much more than that for the aged section. Similar trends can be found from Figure 4-10, which shows crack growth as a function of time. Given the time to crack initiation obtained in stage I, an average crack growth rate in the unaged section can be estimated to be 0.34 in/day, which is more than 1.5 times of the value, i.e., 0.20 in/day obtained for the aged section.

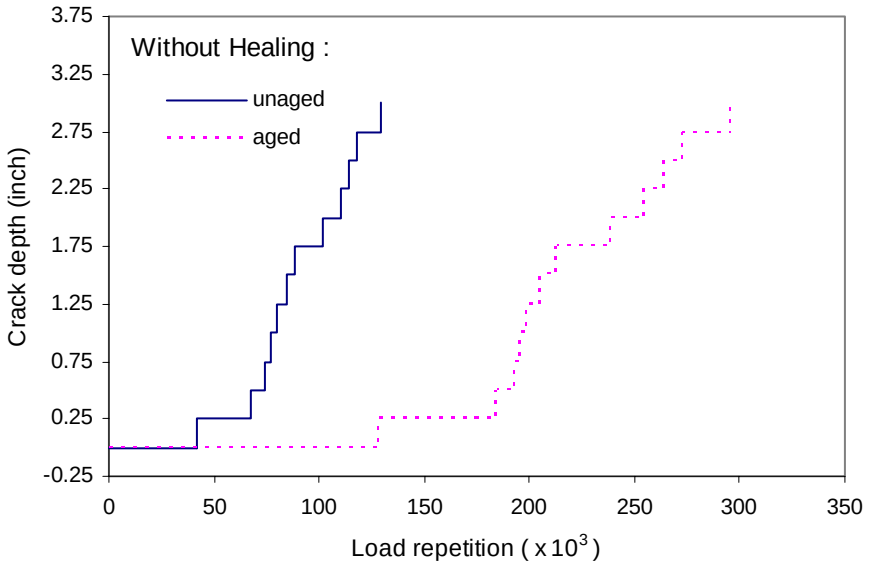

Figure 4-9. Prediction of crack growth w/o healing: crack depth versus load repetition

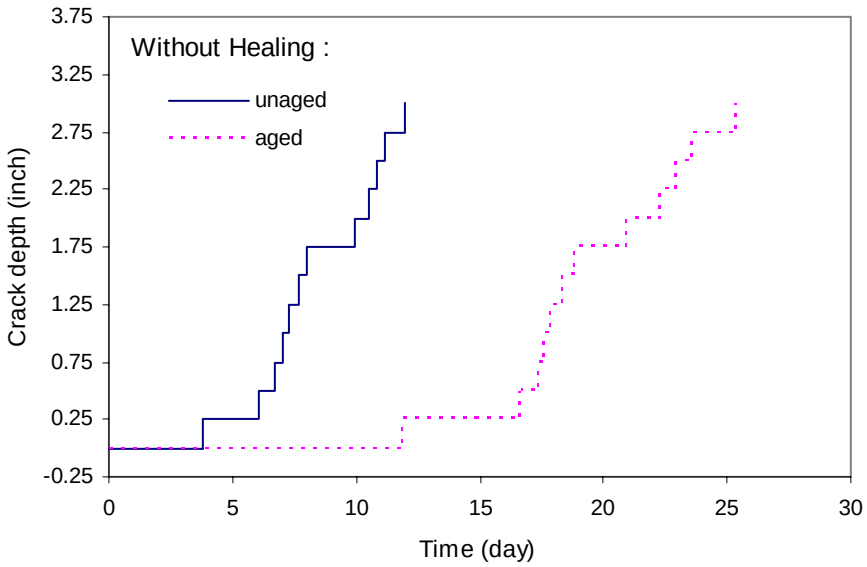

Figure 4-10. Prediction of crack growth w/o healing: crack depth versus time

It is clear that the predicted results in terms of both crack initiation and propagation in the unaged section do not make sense, since as mentioned before, no crack was observed in that section during the entire loading period. Therefore, a mixture healing model must be included in the top-down cracking performance model. However, the two critical values S_{cr1} and S_{cr2} of the healing model have to be estimated before it can be used.

Determination of Critical Values for Daily Lowest AC Stiffness

In order to determine these two critical values S_{cr1} and S_{cr2}, the daily lowest AC stiffness curves in the aged and unaged sections are plotted in Figures 4-11 and 4-12, respectively. As shown, the stiffnesses of the aged section are much higher than the unaged section.

Since the asphalt mixture at surface of the aged section was extensively aged, as indicated by the measured binder viscosity which was much greater than any value determined from field cores in typical Florida pavement, it was believed that no healing would occur in the mixture of this section. According to the definitions of healing zones (refer to Chapter 3, Section Two), the

S_{low} values for this section should be close to S_{cr2}. Therefore, the value for S_{cr2} was selected to be 2,000 ksi (see Figure 4-11).

On the other hand, mixture in the unaged section was only slightly aged, as shown by viscosity test results. The mixture was thus believed to have full healing potential. According to the definitions of healing zones, the S_{low} values for this section should be close to S_{cr1}. As a result, S_{cr1} was selected to be 320 ksi (see Figure 4-12).

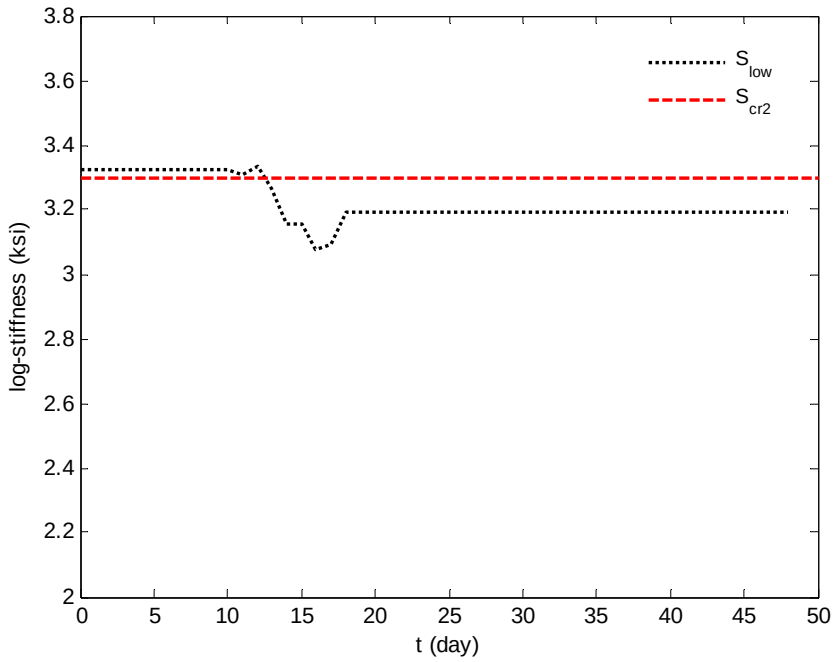

Figure 4-11. Daily AC stiffness of the aged section

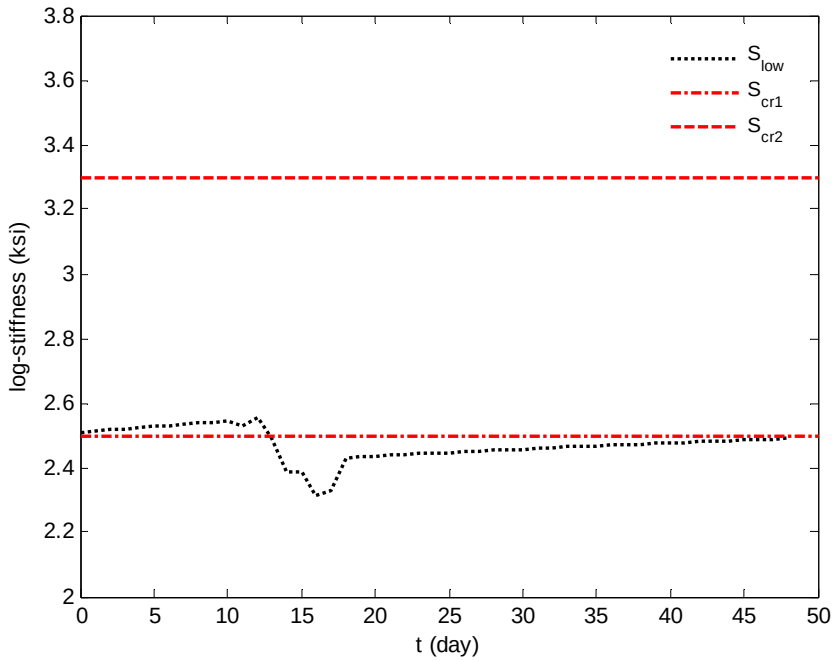

Figure 4-12. Daily AC stiffness of the unaged section

Model Predictions with Healing

Another set of predictions was made using the performance model after incorporating the healing model.

Stage one: crack initiation

The predicted damage in terms of $DCSE_{norm}$ versus load passes for the paired sections are given in Figure 4-13. The figure clearly shows that no crack occurred in the unaged section, which is consistent with the observation in the full-scale HVS test. On the other hand, the predicted load passes to crack initiation for the aged section remained at 128,300. The similar prediction for the aged section using performance models with and without the healing model is expected, since the aged section had no healing potential due to extensive aging applied in the test. The predicted load passes (128,300) were also found to be close to the actual number of passes (140,000) when the first crack was observed.

The predictions in Figure 4-14 show the same trend: crack occurred in the aged section after about 12 days, and no crack occurred in the unaged section.

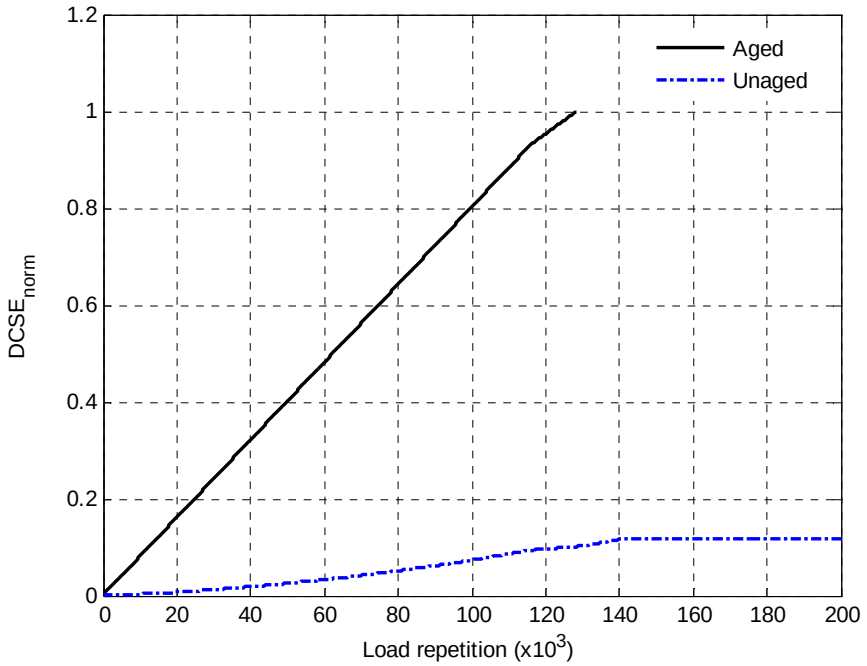

Figure 4-13. Prediction of crack initiation with healing: damage versus load repetition

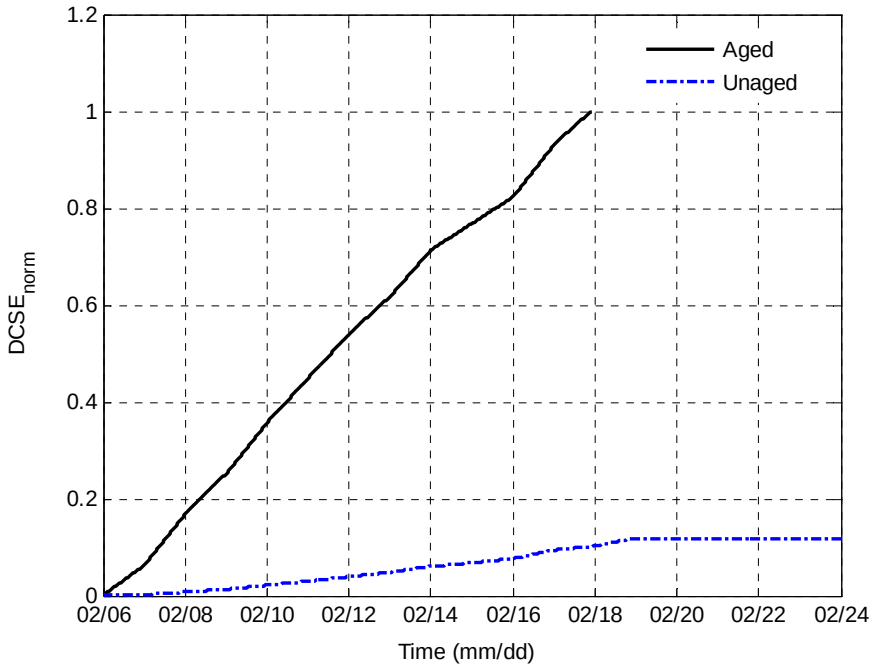

Figure 4-14. Prediction of crack initiation with healing: damage versus time

Stage two: crack propagation

Performance predictions accounting for healing were continued in the crack propagation stage. As shown in Figure 4-15, the crack in the aged section reached the critical crack depth after 296,600 passes of HVS loading. As expected, the number of load passes was slightly greater than the one predicted by the model without healing, since the healing potential, which increases with depth helped to prolong fatigue life. Figure 4-16 shows predicted crack growth in terms of crack depth versus time in the aged section, which follows a similar pattern as that of Figure 4-15. It took another 14 days for the crack to reach the critical crack depth.

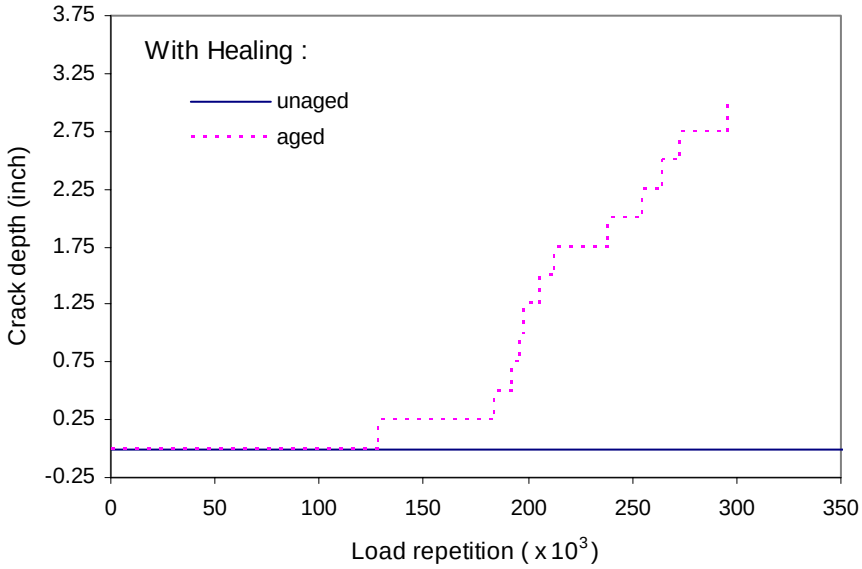

Figure 4-15. Prediction of crack growth with healing: crack depth versus load pass

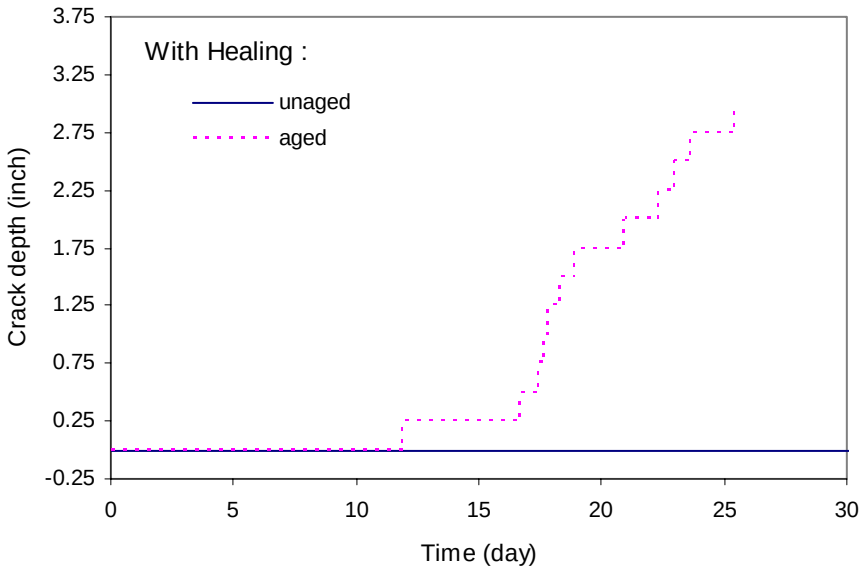

Figure 4-16. Prediction of crack growth with healing: crack depth versus time

In summary, the predictions after incorporation of the healing model seemed quite reasonable, as they agreed well with observations from cores, which indicated that the crack had propagated to about half-depth of the AC layer of the aged section.

Integration of Thermal Response Model

Integration of the thermal response model was completed by simply activating this model in the CCI module. The significance of the thermal response model was illustrated by predicting cracking performance of one pavement section in the Washington D. C. area with and without thermally induced damage accounted for in the performance model.

Selection of Climatic Environment

Since the thermal response model was fully developed, the key for successful integration of this model was to show that the performance model cannot predict cracking performance accurately without accounting for thermal effects. In other words, it was necessary to demonstrate the need to include the thermal response model.

A limited investigation indicated that thermal damage induced in pavement sections subjected to a non-freeze climate as that of Florida was not high enough to alter the predicted top-down cracking performance of these sections. Therefore, a freeze-thaw climate as that of Washington, D.C., was selected to demonstrate the importance of including the thermal response model. The corresponding temperature data file was used as input for model prediction, containing hourly temperatures at different depths of the AC layer. The temperature data was generated based on the climatic condition and typical pavement material and structural properties using the enhanced integrated climatic model (EICM). Other types of climatic environment such as the hard-freeze climate of North Dakota were evaluated in Chapter 5 (Section Three).

Material and Structural Properties

The geometry and material properties for the pavement section are illustrated in Figure 4-17. To account for the effects of stiffness gradient due to temperature and aging, the AC layer was divided into 3 sub-layers with thickness h_1, h_2, and h_3, respectively. Since the temperature and aging gradients are greatest near the surface and reduce with depth, the thickness values of the AC sub-layers were taken as $h_1 = h_2 = H_1/4$ and $h_3 = H_1/2$.

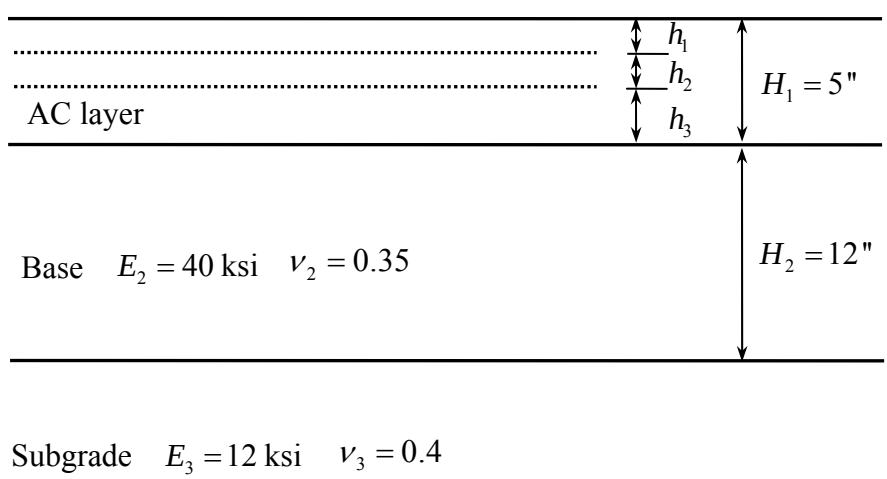

Figure 4-17. Geometry and material properties of a 3-layer pavement structure

The variation of asphalt concrete (AC) modulus with time was estimated using the AC stiffness (creep compliance) aging model. Meanwhile, the degradation of AC fracture properties and healing potential with time were predicted using the FE limit (DCSE limit) aging model and the healing model, respectively. The input information for these material property models is listed in Table 4-4.

Table 4-4. Data for material property aging models

Parameter	Value
Aggregate % passing by weight (seive size)	100.0 (3/4 in.), 90.0 (3/8 in.), 60.2 (# 4), 4.8 (# 200)
Binder type	67-22
Mean annual air temperature, °F	60
Effective binder content, % by volume	12
Air void content, % by volume	7
Initial fracture energy, Kpa	2
Fracture energy aging parameter	3

Figure 4-18 shows the one-year temperature profile at the surface of the AC layer in the Washington D.C. area generated from the EICM. The first day shown in the figure corresponds to July 1st of the year. As an illustration, Figure 4-19 shows the estimated dynamic modulus at year one based on the temperature profile in Figure 4-18. The stiffness was calculated at a load frequency of 10 Hz (i.e., loading time 0.1 s).

The variation of FE limit, DCSE limit, tensile strength and maximum healing potential with age (and depth) are given in Figure 4-20.

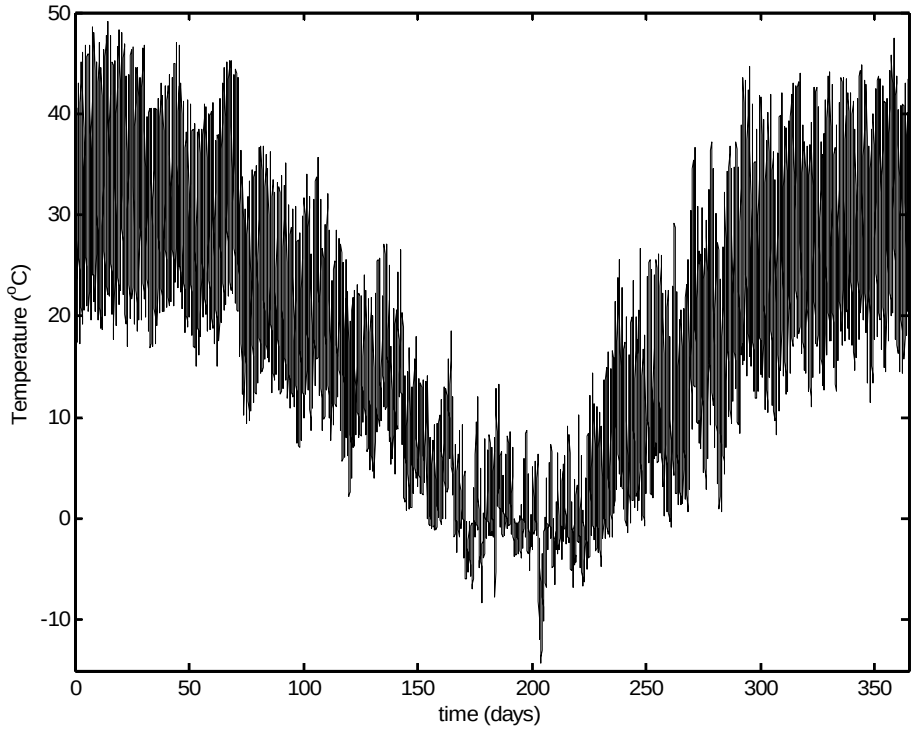

Figure 4-18. One-year temperature profile at the pavement surface (Washington D.C.)

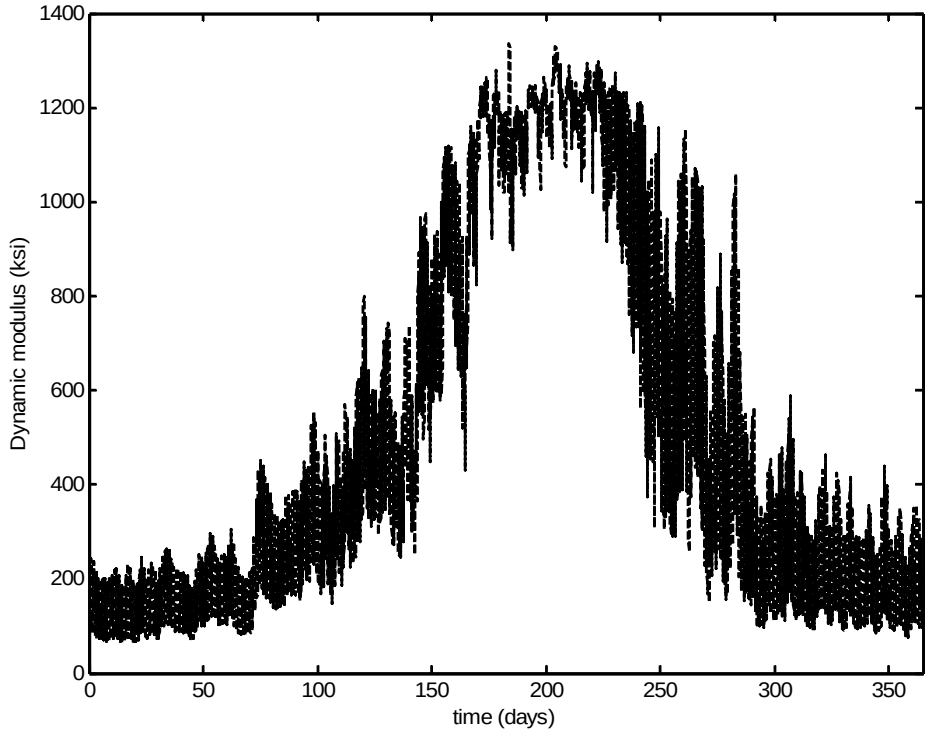

Figure 4-19. Variation of AC stiffness with time

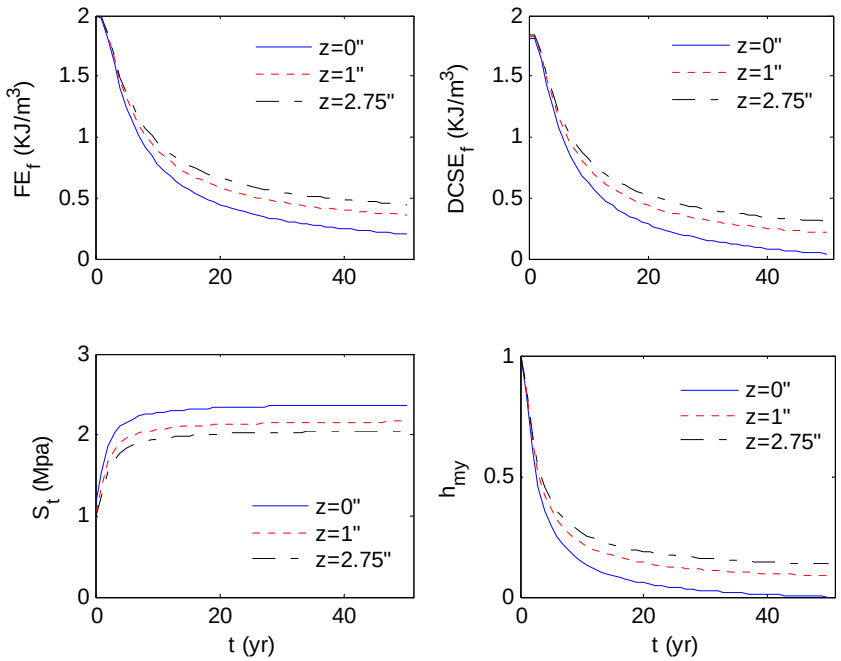

Figure 4-20. Variation of fracture and healing properties with age (and depth)

Traffic Information

The pavement section was assumed to be subjected to 18 kip single axle wheel load at a rate of 100 cycles per hour, which is equivalent to 17.5 million ESALs per 20 years.

Model Predictions without Thermally Induced Damage

In this section, predictions for crack initiation and propagation in the pavement section were made without activation of the thermal response model.

Stage one: crack initiation

Figure 4-21 gives the results of load induced damage accumulation versus time during Year 12. As shown, crack initiation occurred in early October of that Year. The total load passes leading to crack initiation is about 9.9 million ESALs, which were obtained by adding the load passes predicted in Year 12, i.e., 223,700 to the product of the yearly traffic (i.e., 0.876 million ESALs) and 11 (meaning the past 11 years).

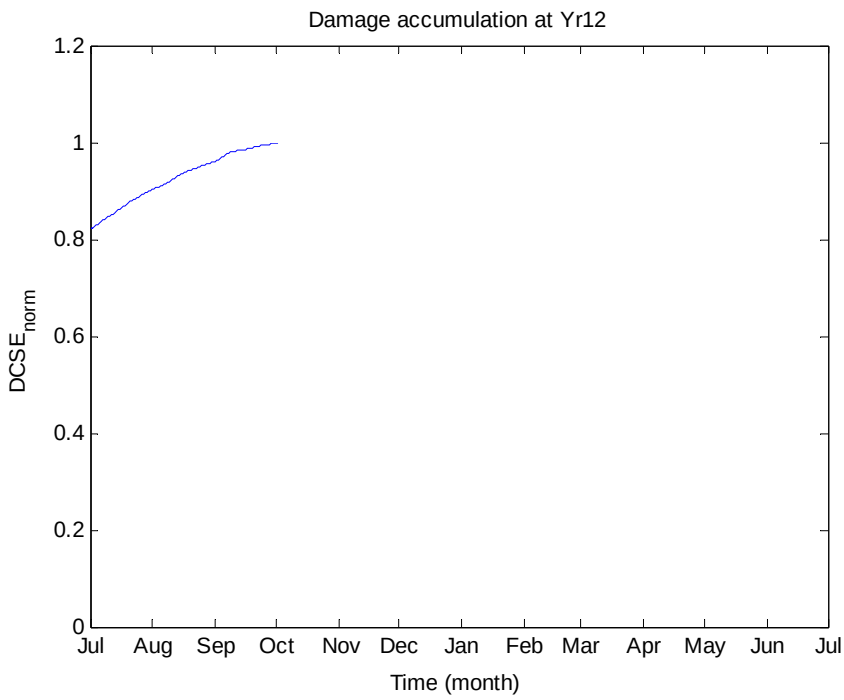

Figure 4-21. Prediction of crack initiation w/o thermally induced damage

Stage two: crack propagation

The predicted crack propagation without thermally induced damage is shown in Figure 4-22. It started at a slow rate for the first few process zones. Subsequently, it sped up and maintained a faster rate until it reached the critical crack depth (i.e., 2.5 in for this case). The process took about 9.5 years.

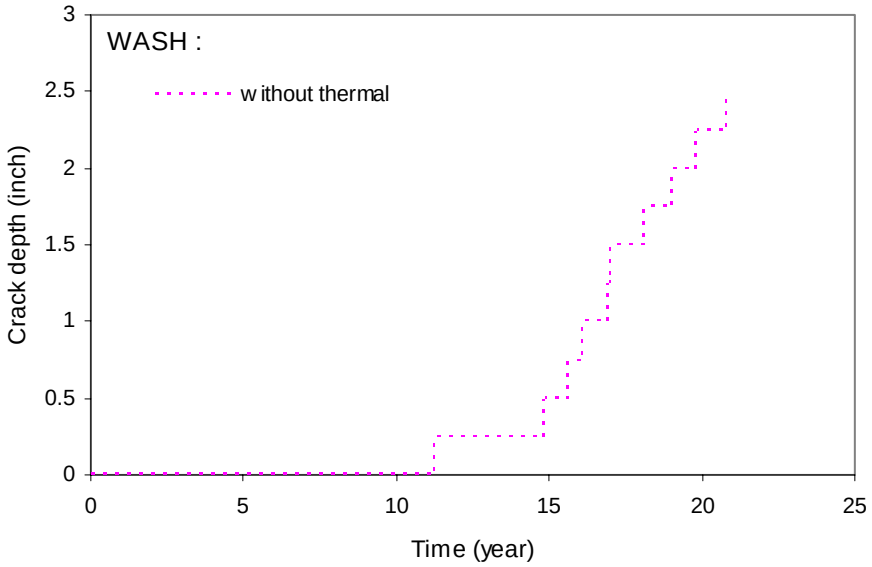

Figure 4-22. Prediction of crack propagation w/o thermally induced damage

Model Predictions with Thermally Induced Damage

Another set of predictions were made when both load and thermally induced damage were accounted in the performance model. The thermal effect on predicted cracking performance was then evaluated based on a comparison of these results with those of the prior section.

Stage one: crack initiation

Figure 4-23 gives the predicted thermal stresses at four depths of the AC layer using the thermal response model. As shown, the thermal stresses at any depth of the AC layer were almost negligible during warmer months (i.e., Jul. to Sep., and Apr. to Jun.), but they were kept at 10 psi during most of the cold times (i.e., the other half of the yearly period), during which significant amount of thermally induced damage can be generated. It can also be seen from the figure that thermal stresses decrease with depth.

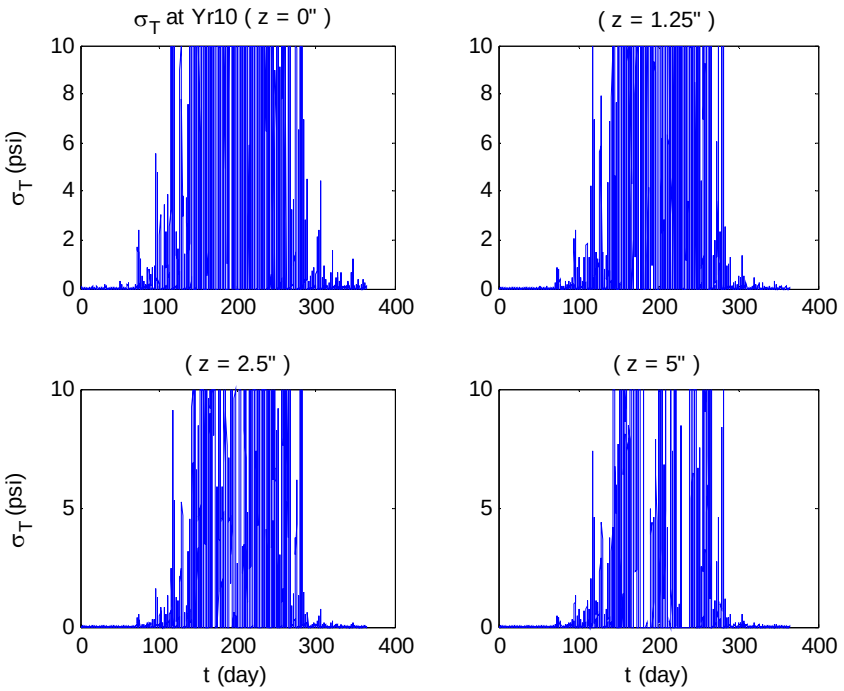

Figure 4-23. Predicted thermal tresses at four depths of AC layer during Year 10

The damage accumulation during Year 10 is shown in Figure 4-24. It can be seen that crack initiation occurred in early June of that Year. After accounting for loads applied in prior years, the total loads leading to crack initiation were about 8.7 million.

Stage two: crack propagation

Figure 4-25 shows the increment of crack depth with time when thermally induced damage was considered (refer to the solid line). Again, the crack propagated at a relatively low growth rate through the first few zones. It then accelerated until it reached the critical crack depth. The process took about 6.4 years. For comparison purpose, the prediction for crack depth versus time without considering thermally induced damage was also presented in the same figure (see the dashed line).

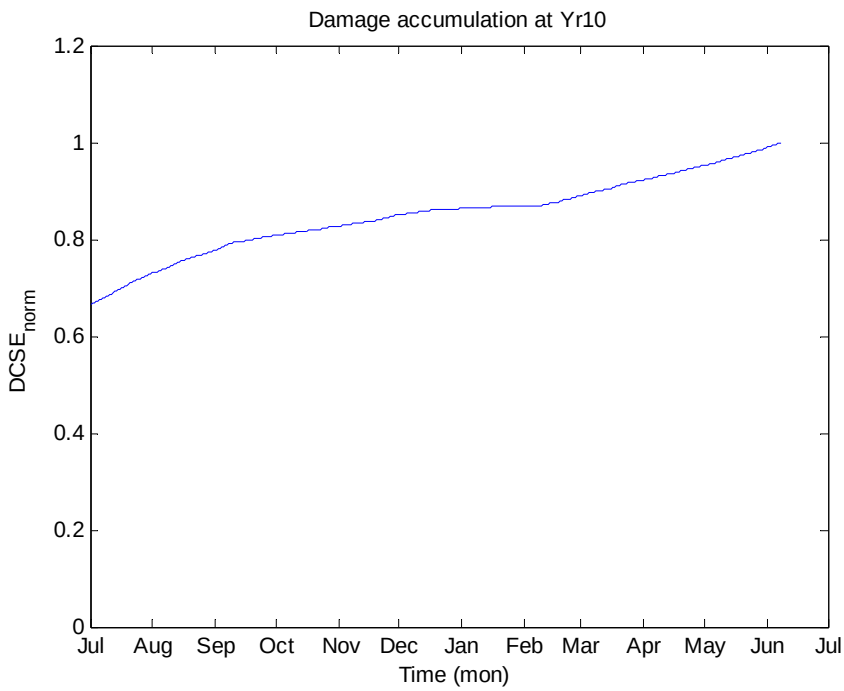

Figure 4-24. Prediction of crack initiation with thermally induced damage

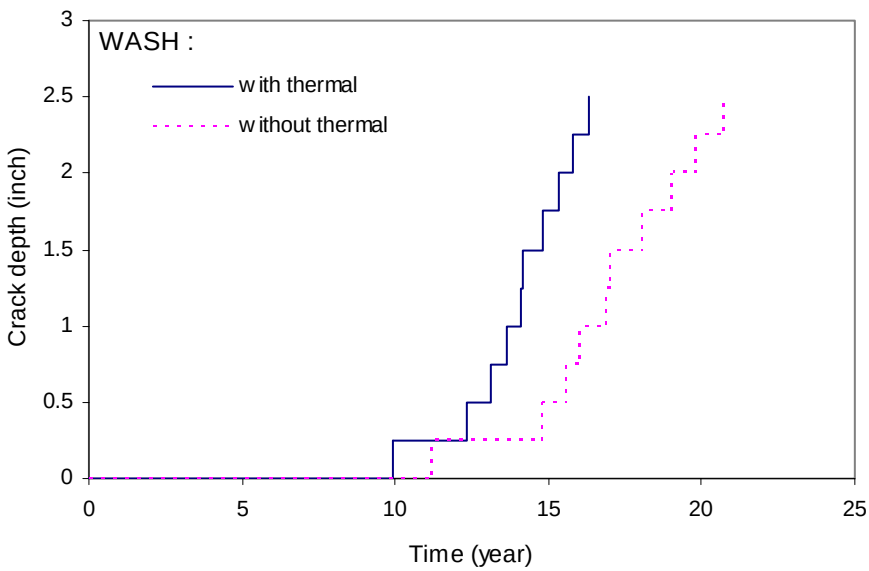

Figure 4-25. Prediction of crack propagation with and without thermally induced damage

Table 4-5 summarizes the predicted number of years (nyrs) and number of load passes (npas) leading to crack initiation, and location of the initial crack (xs) for two conditions: (a) with and (b) without thermally induced damage. It can be seen that without accounting for thermally induced damage, an additional 1.4 years or 1.2 million loads are needed to see

cracking in this pavement. Clearly, thermal effect cannot be ignored for accurate prediction of crack initiation.

Table 4-5. Thermal effect on crack initiation

WASH	nyrs	npas (x 10^6)	xs (in.)
a: with thermal	9.9	8.7	27.5
b: without thermal	11.3	9.9	27.5

Table 4-6 summarizes the predicted number of years (nyrs), number of load passes (npas), and total increment of crack depth (Δa) for these two conditions during the crack propagation stage.

Table 4-6. Thermal effect on crack propagation

WASH	nyrs	npas (x 10^6)	Δa (in.)
a: with thermal	6.4	5.6	2.25
b: without thermal	9.5	8.3	2.25

Without thermally induced damage, an additional 3.1 years or 2.7 million loads are required to complete the propagation stage. Therefore, the importance of incorporation of thermally induced damage in crack propagation was also emphasized. It is noted that the time for crack initiation will affect the propagation time, since FE limit (DCSE limit) reduces with age. For example, if the FE limit of Year 10 (when crack initiation was identified under condition (a)) was used as the starting FE value for predicting crack propagation under condition (b), additional time or loads are expected.

In summary, predicted top-down cracking performance of one pavement section in the Washington D.C. area was compared for two different conditions: with and without thermally induced damage. Based on the comparison for both crack initiation and propagation, it was found that thermal effect is important for an accurate prediction. Therefore, it is necessary to incorporate the thermal response model into the performance model. The results also indicated

that the FE limit (DCSE limit) aging model played an important role in determining the time of crack initiation and the average crack grow rate.

CHAPTER 5
MODEL EVALUATION: PARAMETRIC STUDY

The top-down cracking performance model was intended to predict crack initiation (time and location) as well as crack propagation (increase of crack depth or crack amount with time) for calibration and validation using real asphalt concrete pavements. However, in view of the complexity involved in the model, it was necessary to know how various factors affected predicted results and which factors had the strongest influence on performance. More importantly, it was crucial to identify factors that could alter the cracking mechanism used in the model (e.g., bending versus near-tire mechanism). Therefore, a parametric study was conducted using a broad range of input parameters to evaluate these factors. To limit the number of runs, the following conditions were assumed:

- The pavement structure used in the example for demonstration of the thermal effect was selected (see Chapter 4, Section Three). It consists of three layers: asphalt concrete (with three sub-layers), base and subgrade.
- The base thickness, and subgrade modulus and thickness were not changed for all analyses conducted. The Poisson's ratio for each of the layers was also kept same throughout the study.
- The variation in AC creep compliance was obtained by varying binder viscosity, i.e., by changing binder type only. Meanwhile, the other material characteristics (e.g., aggregate gradation, air void and effective binder content of asphalt mixture) that also influence creep compliance were not changed.

The conditions defined above reduced the input requirements to the following parameters. They are presented below according to three different categories:

- Material and structural properties including,
    - Initial fracture energy.
    - Fracture energy aging parameter.
    - Binder viscosity.
    - Base modulus.
    - AC layer thickness.

- Traffic volume: number of ESALs per year.
- Climatic information: a mean annual air temperature (MAAT) and its companion hourly temperature data at four different depths of AC layer for a whole year.

The values selected for each variable are presented in Table 5-1. For each variable, the value used in the example for demonstration of the thermal effect (Chapter 4, Section Three) is highlighted via a shaded area. The combination of these values (as shown in the shaded area) was used as a standard case. In other words, the example was adopted here as a standard case. Accordingly, the input parameters in Table 4-4 were used in conjunction with those of Table 5-1 to conduct this analysis.

Then, each parameter included in the analysis was individually varied relative to the values given in Table 5-1, while the remaining parameters were held constant at the values used for the standard case. In total, the influence of individual parameters was investigated using 16 cases including the standard one. However, interactions and combined effects were beyond the scope of the analysis.

Table 5-1. Range of parameters selected for sensitivity analysis

Variables	Values			
Initial Fracture Energy FE_i (Kpa)	2	5	10	
Fracture Energy Aging Parameter k_1	1	3	5	
Binder Type	58-28	67-22	76-22	
Base Modulus (Ksi)	20	40	60	
AC Layer Thickness (in)	2.5	5	7.5	10
Traffic Volume (10^6 ESALs per year)	0.175	0.438	0.876	
MAAT (°F)	50	60	75	

Effects of Material and Structural Properties

The material and structural properties under investigation included initial fracture energy, fracture energy aging parameter, binder viscosity, base modulus and AC layer thickness. The influence of each of them is discussed in the following subsections.

Effect of Initial Fracture Energy

The initial fracture energy is the starting value (also maximum value) of any fracture energy aging curve (see Figure 3-6). It also controls the degradation rate of any maximum healing potential aging curve (see Figure 3-9). Therefore, it was expected to have a strong influence on pavement cracking performance. To confirm the expected effect, a broad range of initial fracture energies was selected.

Plots of crack depth versus time predicted by the model for different values of initial fracture energy are shown in Figure 5-1. As shown, pavement with higher initial fracture energy exhibits better cracking performance, i.e., longer crack initiation time and propagation time. For pavements with the same AC layer thickness, comparison was also made with respect to an average crack growth rate, which was defined as,

$$C_t = \frac{CD_c - CD_i}{t_p} \tag{5-1}$$

where, C_t is average crack growth rate, CD_c is critical crack depth, CD_i is initial crack depth of 0.25 inch, and t_p is crack propagation time to the critical crack depth.

Figure 5-2 shows the predicted average growth rate for different FE_i values. It is clear that a higher FE_i value leads to a lower crack growth rate (i.e., better cracking performance).

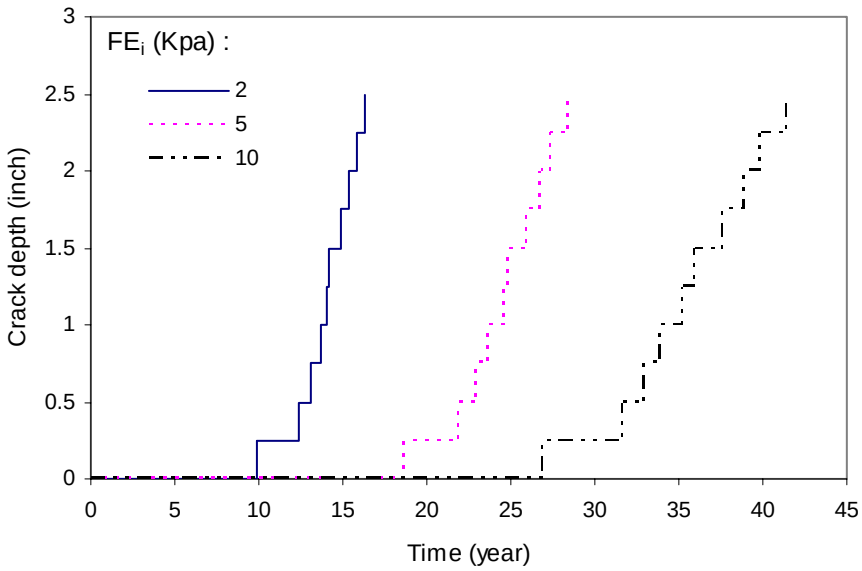

Figure 5-1. Effect of initial fracture energy on cracking performance

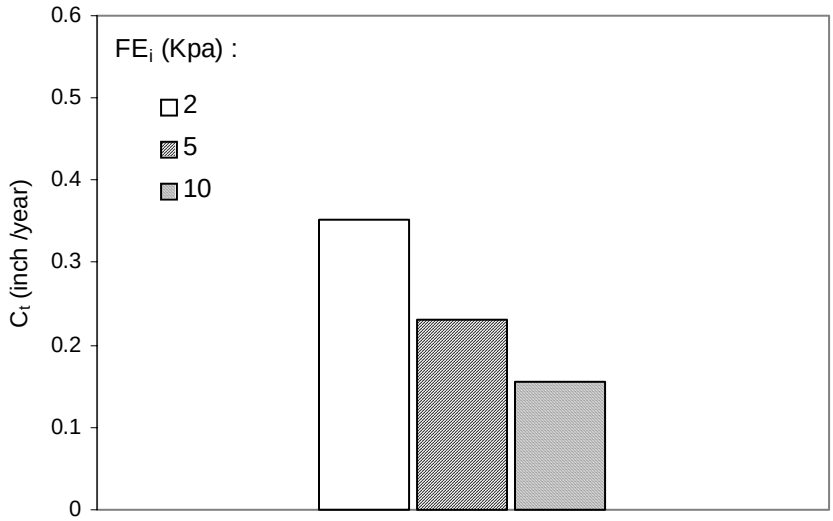

Figure 5-2. Effect of initial fracture energy on average crack growth rate (C_t)

Effect of Fracture Energy Aging Parameter

Fracture energy aging parameter k_1 is an input parameter that governs the shape of the fracture energy aging curve. For a constant initial fracture energy, a larger k_1 value corresponds to a lower rate of degradation in fracture energy with aging (i.e., higher resistance to fracture, see Figure 3-7).

The effect of the fracture energy aging parameter is shown in Figures 5-3 and 5-4. As shown, the increase of k_1 value results in longer time to crack initiation (Figure 5-3) and a lower average crack growth rate (Figure 5-4).

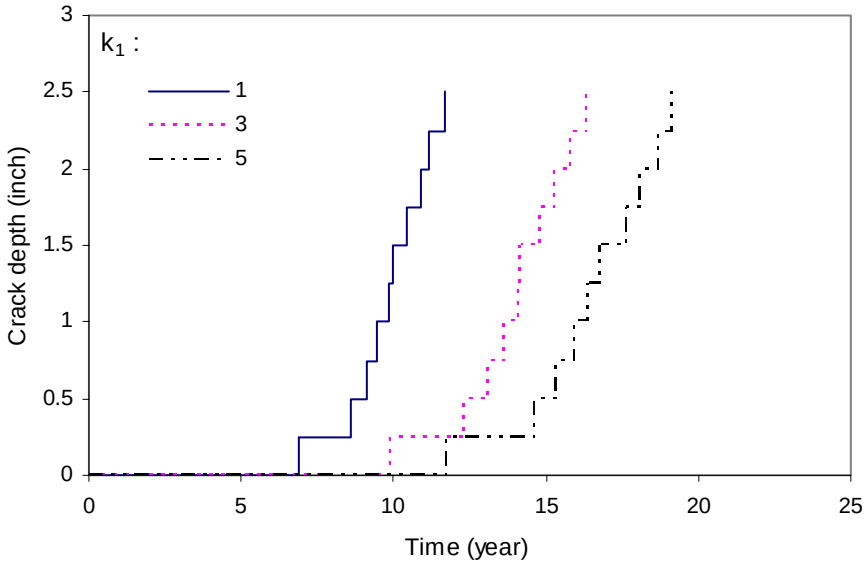

Figure 5-3. Effect of fracture energy aging parameter on cracking performance

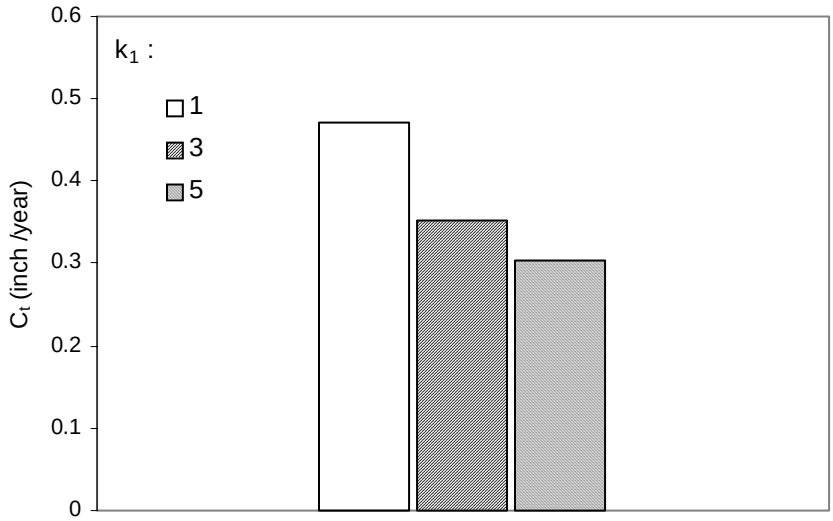

Figure 5-4. Effect of initial fracture energy on average crack growth rate (C_t)

Effect of Binder Viscosity

A typical range of binder types (from soft to stiff) were selected for the analysis. The predicted cracking performance is presented in Figures 5-5 and 5-6, which shows that crack initiation time is not affected by the change in binder viscosity (Figure 5-5), and a softer binder results in only a slightly higher crack growth rate (Figure 5-6). This appears to be associated with the higher creep rate of the mixture with the softer binder. However, as binder stiffness also affects AC stiffness, a softer binder leads to lower AC stiffness, which can counter-balance the effect of higher creep rate. Therefore, the overall change in the average crack growth rate is small. In other words, pavement cracking performance is not sensitive to the change of binder viscosity. Of course, it must be emphasized that this result does not consider that softer binder may increase mixture fracture energy, which was kept constant in this analysis.

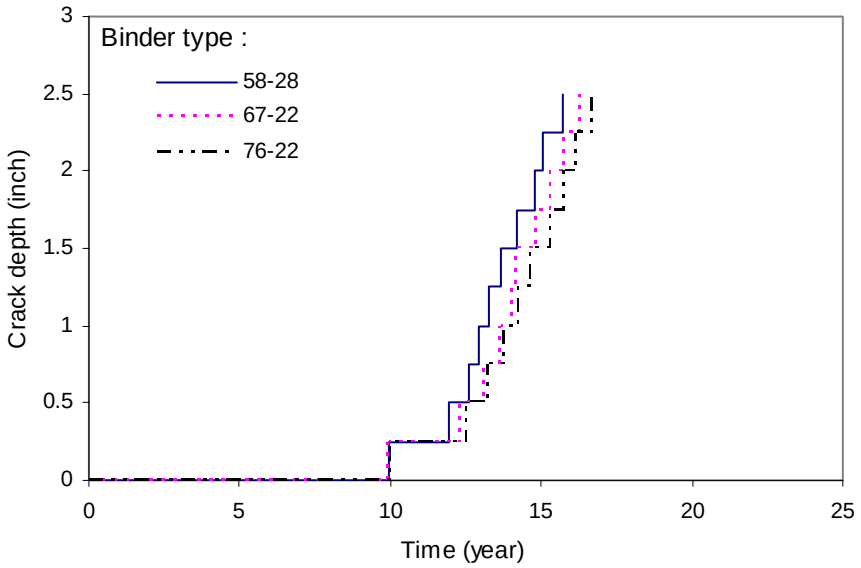

Figure 5-5. Effect of binder type on cracking performance

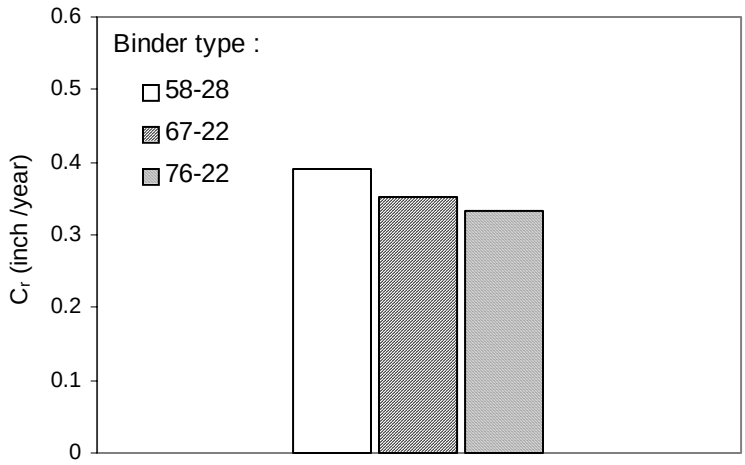

Figure 5-6. Effect of binder type on average crack growth rate (C_t)

Effect of Base Modulus

The effect of base modulus was investigated using the material properties presented in Table 4-4 and the values of base modulus given in Table 5-1. Pavement cracking performance predicted by the model is given in Figures 5-7 and 5-8, which shows that the pavement with higher base modulus has better performance, i.e., longer crack initiation time (Figure 5-7) and lower crack growth rate (Figure 5-8). This was expected because a stiffer base tends to reduce the load induced tensile stresses at the surface of pavement. For the range of base modulus values studied, the effect of base modulus is fairly strong.

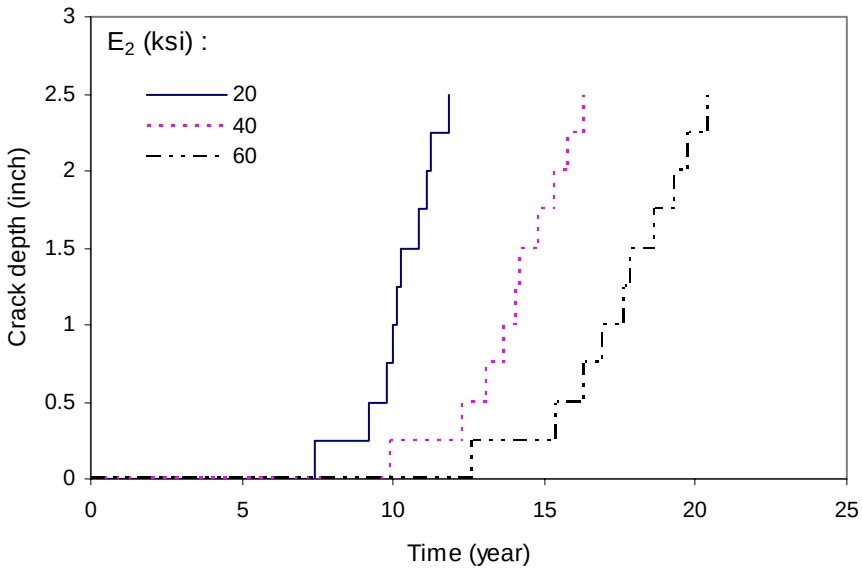

Figure 5-7. Effect of base modulus on cracking performance

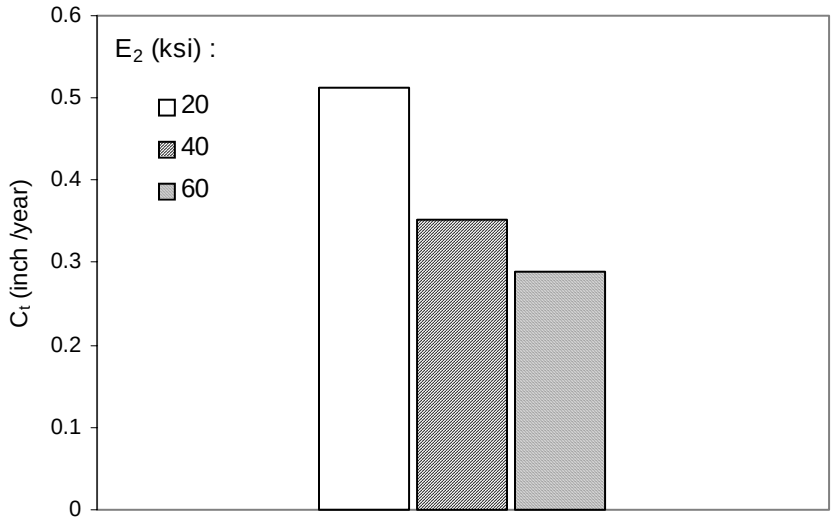

Figure 5-8. Effect of base modulus on average crack growth rate (C_t)

Effect of AC Layer Thickness

A wide range of AC layer thickness values were selected for this analysis:

- 2.5 in for a thin AC layer.
- 5 in for a medium thickness AC layer.
- 7.5 in for a thick AC layer.
- 10 in for a very thick AC layer (i.e., a full depth AC pavement).

The predicted pavement cracking performance for the first three AC layer thickness values are shown in Figures 5-9 and 5-10, which shows that the pavement with thicker AC layer had better cracking performance, i.e., longer crack initiation time (Figure 5-9) and longer crack propagation time (Figure 5-10).

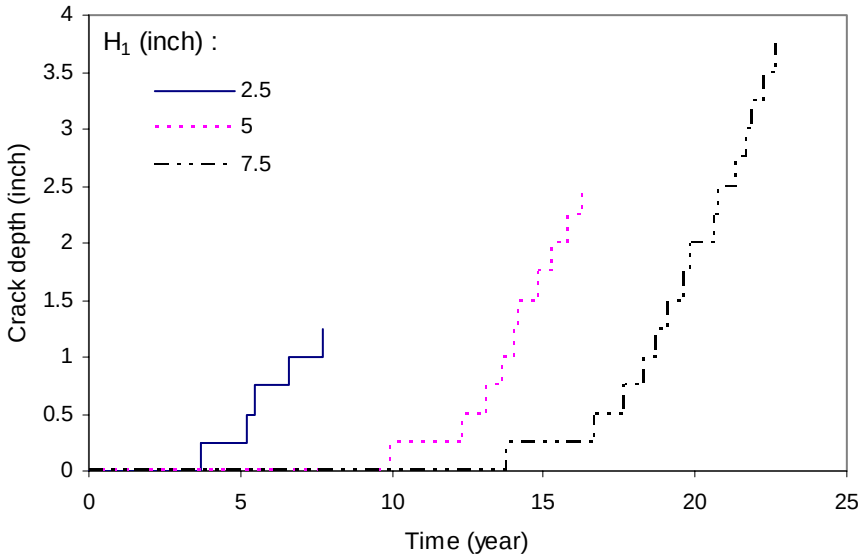

Figure 5-9. Effect of AC layer thickness on cracking performance

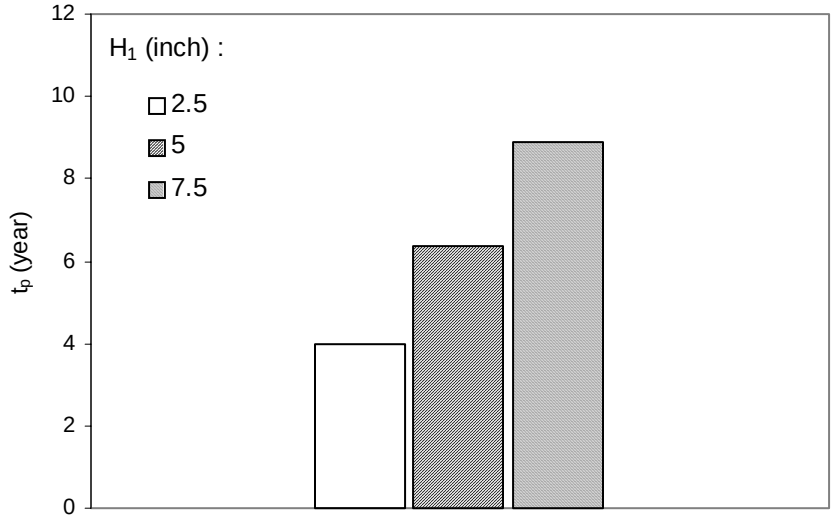

Figure 5-10. Effect of AC layer thickness on crack propagation time (t_p)

However, the predicted location of the initial crack for the thick AC layer was found more than 36 inch from the center of one tire. In this circumstance, the initial crack was actually predicted to be either in the compressive zone of the other tire or in the other traffic lane, as indicated by Figure 5-11. In other words, the prediction was not realistic. Therefore, the bending mechanism used for model prediction may not be appropriate for the thick AC layer pavement.

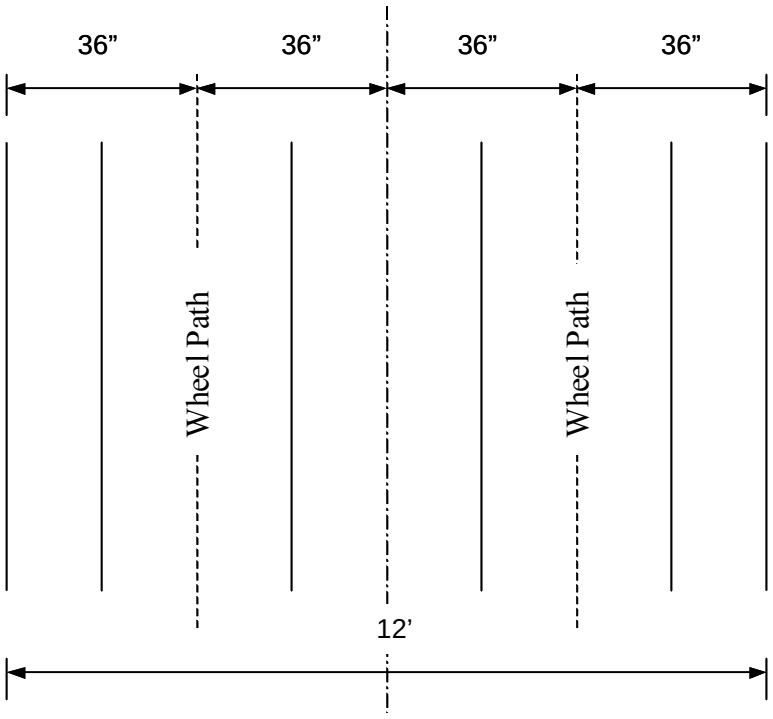

Figure 5-11. Schematic drawing for one typical traffic lane

The near-tire mechanism, accounting for shear-induced tension at the tire edge, was thus considered for use in thick AC layer. According to this mechanism, the location of initial crack is right next to the tire edge. The major driving force for crack initiation and propagation is the shear-induced principal tensile stress. However, a crack growth simulation tool based on this mechanism was not available at this time. Therefore, the CGS module was used as a surrogate to predict crack growth with time. Due to the localized property of the shear-induced tension at the tire edge, the critical crack depth was redefined to be one fourth of the AC layer depth. Then, a

simplified model with the near-tire mechanism was used to predict cracking performance for the 7.5 inch thick AC layer and a 10 inch full depth AC pavement.

The predicted cracking performance is given in Figure 5-12. As shown, both pavements have identical performance, i.e., same crack initiation time and similar crack propagation time. This is expected because the principal tensile stress of 25 psi predicted based on actual tire stresses was the same for both pavements. In fact, this stress was found to be independent of AC thickness and the stiffness ratio of AC to base layer.

A comparison of Figure 5-12 and Figure 5-9 appears to indicate that thick pavements may perform even worse than a pavement with a medium thickness AC layer. However, it should be noted that some potential factors affecting the near-tire mechanism are not addressed in the current model, including effects of wander and stress state. Both will result in less damage than currently predicted. Therefore, the comparison may not be accurate without considering these factors.

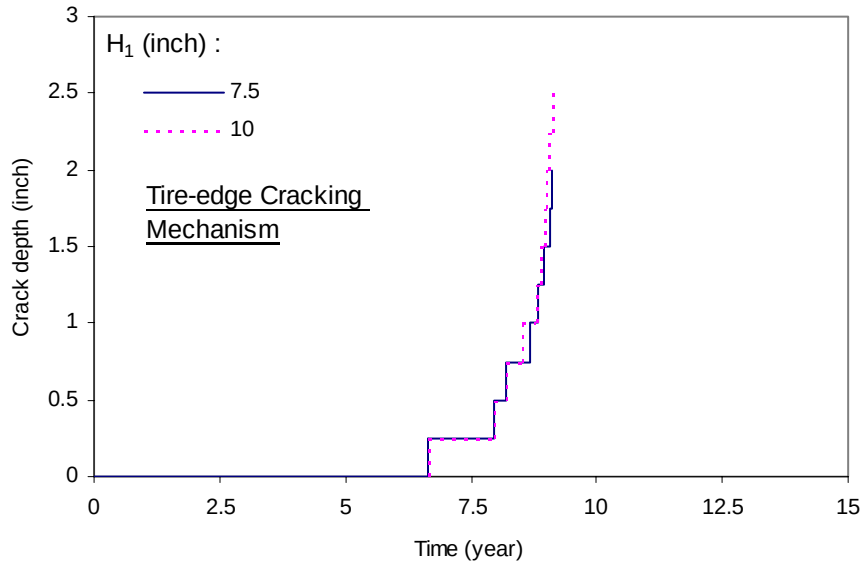

Figure 5-12. Predictions based on tire-edge cracking mechanism

Effect of Traffic

As shown in Table 5-1, three traffic levels (in million ESALs per year) were selected for this analysis:

- High traffic: 0.876
- Medium traffic: 0.438
- Low traffic: 0.175

The high traffic level is equivalent to 100 ESALs in an hour. Accordingly, the medium and low traffic levels correspond to 50 and 20 ESALs per hour. The predicted pavement performance is shown in Figures 5-13 and 5-14. As expected, the pavement subjected to the highest traffic level had the worst performance, i.e., shortest time to crack initiation (Figure 5-13) and highest crack growth rate (Figure 5-14). Overall, the effect of traffic is strong.

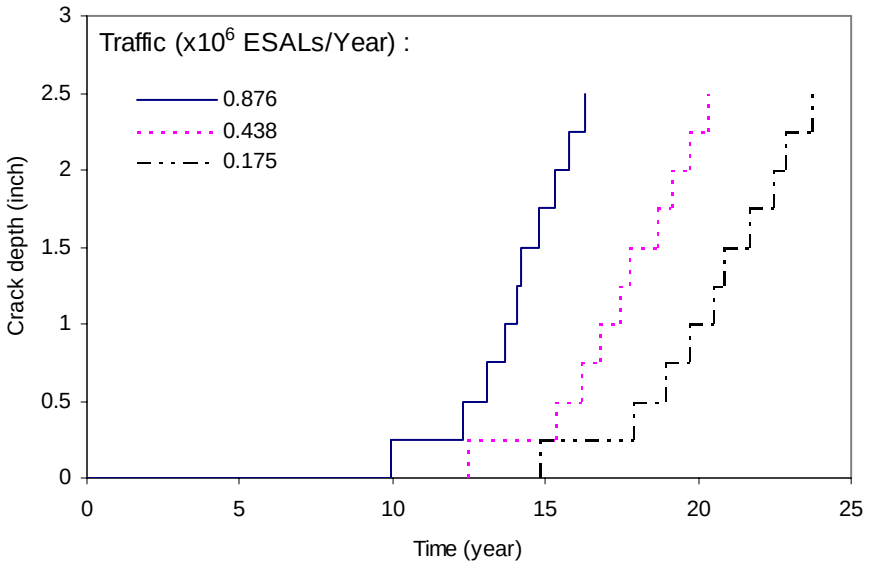

Figure 5-13. Effect of traffic volume on cracking performance

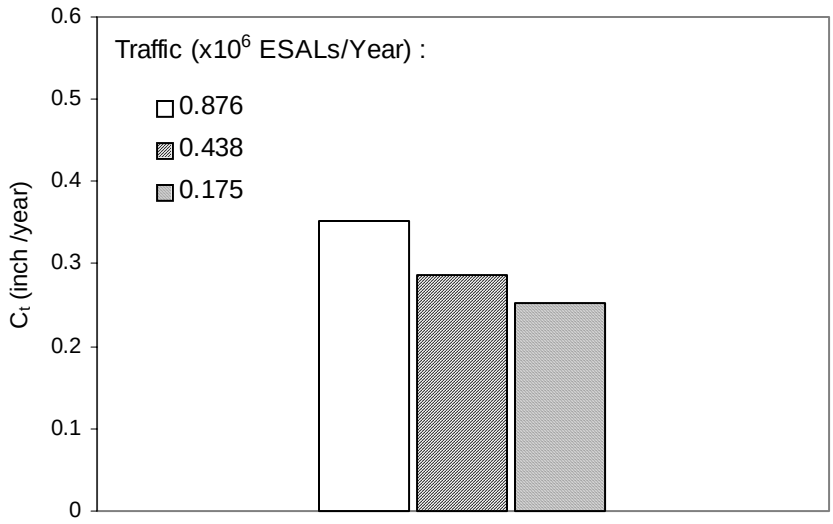

Figure 5-14. Effect of traffic volume on average crack growth rate (C_t)

Effect of Climate

Three typical climatic environments were selected for this analysis:

- Non-freeze (NF) environment, as represented by the climate of Melrose, FL.
- Freeze-thaw (FT) environment as of Washington, D.C.
- Hard-freeze (HF) environment as of Fargo, ND.

The mean annual air temperature (MAAT) value for each of the climatic environment was given in Table 5-1. Under each climate, the MAAT value and the corresponding temperature data file containing hourly temperature history at four depths of the AC layer for a whole year were used as input for model prediction. The predicted pavement performance is shown in Figures 5-15 and 5-16. As shown, the pavement cracking performance under both the FT and HF environments appears to be identical. Meanwhile, under the NF environment, the pavement exhibits a slightly later crack initiation (Figure 5-15), but a higher crack growth rate (Figure 5-16) as compared to the performance under the other two environments. Overall, the effect of climatic environment (more specifically, temperature) is minimal.

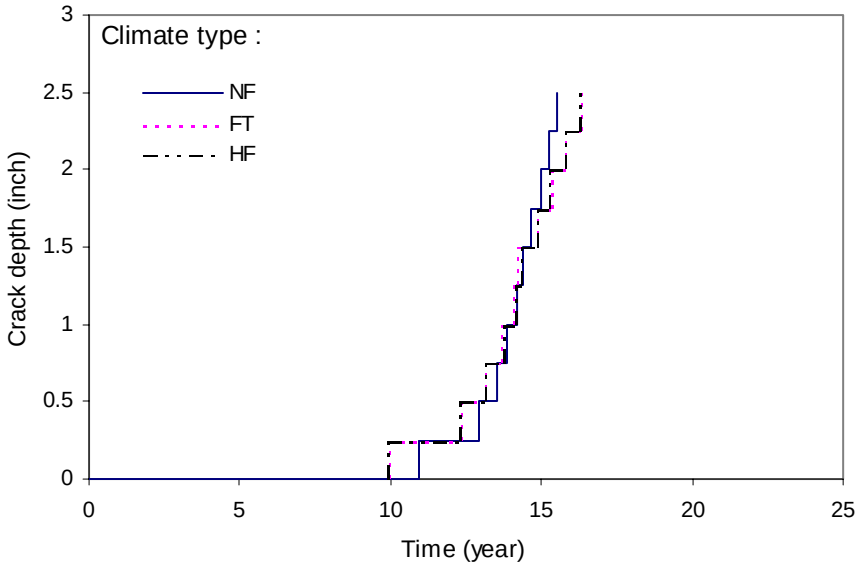

Figure 5-15. Effect of climatic environment on cracking performance

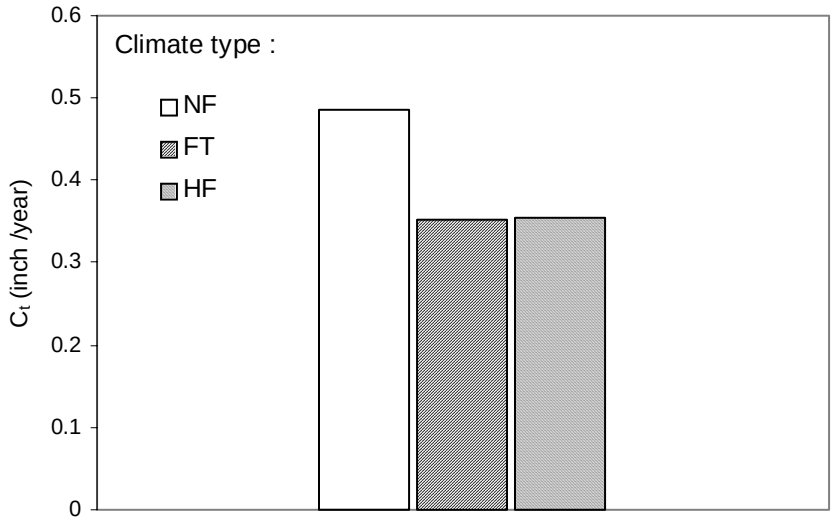

Figure 5-16. Effect of climatic environment on average crack growth rate (C_t)

This was expected because the influences of climatic environment on damage development in the pavement are two-sided: on one side, colder weather leads to higher thermal stresses and thus higher thermally induced damage. However, it should be noted that transverse, as opposed to longitudinal, thermal stresses were used to compute thermally induced damage in the thermal response model (Chapter 3, Section Three). Therefore, the resulting thermally induced damage is

not as high as that caused by longitudinal thermal stresses. On the other side, colder weather results in lower creep rate and thus lower load induced damage.

When both thermally induced damage and load induced damage are combined, the two-sided effects of climatic environment counter-balanced each other. To verify this point, the thermal response sub-model was turned off in the top-down cracking performance predictive system, which was then used to predict cracking performance for the same pavement under these three climatic environments. In other words, the climate was allowed to influence load induced damage only. The results are presented in Figures 5-17 and 5-18. As shown, the climate did not have much influence on crack initiation time (Figure 5-17). However, it did strongly affect the crack growth rate (Figure 5-18). As can be seen, pavement under a warmer climatic environment has a higher crack growth rate. This was expected because the warmer time of a yearly period is longer under warmer climate, which subjects the pavement to a high creep rate for longer time and thus more damage.

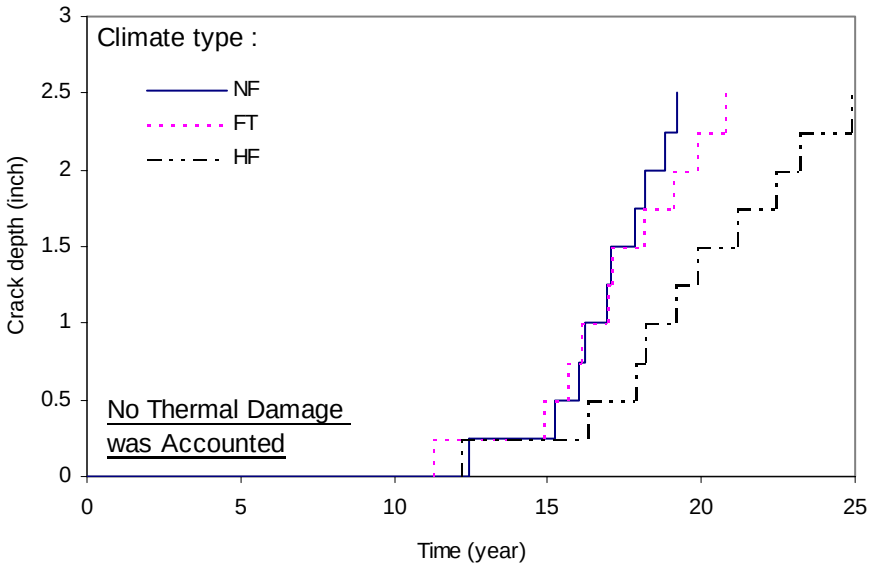

Figure 5-17. Effect of climatic environment (w/o thermally induced damage) on cracking performance

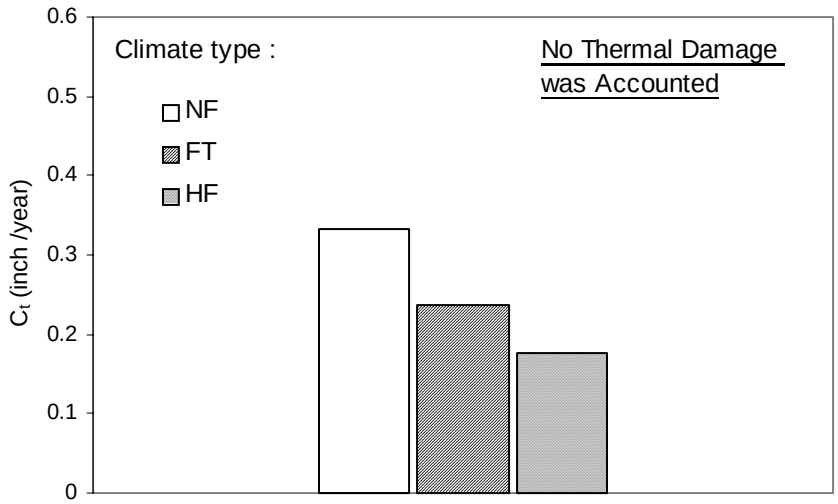

Figure 5-18. Effect of climatic environment (w/o thermally induced damage) on average crack growth rate (C_t)

CHAPTER 6
MODEL CALIBRATION AND VALIDATION

The top-down cracking performance model needed to be calibrated and validated to determine whether the model could reasonably predict cracking performance of asphalt concrete pavement using pavement material and structural properties, traffic volume and climatic information.

Summary of Top-down Cracking Performance Model Data

Calibration of the top-down cracking performance model was conducted by matching as closely as possible top-down cracking predictions with observed cracking performance, more specifically crack initiation time in the field. To complete the calibration, input data were needed to make top-down cracking predictions. In addition, observed field performance of each pavement section was required for comparison to model predictions. This section presents the data used for calibration of the performance model.

Selection of Pavement Sites

Thirteen pavement sections were evaluated as part of this study. These sections were selected based on quality of data in terms of both laboratory testing and field observation. Only sections for which reliable and high quality material property and pavement performance data were available were used for calibration/validation.

According to the climatic condition, these pavement sections fell into two groups. Group I included eleven sections under Non-Freeze climate of Florida. Meanwhile, Group II had two sections under Hard-Freeze climate of Minnesota. The locations of test sections of Groups I and II are presented in Tables 6-1 and 6-2, respectively. As can be seen, Group I was the primary group, containing most of the pavement sections, while Group II was a supplement. The

inclusion of Group II was intended to represent pavement performance under a different climatic condition.

However, according to the parametric study presented in Chapter Five, AC layer thickness was found to govern the cracking mechanism. For pavements with thin to medium thickness AC layer as those of Group I (see Table 6-6), the bending mechanism was appropriate. Meanwhile, for full-depth AC pavements as those of Group II (see also Table 6-6), the near-tire mechanism had to be used. To avoid possible inconsistency due to different mechanisms, the pavements in Group II were not used in the model calibration. However, the calibrated performance model was used to predict performance of pavements in Group II to show the potential of the model for including both cracking mechanisms in future developments.

Table 6-1. Field test sections under Non-Freeze climate of Florida

Section Number	Section Name	Code	County	Section Limits
1	Interstate 75 Section 1	I75-1A	Charlotte	MP 161.1 - MP 171.3
2	Interstate 75 Section 1	I75-1B	Charlotte	MP 149.3 - MP 161.1
3	Interstate 75 Section 3	I75-3	Lee	MP 131.5 - MP 149.3
4	Interstate 75 Section 2	I75-2	Lee	MP 115.1 - MP 131.5
5	State Road 80 Section 1	SR 80-1	Lee	From Hickey Creek Bridge To East of Joel Blvd.
6	State Road 80 Section 2	SR 80-2	Lee	From East of CR 80A To West of Hickey Creek Bridge
7	Interstate 10 Section 8	I10-8	Suwannee	MP 15.144 - MP 18.000
8	Interstate 10 Section 9	I10-9	Suwannee	MP 18.000 - MP 21.474
9	State Road 471	SR471	Sumter	The northbound lane three miles north of the Withlacoochee River
10	State Road 19	SR19	Lake	The southbound lane five miles south of S.R. 40
11	State Road 997	SR997	Dade	The northbound lane 7.6 miles south of US-27

Table 6-2. Field test sections under Hard-Freeze climate of Minnesota

Section Number	Section Name	Code	Location
12	Interstate 94 Cell 4	I94-4	located near Albertville, Minnesota (40 miles northwest of the Twin Cities)
13	Interstate 94 Cell 14	I94-14	located near Albertville, Minnesota (40 miles northwest of the Twin Cities)

Data Obtained from SuperPave IDT

The Superpave indirect tensile test (IDT) developed as part of the Strategic Highway Research Program (SHRP) was used to determine tensile properties on field cores obtained from the 13 test sections. The Superpave IDT includes three types of tests: resilient modulus, creep compliance, and tensile strength.

- The resilient modulus test was performed in a load-controlled mode by applying a repeated haversine waveform load to the specimen for a period of 0.1 second followed by a rest period of 0.9 seconds. The load was selected to keep the repeated horizontal strain between 100 and 300 micro-strain during the test (49). The resilient moduli of mixtures determined at 10°C are presented in Table 6-3. They represent the mixture property at the age when coring was conducted.

- The creep compliance test was also performed in the load-controlled mode by applying a monotonic static load to the specimen for a period of 1000 seconds. The load is selected to maintain the accumulative horizontal strain below 1000 micro-strain (50). The creep compliance master curve parameters determined based on tests conducted at 0, 10, and 20°C are presented in Table 6-4.

- The strength test was performed in a displacement-controlled mode. A loading rate of 50 mm/min was used. The fracture properties determined at 10°C are also shown in Table 6-3.

Table 6-3. Data from SuperPave IDT resilient modulus and tensile strength tests at 10°C

Section Code	M_R (Gpa)	S_t (Mpa)	ε_f ($\mu\varepsilon$)	FE_f (Kpa)	$DCSE_f$ (Kpa)	Age (year)
I75-1A	11.14	1.65	1028.05	1.1	1.0	15
I75-1B	10.91	2.01	1437.44	2.0	1.8	14
I75-3	11.58	1.68	715.74	0.8	0.7	15
I75-2	10.29	1.89	1066.72	1.3	1.1	14
SR80-1	13.39	1.59	495.27	0.3	0.2	16
SR80-2	13.45	2.39	679.15	1.0	0.8	19
I10-8	9.85	1.56	386.00	0.4	0.3	7
I10-9	10.21	1.27	415.00	0.4	0.3	7
SR471	7.67	1.79	2040.00	2.5	2.3	3
SR19	9.30	1.71	1338.00	1.6	1.4	3
SR997	11.74	2.33	594.00	0.9	0.7	40
I94-4	8.18	1.35	1203.56	1.1	1.0	13
I94-14	9.44	1.78	1760.25	2.4	2.2	13

Table 6-4. Data from SuperPave IDT creep compliance tests at 0, 10, and 20°C

Section Code	m	D_1 (1/Gpa)	AT(3)*	AT(2)	AT(1)
I75-1A	0.441	0.027	251.19	35.48	1
I75-1B	0.471	0.029	177.83	19.95	1
I75-3	0.485	0.022	281.84	14.13	1
I75-2	0.460	0.021	562.34	56.23	1
SR80-1	0.445	0.014	354.81	25.12	1
SR80-2	0.368	0.014	501.19	35.48	1
I10-8	0.441	0.013	112.202	8.913	1
I10-9	0.503	0.006	141.254	14.125	1
SR471	0.783	0.001	223.872	63.096	1
SR19	0.595	0.012	89.125	8.913	1
SR997	0.349	0.019	63.096	3.981	1
I94-4	0.462	0.018	–	44.668	1
I94-14	0.456	0.019	–	79.433	1

*AT(3) denotes the inverse of shift factor at the highest temperature.

Data for Material Property Model

The material property model consists of four sub-models: AC stiffness (creep compliance) aging model, strength aging model, fracture energy (dissipated creep strain energy) aging model, and healing model (refer to Chapter 3, Section Two).

The AC stiffness aging model estimates the stiffness of the asphalt mixture as a function of temperature and time. The input information for this model is given below:

1) Percent passing 3/4, 3/8, #4, and #200 sieves by weight.
2) Binder type and mean annual air temperature (MAAT).
3) Effective binder content (% by volume) and air void (% by volume).

The values used for above parameters are shown in Table 6-5.

The AC strength aging model uses the stiffness predicted by the stiffness aging model and the correlation between stiffness and strength to calculate the tensile strength of asphalt mixture.

Table 6-5. Data used by the material property model

Section Code	Percent passing by weight 3/4 in	3/8 in	# 4	# 200	V_{beff} (%)	V_a (%)	MAAT (°F)	Binder type
I75-1A	100.0	91.8	73.6	5.9	10.7	5.4	75	67-22
I75-1B	100.0	93.7	74.6	5.6	10.7	3.2	75	67-22
I75-3	100.0	86.2	65.1	5.5	8.2	7.2	75	67-22
I75-2	100.0	92.5	68.9	5.0	8.4	6.9	75	67-22
SR80-1	100.0	80.4	59.0	5.8	8.6	5.7	75	67-22
SR80-2	100.0	84.8	64.4	6.2	8.9	7.5	75	67-22
I10-8	100.0	90.0	60.2	4.8	10.3	8.7	75	67-22
I10-9	100.0	90.0	60.2	4.8	9.1	9.9	75	67-22
SR471	100.0	90.0	60.2	4.8	13.3	5.7	75	67-22
SR19	100.0	90.0	60.2	4.8	14.2	4.8	75	67-22
SR997	100.0	90.0	60.2	4.8	11.4	7.6	75	67-22
I94-4	100.0	82.1	65.6	5.2	10.3	4.4	50	58-28
I94-14	100.0	83.4	68.3	5.0	11.1	3.7	50	58-28

The fracture energy aging model also uses the stiffness predicted by the stiffness aging model, but in a normalized form. The model has two unknowns: the aging parameter k_1 and the initial fracture energy FE_i. Of the two unknowns, k_1 was determined from the calibration effort. Meanwhile, FE_i can be determined from unaged cores using SuperPave IDT tests. However, since unaged mixture was not available for the field sections used in this study, FE_i was back-calculated from tests performed on aged cores. As an example, the FE limit aging curve (including FE_i) determined based on the FE_f of 1.1 Kpa measured at an age of 15 years for test section I75-1A (assuming a k_1 value of 3) is shown below,

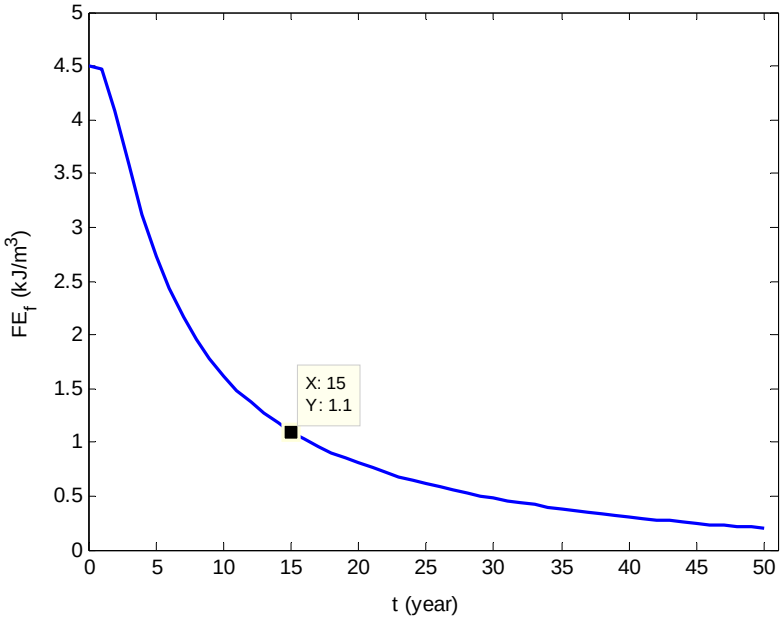

Figure 6-1. Determination of FE limit aging curve (including FE_i) based on measured FE from aged cores for test section I75-1A

The healing model has three components: the maximum healing potential aging model, and two criteria for determination of daily-based and yearly-based healing:

- The maximum healing potential aging model uses the normalized stiffness and initial fracture energy to estimate the loss of maximum healing potential due to aging.
- The criterion for determination of daily-based healing h_{dn} uses the lowest stiffness S_{low} of any day predicted by the stiffness aging model to determine the healing potential of that day. The daily-based healing h_{dn} is bounded by zero and the maximum value h_{ym} determined by the maximum healing potential aging model. Meanwhile, the S_{low} of any day is bounded by two critical values S_{cr1} and S_{cr2}, which were determined to be 320 and 2,000 ksi (see Chapter 4, Section Two).
- The criterion for determination of yearly-based healing h_{yn} is identical to the criterion for daily-based healing except an averaged daily lowest stiffness S_{lowa} for a prolonged period was used instead of S_{low} to obtain the healing potential of any year.

Data for Pavement Response Model

The pavement response model consists of two sub-models: (i) load response model, and, (ii) thermal response model (refer to Chapter 3, Section Three).

The load response model estimates load-induced stresses due to traffic loads. This model requires the following input parameters:

1) Layer thickness of AC, base, and subbase.
2) Modulus of base, subbase, and subgrade.
3) Poisson's ratio of AC, base, subbase, and subgrade.
4) Yearly average traffic volume (in ESALs).
5) Hourly temperatures within the AC layer.
6) The master creep compliance curve, as obtained via the IDT creep compliance tests.

The values used for parameters listed in 1), 2), and 4) are shown in Table 6-6. Poisson's ratios of 0.3, 0.35, 0.35, and 0.4 were assumed for AC, base, subbase, and subgrade, respectively. The hourly pavement temperatures were estimated by the enhanced integrated climatic model (EICM) using typical pavement material and structural properties and local climatic information.

Table 6-6. Data used by the pavement response model

Section	Layer thickness (in)			Layer modulus (ksi)			Yearly traffic
Code	AC	Base	Sub-base	Base	Sub-base	Sub-grade	(10^3 ESAL)
I75-1A	6.54	12	12	54.8	50.1	30.1	573
I75-1B	6.24	12	12	63.6	51.4	36.1	558
I75-3	6.48	12	12	59.6	34.8	36.2	674
I75-2	7.42	12	12	107.4	90.3	31.4	576
SR80-1	3.38	12	12	51.3	40.0	39.7	221
SR80-2	6.30	12	12	57.3	45.6	18.8	207
I10-8	7.20	12	12	55.7	54.5	38.9	392
I10-9	7.40	12	12	65.2	41.4	46.6	392
SR471	2.58	12	12	43.0	34.0	33.6	26
SR19	2.40	12	12	50.7	13.0	12.6	51
SR997	2.18	12	12	109.0	53.0	52.7	89
I94-4	9.10	–	–	–	–	3.2	488
I94-14	10.90	–	–	–	–	3.2	782

The thermal response model estimates thermally induced stresses caused by changes in pavement temperatures. This model requires the following input parameters:

1) Thickness of AC layer.
2) The master relaxation modulus curve, as obtained via the IDT creep compliance tests.
3) Hourly pavement temperatures within the AC layer.
4) Coefficient of thermal contraction of the asphalt concrete mixture.

The values used for parameters listed in 1) to 3) were covered by the input for load response model. The coefficient of thermal contraction was assumed to be 1.2E-5 ε/°C for all test sections of this study.

Data for Pavement Fracture Model

The pavement fracture model consists of three sub-models: (i) crack initiation model, (ii) crack growth model, and (iii) crack amount model (refer to Chapter 3, Section Four).

The crack initiation model uses the load-induced and thermal-induced stresses predicted by the pavement response model, and the rule for determination of crack initiation to predict crack initiation time and location. During the process, the mixture fracture and healing properties determined by the material property model are also required.

The crack growth model uses the load-induced stresses on the basis of the 2-D DDBE program, thermally induced stresses predicted by the pavement response model and stress intensity function, and the rule for determination of crack propagation to compute increase of crack depth with time. Similarly, the mixture fracture and healing properties determined by the material property model are required during the process.

The crack amount model converts the crack depth versus time relationship predicted by the crack growth model to crack amount versus time relationship.

Observed Pavement Performance Data

The input data presented in the previous sub-sections was used to make performance predictions for each of the 13 test sections in two phases. During phase one, the predictions for

the eleven sections of Group I were compared with observed performance to calibrate the model. Therefore, the observed field performance for each of the sections was also required, which was obtained via following two resources:

- A field trip was made to each test section to observe and photograph its performance and take cores in 2003. The cracked sections exhibited a moderate amount of cracking, while the uncracked sections were in an acceptable condition. An inspection of core samples from the cracked sections clearly indicated the presence of top-down cracking. The cracks initiated from the surface and moved downward.

- The crack rating history for each test section was obtained from the flexible pavement condition survey database, which is maintained by the Florida Department of Transportation (FDOT).

The crack initiation time for each test section was determined on the basis of the above information and the best knowledge of the research team. It is shown in Table 6-7.

Table 6-7. Observed top-down cracking performance

Section No	Section Code	Observed Initiation-Time (year)
1	I75-1A	10
2	I75-1B	12
3	I75-3	11
4	I75-2	17
5	SR80-1	13
6	SR80-2	22
7	I10-8	8
8	I10-9	8
9	SR471	2
10	SR19	1
11	SR997	38
12	I94-4	4
13	I94-14	6

In phase two, predictions obtained using the calibrated model were presented for all test sections including those of Group II. For comparison purposes, the observed crack initiation time of Group II is also presented in Table 6-7, which was obtained from Minnesota Department of Transportation (MDOT). Based on the observed crack initiation time, pavement cracking performance can be categorized according to one of the following five performance levels:

- Level I: 1 to 5 years before crack initiation.
- Level II: 6 to 10 years before crack initiation.
- Level III: 11 to 20 years before crack initiation.
- Level IV: 21 to 30 years before crack initiation.
- Level V: greater than 30 years before crack initiation.

Calibration of Model

Model calibration was completed by matching as closely as possible top-down cracking predictions with observed top-down cracking in the field. The 11 pavement sections (Group I) documented in the prior section were used for calibration of the model. Since the aging parameter (k_1) was included as an unknown parameter within the fracture energy aging model, R^2 of the predicted initiation times of top-down cracking was determined for each assumed k_1 value using linear regression. A series of linear regressions was conducted with k_1 values ranging from 0.5 to 5. The final model was chosen as the k_1 value resulted in the best fit (highest R^2) between observed initiation times of cracking with the predicted ones.

Calibration Procedure

First, a matrix of runs of the top-down cracking performance model was conducted to obtain crack initiation time predictions for each selected section at 8 values of the aging parameter ranging between 0.5 and 5. This range of k_1 values was determined by a trial-and-error process. It was observed that a value of 0.5 resulted in higher levels of predicted performance i.e., longer time to crack initiation for most of the pavement sections, including those sections known to have poor observed performance. Similarly, a value of 5 resulted in lower levels of predicted performance for most of the sections, including those sections known to have good observed performance. The data obtained from these runs is shown in Table 6-8.

Table 6-8. Predicted versus observed cracking performance for different k_1-values (all test sections in Group I)

Section No.	Observed t_i (year)	Predicted t_i' (year) k_1-value 0.5	1	1.5	2	2.5	3	3.5	5
1	10	14.7	14.7	13.8	12.7	11.8	10.9	10.7	9.6
2	12	13.9	13.9	13.9	13.9	13.8	12.9	12.7	11.0
3	11	8.9	8.0	6.9	6.5	5.9	5.5	4.9	4.0
4	17	19.0	19.0	18.8	17.8	16.8	16.0	15.7	14.6
5	13	3.0	2.3	2.2	1.7	1.3	1.2	1.2	1.1
6	22	25.7	25.7	25.7	24.7	23.7	22.8	22.6	20.9
7	8	7.6	6.6	5.9	5.8	5.6	5.6	4.9	4.6
8	8	7.9	6.9	6.7	6.6	5.9	5.8	5.7	4.7
9	2	6.9	5.8	5.5	4.9	4.8	4.8	4.8	4.7
10	1	5.6	4.6	4.3	3.9	3.8	3.8	3.7	3.5
11	38	34.8	34.8	34.8	34.8	34.8	34.8	34.8	34.7
		R^2							
		0.807	0.803	0.802	0.809	0.802	0.801	0.791	0.767

Secondly, for each aging parameter, a linear regression routine was used to determine R^2 by regressing the observed initiation time on the predicted time of crack initiation. The optimum k_1 value was then chosen as the one resulting in the largest R^2. In other words, the value that resulted in the best match (lowest error) between predicted crack initiation time and the time observed in the field was chosen as the optimum k_1.

Initial Calibration Results

Linear regressions were performed to determine eight different values of R^2 (one for each aging parameter k_1), which are also presented in Table 6-8. As shown, eight models were obtained, each with its own k_1 and R^2. The model with the highest R^2 had the following parameters:

- $k_1 = 2.0$
- $R^2 = 0.809$

Another way to evaluate the goodness of fit of the model is to directly compare the predicted to the observed levels of cracking performance, as defined in the prior section. The results of this comparison using predicted initiation time determined with the aging parameter presented above are shown in Figure 6-2, which may be summarized as follows:

- Two of two level I sections were predicted to be level I sections.
- Two of three level II sections were predicted to be level II sections and only one level II section was predicted to be level III section.
- Of the four level III sections, two were predicted to be level III sections, one was predicted to be level II, and one was predicted to be level I.
- The level IV and V sections were predicted to be level IV and V, respectively.

		Observed Cracking Performance				
		I	II	III	IV	V
Predicted Cracking Performance	I	2		1		
	II		2	1		
	III		1	2		
	IV				1	
	V					1

Figure 6-2. Predicted versus observed cracking performance (All 11 sections)

When viewed in this manner, the correlation between predicted and observed cracking performance appeared fairly strong. As shown in Figure 6-2, only one prediction was off the diagonal by two cells. Of the other 10 predictions, 8 were on the diagonal (representing good

prediction), and 2 were just one cell off the diagonal (implying fairly good prediction). Thus, the correspondence between predicted and observed cracking performance in terms of crack initiation time was good for 10 out of 11 sections.

However, the off diagonal by two cells prediction for test section five apparently had a strong influence on R^2, which was not very sensitive to the k_1 value. In other words, the prediction for test section five may have overshadowed the sensitivity of the results. In view of this problem with test section five, it was excluded from the final calibration. However, it was included in the validation process as an independent data point.

Final Calibration

Because of the problem with test section five, it was not included in the final calibration of the model. Once again linear regressions were performed to determine eight different values of R^2 (one for each aging parameter) and the results are given in Table 6-9:

Table 6-9. Predicted versus observed cracking performance for different k_1-values (without test section 5 in Group I)

Section No.	Observed t_i (year)	Predicted t_i' (year) k_1-value 0.5	1	1.5	2	2.5	3	3.5	5
1	10	14.7	14.7	13.8	12.7	11.8	10.9	10.7	9.6
2	12	13.9	13.9	13.9	13.9	13.8	12.9	12.7	11.0
3	11	8.9	8.0	6.9	6.5	5.9	5.5	4.9	4.0
4	17	19.0	19.0	18.8	17.8	16.8	16.0	15.7	14.6
6	22	25.7	25.7	25.7	24.7	23.7	22.8	22.6	20.9
7	8	7.6	6.6	5.9	5.8	5.6	5.6	4.9	4.6
8	8	7.9	6.9	6.7	6.6	5.9	5.8	5.7	4.7
9	2	6.9	5.8	5.5	4.9	4.8	4.8	4.8	4.7
10	1	5.6	4.6	4.3	3.9	3.8	3.8	3.7	3.5
11	38	34.8	34.8	34.8	34.8	34.8	34.8	34.8	34.7
		R^2							
		0.902	0.911	0.914	0.930	0.931	0.933	0.924	0.901

It was determined that the model with the highest R^2 had the following parameters:

- $k_1 = 3.0$
- $R^2 = 0.933$

The above aging parameter was used to generate the comparison between predicted and observed performance presented in Figure 6-3. As shown in the figure, no prediction was off the diagonal by more than one cell. 8 out of the 10 predictions were on the diagonal (representing good prediction) and the other 2 were just one cell off the diagonal (implying fairly good prediction). Thus, the correspondence between predicted and observed performance in terms of crack initiation time was good for all 10 test sections.

In conclusion, results of the calibration effort clearly indicate that the top-down cracking performance model appears to adequately represent and account for the most significant factors that influence top-down cracking in the field.

		Observed Cracking Performance				
		I	II	III	IV	V
Predicted Cracking Performance	I	2				
	II		2	1		
	III		1	2		
	IV				1	
	V					1

Figure 6-3. Predicted versus observed cracking performance (without section 5)

Validation of Model

The previous section showed strong correlation between top-down cracking predictions by the performance model and observed crack initiation time in the field, thus establishing the model's credibility. The final step in the model-developing process was validation of the selected model. The objective was to assess the ability of the performance model to accurately predict top-down cracking in the field using data not used in developing the model.

For validating a regression model, three methods are commonly used including: 1) Collection of new data, 2) Data splitting, and 3) Prediction sum of squares (PRESS). The first method suggests that a new data set should be collected. However, the collection of new data is not possible due to time and resource constraints of this study. The second method is not feasible due to the small sample size of the available data set.

The last method is suitable for small data sets where data splitting is impractical. Since it has been successfully used by Lytton and Roque et al. (51) for validation of the thermal cracking model, the PRESS method was selected for use in this study.

PRESS Procedure

In the PRESS procedure, one data point is removed at a time from the data set (e.g., a data set with n data points) while the unknown parameters in the model are being estimated. In other words, the model is calibrated with (n-1) data points at a time. Then this model is used to predict the value of the removed point. This process is repeated for all the data points in the data set. The predicted values obtained by this method are then compared with the actual values. The R^2 (PRESS) is calculated for the predicted and actual values as follows:

$$\left(R^2\right)_p = 1 - \frac{\sum\left(Y_{(i)} - \hat{Y}_{(i)}\right)}{\sum\left(Y_{(i)} - \bar{Y}_{wo(i)}\right)} \tag{6-1}$$

where: $Y_{(i)}$ = observed response for the ith data point

$\hat{Y}_{(i)}$ = predicted response for the ith data point

$\overline{Y}_{wo(i)}$ = average of the predicted responses of (n-1) data points without the ith data point

The R^2 (PRESS) will always be lower than the R^2 obtained from the full model because the PRESS procedure uses (n-1) data points to estimate the unknown parameters as compared to the procedure based on the full model where n data points are used. The degree of closeness of R^2 (PRESS) to R^2 (Full model) serves as a measure of the model's predictive ability. Good models will have an R^2 from the PRESS procedure close to the R^2 from the full model.

Validation Process Using PRESS

For validation purposes, the performance model used to predict crack initiation for any one particular test section was calibrated on the basis of data of the other test sections. For example, the model used to predict crack initiation in test section one was calibrated using the data set without including section one.

In this study, the validation process involved two steps. First, as was the case with final calibration of the performance model presented in the prior section, test section five was not included. So, only 10 test sections were included in this step. The calibration procedure (also described in the prior section) was conducted 10 times, once for each test section. The R^2 (PRESS) was then computed using Eqn (6-1).

Next, the crack initiation time of test section five was predicted using the model calibrated with the 10 test sections of step one. The error associated with this prediction was also added to the R^2 (PRESS) obtained in the first step.

As an example of step one, the top-down cracking performance model used to predict crack initiation for test section one, was calibrated with data from the other 9 test sections, i.e., test sections two through eleven except for test section five. Linear regressions were performed

to determine 8 different values of R^2 (one for each aging parameter) on the basis of the data from the other 9 test sections. The performance model used to predict crack initiation for test section one was selected as the one having the k_1 value that resulted in the highest R^2. This process was repeated 10 times such that a total of 80 linear regressions were performed during step one. A similar process was used in step two, where linear regressions were performed to determine 8 different values of R^2 on the basis of the data from the 10 test sections of step one. The top-down cracking performance model used to predict crack initiation for test section five was selected as the one that resulted in the highest R^2. This process was applied once in step two.

The R^2 for each linear regression is presented in Table 6-10. For each pavement section, the model resulting in the largest R^2 is identified via a shaded area, in which the predicted cracking performance level is also presented.

The resulting 11 models were used to make an independent prediction of crack initiation time of top-down cracking for each test section in the validation effort. The independent predictions were compared to observed initiation time to evaluate the predictive capability of the model. Results of this evaluation are presented in the following sub-section.

Table 6-10. Predicted cracking performance for various aging parameters using PRESS procedure

Section No.	Observed Performance*	Predicted Performance*							
		Aging Parameter k_1							
		0.5 (R^2)	1.0 (R^2)	1.5 (R^2)	2.0 (R^2)	2.5 (R^2)	3.0 (R^2)	3.5 (R^2)	5.0 (R^2)
1	II	(0.923)	(0.932)	(0.927)	III (0.937)	(0.934)	(0.933)	(0.924)	(0.900)
2	III	(0.906)	(0.915)	(0.917)	(0.934)	III (0.934)	(0.934)	(0.924)	(0.902)
3	III	(0.906)	(0.920)	(0.929)	(0.949)	(0.956)	II (0.962)	(0.959)	(0.948)
4	III	(0.904)	(0.913)	(0.916)	(0.930)	(0.930)	III (0.933)	(0.924)	(0.905)
5	III	(0.902)	(0.911)	(0.914)	(0.930)	(0.931)	I (0.933)	(0.924)	(0.901)
6	IV	(0.907)	(0.917)	(0.920)	IV (0.931)	(0.928)	(0.927)	(0.917)	(0.893)
7	II	(0.900)	(0.911)	(0.916)	(0.934)	(0.935)	II (0.937)	(0.931)	(0.910)
8	II	(0.900)	(0.910)	(0.913)	(0.931)	(0.934)	II (0.936)	(0.927)	(0.909)
9	I	(0.914)	(0.914)	(0.915)	(0.930)	(0.930)	I (0.932)	(0.921)	(0.895)
10	I	(0.909)	(0.911)	(0.911)	(0.928)	(0.928)	I (0.930)	(0.919)	(0.891)
11	V	(0.736)	(0.763)	(0.771)	(0.821)	(0.824)	V (0.829)	(0.802)	(0.734)

* Predicted and Observed Performance are shown as Levels I to V.

Validation Results

The R^2 from the PRESS procedure described above was determined to be 0.82. In comparison to the R^2 of 0.93 for the full model (i.e., the model determined from the final calibration), the performance model developed appears to have strong predictive ability.

The data were also evaluated by directly comparing the independent performance predictions with the observed levels of performance defined in Section 6.1. The results of the

comparison are presented in Figure 6-4. As shown, only one prediction was off the diagonal by two cells. Of the other 10 predictions, 8 were on the diagonal, and 2 were just one cell off the diagonal. Thus, the correspondence between predicted and observed cracking performance for these independent predictions was good for 10 of 11 test sections.

		Observed Cracking Performance				
		I	II	III	IV	V
Predicted Cracking Performance	I	2		1		
	II		2	1		
	III		1	2		
	IV				1	
	V					1

Figure 6-4. Predicted versus observed cracking performance (from PRESS)

Based on these results and the R^2 (PRESS) of 0.82, the predictive capability of the model appears to be good. After model calibration and validation, the final predictions using the calibrated model are presented in the next section.

Final Model Predictions

In this section, final model predictions were conducted using the calibrated model. The complete results are presented in Table 6-11, which will be illustrated in three parts. First, the predicted crack initiation time is compared with the observed initiation time in the field for all

thirteen test sections. Second, the predicted propagation time is compared with the predicted initiation time. The purpose is to evaluate the predicted propagation time by assessing its relationship with the initiation time. Thirdly, the cracking histories of all sections in terms of crack amount versus time are presented, which were obtained using the crack amount model.

Table 6-11. Crack Depths versus Time Predictions Using Calibrated Aging Parameter (k_1 = 3.0)

Section		I75-1A		I75-1B		I75-3		I75-2		SR80-1		SR80-2	
Thickness (inch)		6.54		6.23		6.47		7.42		3.38		6.29	
Year Opened		1988		1989		1988		1989		1987		1984	
Observed Initiation Time (year)		10		12		11		17		13		22	
Predictions	C.D.*	C/D +	Y.C.@	C/D	Y.C.	C/D	Y.C.	C/D	Y.C.	C/D	Y.C.	C/D	Y.C.
	0.25	0.04	10.9	0.04	12.9	0.04	5.5	0.03	16.0	0.07	1.2	0.04	22.8
	0.50	0.08	12.7	0.08	14.6	0.08	6.3	0.07	18.4	0.15	1.7	0.08	25.6
	0.75	0.11	13.2	0.12	15.1	0.12	6.8	0.10	18.9	0.22	1.9	0.12	26.5
	1.00	0.15	13.5	0.16	15.4	0.15	6.9	0.13	19.3	0.30	2.0	0.16	26.9
	1.25	0.19	13.7	0.20	15.7	0.19	6.9	0.17	19.6	0.37	2.1	0.20	27.4
	1.50	0.23	13.9	0.24	15.9	0.23	7.0	0.20	19.8	0.44	2.1	0.24	27.7
	1.75	0.27	14.1	0.28	16.0	0.27	7.0	0.24	20.0	0.52	2.4	0.28	27.9
	2.00	0.31	14.2	0.32	16.2	0.31	7.1	0.27	20.1			0.32	28.3
	2.25	0.34	14.3	0.36	16.3	0.35	7.1	0.30	20.3			0.36	28.5
	2.50	0.38	14.5	0.40	16.4	0.39	7.2	0.34	20.4			0.40	28.6
	2.75	0.42	14.7	0.44	16.7	0.43	7.2	0.37	20.6			0.44	28.8
	3.00	0.46	14.8	0.48	17.0	0.46	7.3	0.40	20.7			0.48	29.2
	3.25	0.50	15.1	0.52	17.2	0.50	7.5	0.44	20.8			0.52	29.4
	3.50							0.47	20.9				
	3.75							0.51	21.1				

* C.D. stands for Crack Depth (inch); + C/D stands for Crack depth over AC thickness ratio; @ Y.C. stands for time (year)

Table 6-11. Continued

Section		I10-8		I10-9		SR471		SR19		SR997		I94-4		I94-14	
Thickness (inch)		7.20		7.40		2.58		2.39		2.17		9.10		10.90	
Year Opened		1996		1996		2000		2000		1963		1994		1994	
Observed Initiation Time (year)		8		8		2		1		38		4		6	
Predictions	C.D.*	C/D +	Y.C.@	C/D	Y.C.	C/D	Y.C.	C/D	Y.C.	C/D	Y.C.	C/D	Y.C.	C/D	Y.C.
	0.25	0.03	5.6	0.03	5.8	0.10	4.8	0.10	3.8	0.12	34.8	0.03	4.2	0.02	6.0
	0.50	0.07	6.6	0.07	6.9	0.19	5.2	0.21	4.7	0.23	39.6	0.05	5.9	0.05	7.2
	0.75	0.10	6.8	0.10	7.3	0.29	5.7	0.31	4.9	0.35	41.4	0.08	6.0	0.07	7.4
	1.00	0.14	7.0	0.14	7.5	0.39	6.0	0.42	5.0	0.46	42.8	0.11	6.2	0.09	7.9
	1.25	0.17	7.1	0.17	7.6	0.48	6.3	0.52	5.1	0.58	43.2	0.14	6.3	0.11	8.0
	1.50	0.21	7.3	0.20	7.7	0.58	7.0					0.16	6.9	0.14	8.3
	1.75	0.24	7.4	0.24	7.8							0.19	7.1	0.16	8.8
	2.00	0.28	7.5	0.27	7.9							0.22	7.2	0.18	9.0
	2.25	0.31	7.5	0.30	8.0							0.25	7.7	0.21	9.2
	2.50	0.35	7.6	0.34	8.1									0.23	9.3
	2.75	0.38	7.7	0.37	8.2									0.25	9.9
	3.00	0.42	7.7	0.41	8.3										
	3.25	0.45	7.7	0.44	8.4										
	3.50	0.49	7.8	0.47	8.5										
	3.75	0.52	7.9	0.51	8.5										

* C.D. stands for Crack Depth (inch); + C/D stands for Crack depth over AC thickness ratio; @ Y.C. stands for time (year)

Predicted vs. Observed Crack Initiation Time

The predicted crack initiation time versus the observed time in the field for all thirteen test sections are presented in Figure 6-5. As shown, the predictions generally agreed well with the observed time except for SR80-1 (i.e., test section five).

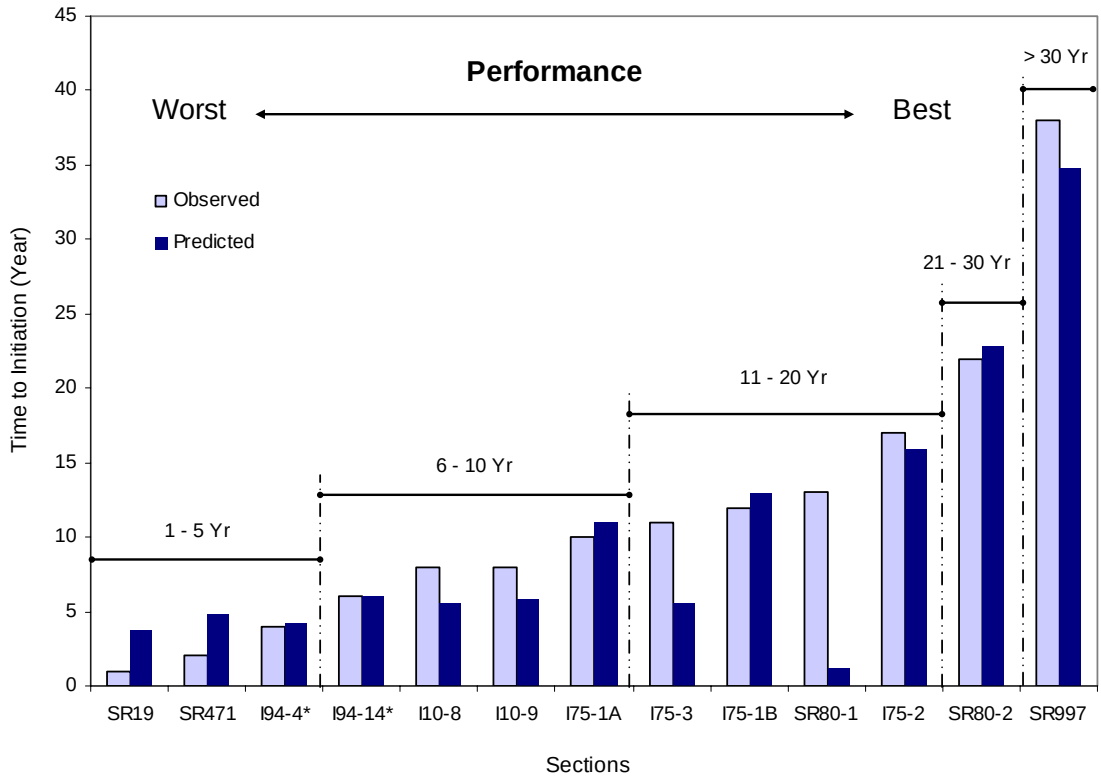

Figure 6-5. Predicted versus observed crack initiation time for all test sections

Crack Initiation Time vs. Propagation Time

The initial crack depth of top-down cracking was determined to be 6 mm (0.25 in), and the critical crack depth was defined as the depth equal to one-half of the AC layer thickness (see Chapter 3, Section Four). Therefore, for a vertical crack, the crack propagation time t_p can be obtained by computing the difference between the time to initial crack depth (i.e., crack initiation time) and that to critical crack depth.

The crack propagation time was thus determined for each of the test sections using predictions by the calibrated model and plotted against the corresponding crack initiation time in Figure 6-6. As shown, the predicted propagation time appears to increase linearly with the initiation time: 1) For pavement sections that start to crack after in service for 10 to 20 years, the propagation time to failure is about 4 to 5 years, which is consistent with our typical observations in the field. 2) For test sections with an earlier crack initiation, the propagation time tends to be shorter. 3) For pavements that can last for more than 20 years, the predicted time to critical crack depth is also longer.

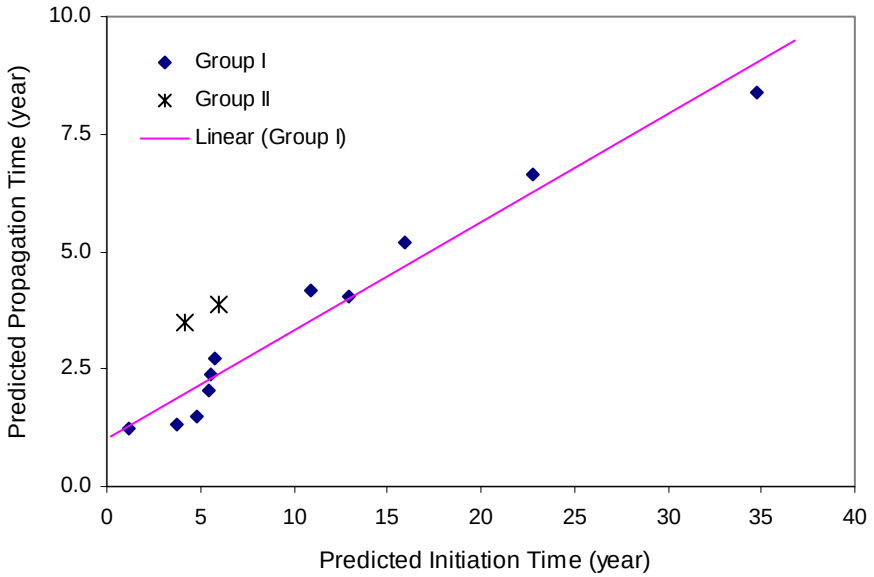

Figure 6-6. Predicted crack propagation time versus crack initiation time

Due to difficulties involved in obtaining reliable data on development of a real crack in the field, no further calibration was performed on predicted crack propagation time. However, the comparison in Figure 6-6 can be viewed as an alternative means to assess the reasonableness of the model for propagation time prediction.

Crack Amount Development with Time

The final model predictions are expressed in terms of crack amount versus time for each of the test sections. They are presented according to the performance category (I to V) with respect to observed performance, as shown in Figures 6-7 to 6-10. These predictions may be summarized as follows:

- The amount of cracking of a thin pavement at initiation is greater than that of a thicker pavement. This indicates that crack initiation may be more easily identified in thinner pavements than in thicker ones in the field.

- For test sections of Group I (governed by the bending mechanism): 1) Predictions for sections of lower performance levels are generally consistent with field observations (Figures 6-7 and 6-8). The relatively high creep rate combined with high surface tensile stresses are believed to be responsible for severe cracking conditions in these sections within a relatively short period. 2) Predictions for sections of higher performance levels also agree reasonably with observations in the field, except for section five (i.e., SR80-1) (Figures 6-9 and 6-10). The relatively low creep rate and high fracture energy of the asphalt mixtures combined with the relatively low traffic loads in these sections resulted in longer service life.

- For test sections of Group II (governed by the near-tire mechanism): Predictions of crack initiation for both sections of this group agree well with field observations. However, the trend for crack propagation appears to be different from those predicted for sections of Group I (Figures 6-7 and 6-8). This is expected because a crack growth simulation tool specifically for the near-tire mechanism is not available. The CGS module (focused on the bending mechanism) was used as a surrogate to make these predictions. Therefore, an enhanced crack growth model that also addresses the near-tire mechanism needs to be developed for more accurate prediction of top-down cracking in thick HMA layers.

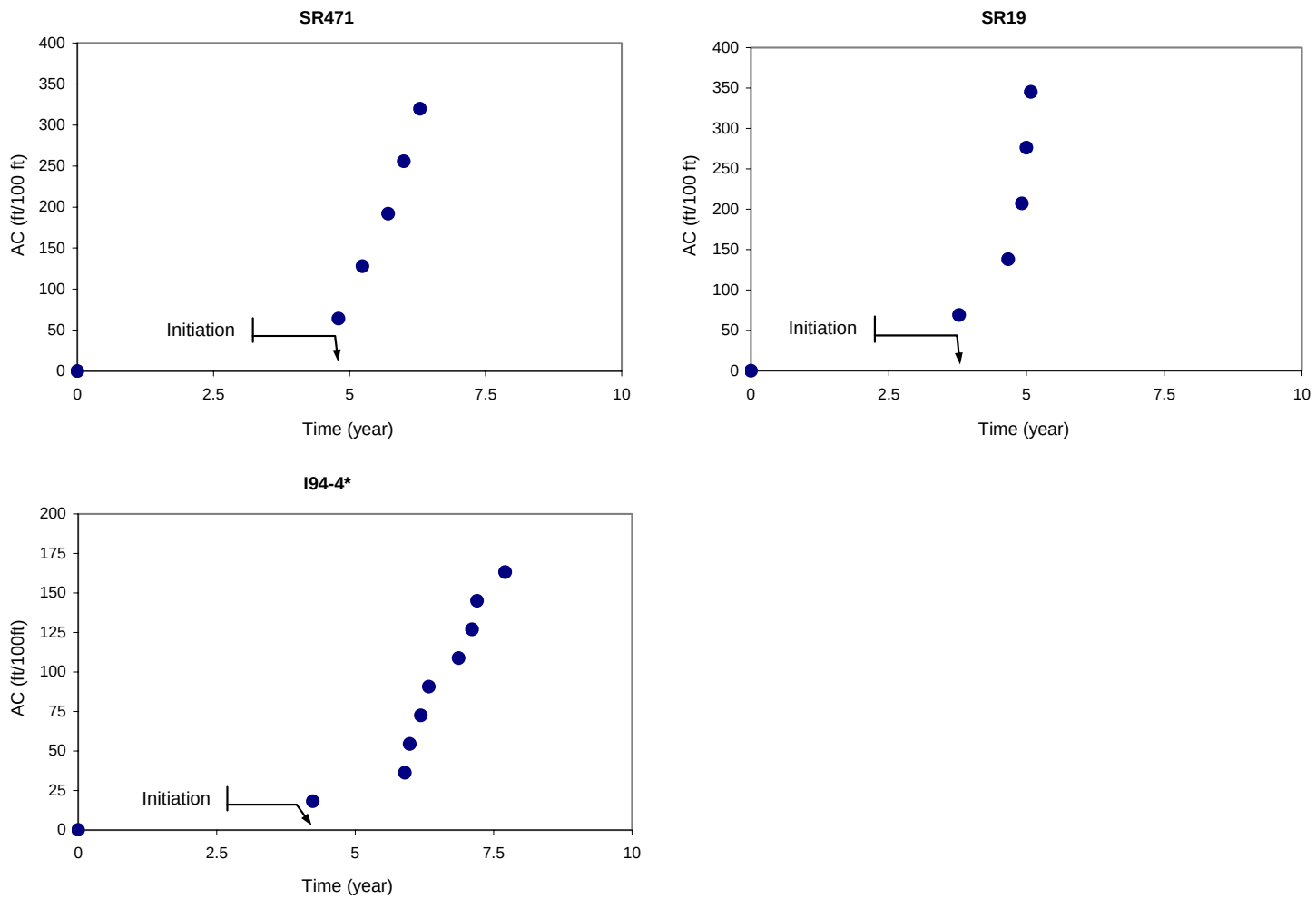

Figure 6-7. Predicted crack amount versus time for test sections of level I

(∗ The maximum amount of cracking was reduced to 165 ft /100 ft for full depth pavement (near-tire mechanism).)

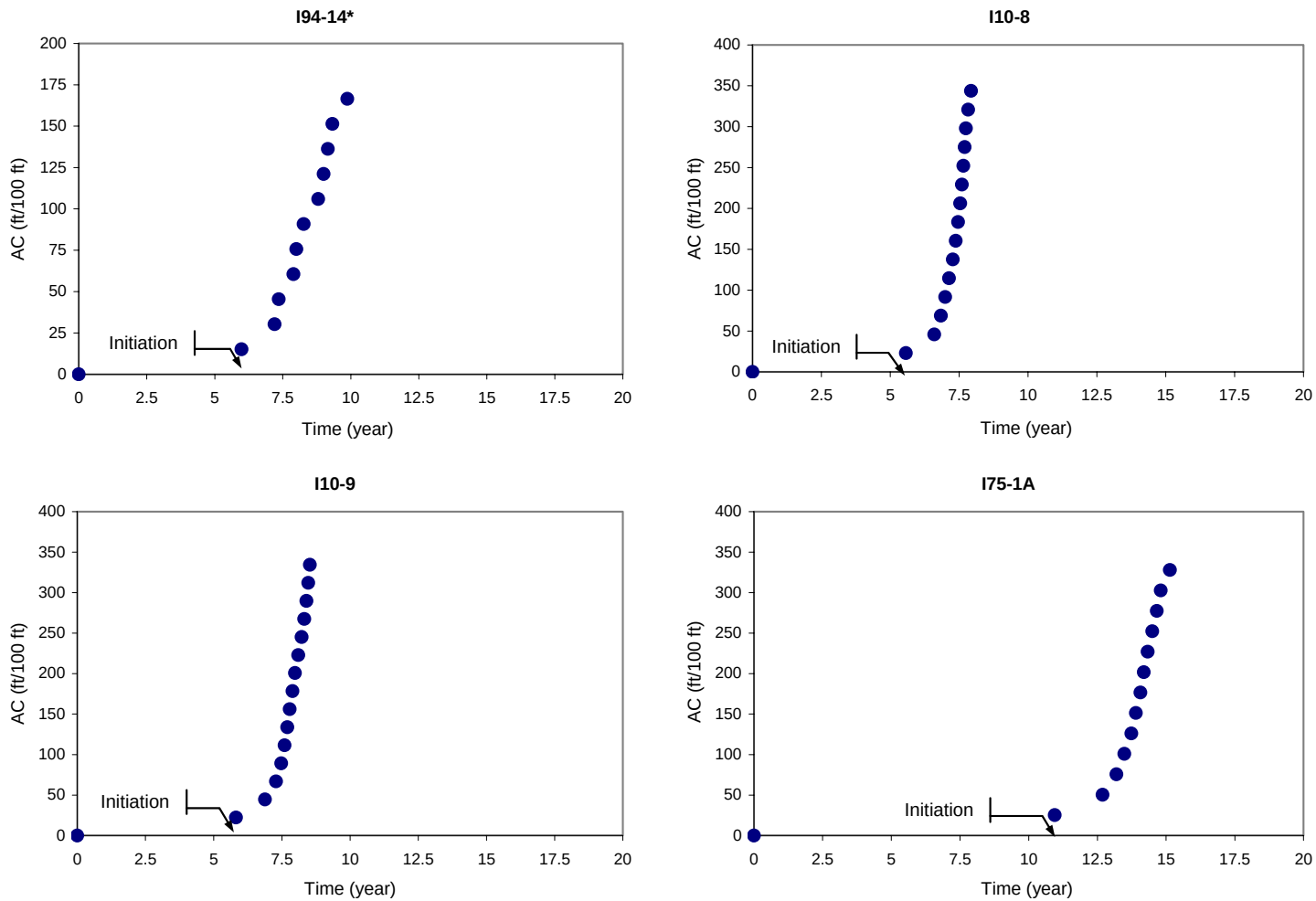

Figure 6-8. Predicted crack amount versus time for test sections of level II

(∗ The maximum amount of cracking was reduced to 165 ft /100 ft for full depth pavement (near-tire mechanism).)

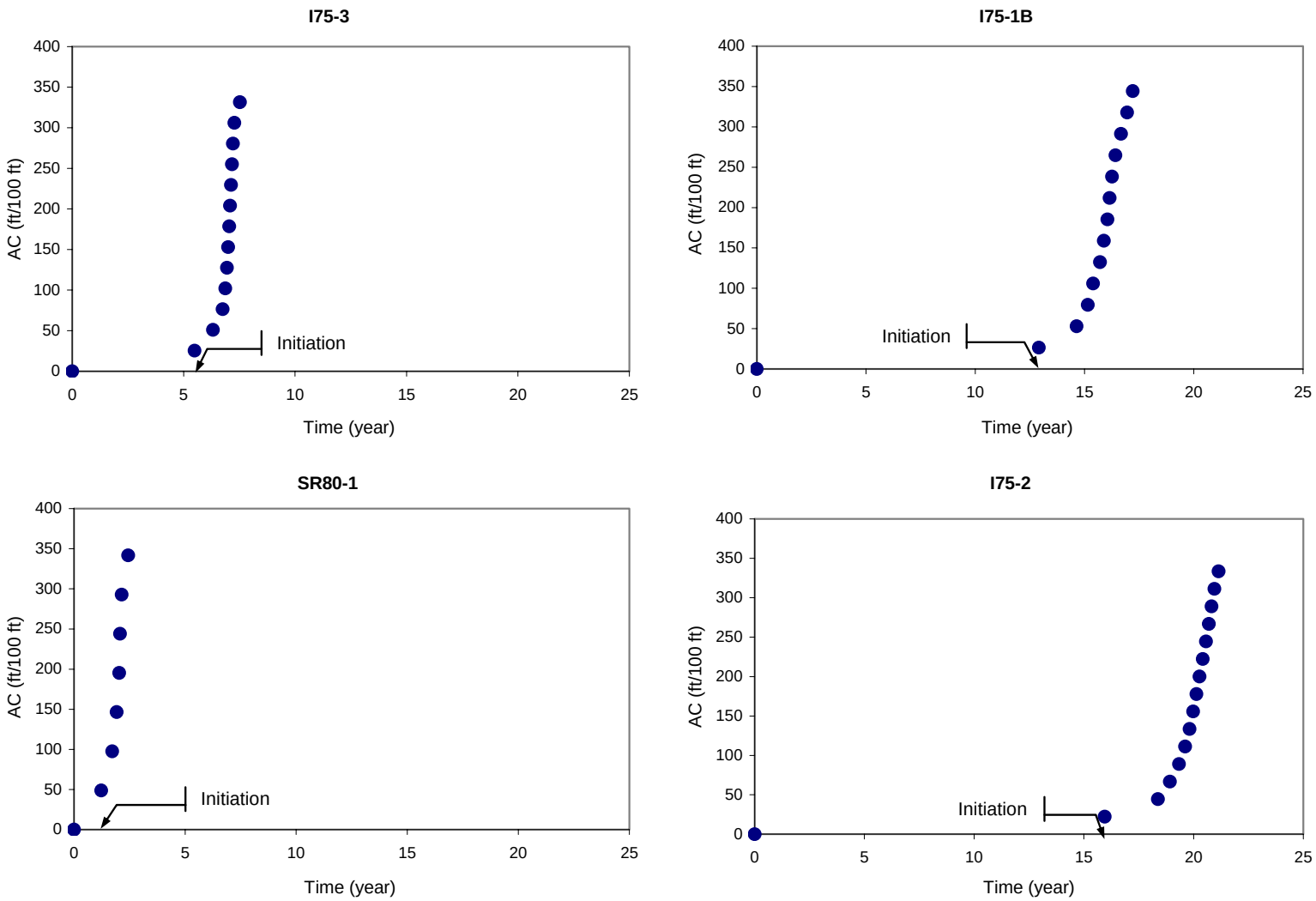

Figure 6-9. Predicted crack amount versus time for test sections of level III

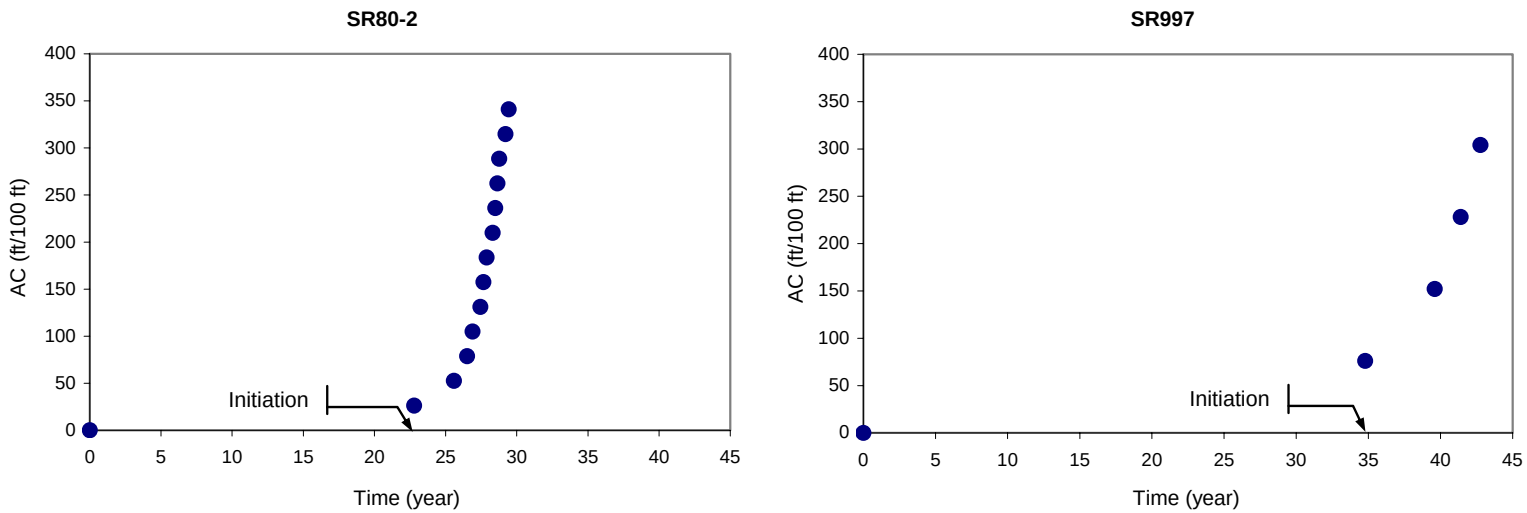

Figure 6-10. Predicted crack amount versus time for test sections of levels IV and V

CHAPTER 7
CONCLUSIONS AND RECOMMENDATIONS

Conclusions

An HMA-FM-based model was developed to predict top-down cracking performance, with the emphasis placed on the bending mechanism. This model was comprised of several key elements as summarized below:

- A critical condition concept that can more accurately capture field observations and significantly reduces the computation time required for long-term pavement performance prediction.
- Material property sub-models that account for changes in near-surface mixture properties with aging, including increase in stiffness (stiffening), reduction in fracture energy (embrittlement), and reduction in healing potential, which make pavements more susceptible to top-down cracking.
- A thermal response model that predicts transverse thermal stresses that can be an important part of the top-down cracking mechanism.
- A pavement fracture model that predicts crack growth with time, accounting for the effect of changes in geometry on stress distributions.

A systematic parametric study showed that the system provided reasonable predictions and expected trends for both crack initiation and propagation. Furthermore, a full calibration of field sections was completed by matching as closely as possible top-down cracking predictions in terms of crack initiation time with observed top-down cracking in the field. Only one calibration factor (i.e., the aging parameter k_1) was included in the calibration process. Results of the calibration effort indicated that the predictive system adequately represents and accounts for the most significant factors that influence top-down cracking in the field. The validation efforts using the prediction sum of squares (PRESS) procedure further established the viability of the predictive system.

In conclusion, the work performed clearly indicates that the HMA-FM-based model developed and evaluated in this study can form the basis for a top-down cracking model suitable

for use in the MEPDG. It should also be noted that material property sub-models developed for the model should be considered place-holder relations. Further development and evaluation of the material property place-holder relationships are highly recommended in future work, particularly for models to predict fracture energy (FE), damage rate, healing potential, and their changes with aging.

Recommendations

The following items are recommended for future research:

- Damage rate and fracture energy are the most important material properties related to top-down cracking. However, no reliable material model is available for either of them. The place-holder relations introduced in this study to predict damage rate were based on the Witczak model, but should not be considered reliable without further validation. Enhanced relations may need to be developed. Regarding the determination of fracture energy, an initial FE model from mixture characteristics (gradation etc.) and properties of mixture components needs to be developed.

- A simplified empirical-based healing model was used in this research, but should not be considered reliable without further validation. An enhanced model may need to be developed for more accurate estimation of mixture healing under various conditions.

- The near-tire mechanism needs to be further investigated for more proper incorporation into the performance model. Considerations are required regarding effects of tire type and cross slope on shear-induced tension at tire edge.

- Wander effects relative to mechanisms need to be addressed. For example, the significance of the near-tire mechanism is strongly dependent on the extent of wander, because the location for crack initiation is right next to the tire edge. However, the importance of the bending-mechanism is not sensitive to wander.

- Damage effects on reduction in AC modulus and the change in stress-strain-energy response resulting from the modulus reduction need to be considered and integrated into the performance model.

- Influence of stress state on damage rate needs to be considered for more accurate determination of critical condition.

LIST OF REFERENCES

1. Roque, R., and B. E. Ruth. Mechanisms and Modeling of Surface Cracking in Asphalt Pavements. *Journal of the Association of Asphalt Paving Technologists*, Vol. 59, 1990, pp. 397-421.

2. Myers, L., R. Roque, and B. E. Ruth. Mechanisms of Surface Initiated Longitudinal Wheel Path Cracks in High-type Bituminous Pavements. *Journal of the Association of Asphalt Paving Technologists*, Vol. 67, 1998, pp. 402-432.

3. Uhlmeyer, J. S., K. Willoughby, L. M. Pierce, and J. P. Mahoney. Top-down Cracking in Washington State Asphalt Concrete Wearing Courses. In *Transportation Research Record: Journal of the Transportation Research Board, No. 1730*, Transportation Research Board of the National Academies, Washington, D.C., 2000, pp. 110-116.

4. Gerritsen, A. H., C. A. P. M. Van Gurp, J. P. J. Van Der Heide, A. A. A. Molenaar, and A. C. Pronk. Prediction and Prevention of Surface Cracking in Asphaltic Pavements. *Proc., 6th International Conference on Structural Design of Asphalt Pavements*, Ann Arbor, Michigan, 1987, pp. 378-391.

5. De Freitas, E. F., P. Pereira, L. Picado-Santos, and A. T. Papagiannakis. Effect of Construction Quality, Temperature and Rutting on Initiation of Top-downing Cracking. In *Transportation Research Record: Journal of the Transportation Research Board, No. 1929*, Transportation Research Board of the National Academies, Washington, D.C., 2005, pp. 174-182.

6. Matsuno, S., and T. Nishizawa. Mechanism of Longitudinal Surface Cracking in Asphalt Pavement. *Proc., 7th International Conference on Asphalt Pavements*. University of Nottingham, UK, Vol. 2, 1992, pp. 277-291.

7. Raju, S., S. S. Kumar, K. S. Reddy, S. Bose, and B. B. Pandey. Analysis of Top-Down Cracking Behavior of Asphalt Pavements. *Transportation Research Board*, Washington, D.C., 2008.

8. Myers, L. A., and R. Roque. Top-down Crack Propagation in Bituminous Pavements and Implications for Pavement Management. *Journal of the Association of Asphalt Paving Technologists*, Vol. 71, 2002, pp. 651-670.

9. Zhang, Z., R. Roque, and B. Birgisson. Evaluation of Laboratory-Measured Crack Growth Rate for Asphalt Mixtures. In *Transportation Research Record: Journal of the Transportation Research Board, No. 1767*, Transportation Research Board of the National Academies, Washington, D.C., 2001, pp. 67-75.

10. Kim, B., R. Roque, and B. Birgisson. Effect of Styrene Butadiene Styrene Modifier on Cracking Resistance of Asphalt Mixture. In *Transportation Research Record: Journal of the*

Transportation Research Board, No. 1829, Transportation Research Board of the National Academies, Washington, D.C., 2003, pp. 8-15.

11. Roque, R., Z. Zhang, and B. Sankar. Determination of Crack Growth Rate Parameters of Asphalt Mixtures Using the SuperPave Indirect Tensile Test (IDT). *Journal of the Association of Asphalt Paving Technologists*, Vol. 68, 1999, pp. 404-433.

12. Yoo, P. J., and I. L. Al-Qadi. The Truth and Myth of Fatigue Cracking Potential in Hot-Mix Asphalt: Numerical Analysis and Validation. *Journal of the Association of Asphalt Paving Technologists*, Vol. 77, 2008, pp. 549-590.

13. Huang, Y. H. *Pavement Analysis and Design*. New Jersey, Prentice Hall, Inc., 2004, pp. 104.

14. Kim, Y. R., D. N. Little. One-Dimensional Constitutive Modeling of Asphalt Concrete. *ASCE Journal of Engineering Mechanics*, Vol. 116, No. 4, pp. 751-772, 1990.

15. Schapery, R. A. Correspondence Principles and a Generalized J Integral for Large Deformation and Fracture Analysis of Viscoelastic Media. *International Journal of Fracture*, Vol. 25, 1984, pp. 195-223.

16. Park, S. W., Y. R. Kim, and R. A. Schapery. A Viscoelastic Continuum Damage Model and Its Application to Uniaxial Behavior of Asphalt Concrete. *Mechanics of Materials*, Vol. 24, No. 4, pp. 241-255, 1996.

17. Kim, Y. R., Y. C. Lee, and H. J. Lee. Correspondence Principle for Characterization of Asphalt Concrete. *ASCE Journal of Materials in Civil Engineering*, Vol. 7, No. 1, 1995, pp. 59-68.

18. Kim, Y. R., H. J. Lee, and D. N. Little. Fatigue Characterization of Asphalt Concrete Using Viscoelasticity and Continuum Damage Theory. *Journal of the Association of Asphalt Paving Technologists*, Vol. 66, 1997, pp. 520-569.

19. Lee, H. J., and Y. R. Kim. Viscoelastic Constitutive Model for Asphalt Concrete under Cyclic Loading. *Journal of Engineering Mechanics*, Vol. 124, No. 1, 1998, pp. 32-40.

20. Lee, H. J., and Y. R. Kim. A Viscoelastic Continuum Damage Model of Asphalt Concrete with Healing. *ASCE Journal of Engineering Mechanics*, Vol. 124, No. 11, 1998, pp. 1224-1232.

21. Daniel, J. S., Y. R., Kim, and H. J. Lee. Effects of Aging on Viscoelastic Properties of Asphalt-Aggregate Mixtures. In *Transportation Research Record: Journal of the Transportation Research Board, No. 1630*, Transportation Research Board of the National Academies, Washington, D.C., 1998, pp. 21-27.

22. Schapery, R. A. Nonlinear Viscoelastic and Viscoplastic Constitutive Equations with Growing Damage. *International Journal of Fracture*, Vol. 97, 1999, pp. 33-66.

23. Chehab, G. R., Y. R. Kim, R. A. Schapery, M. Witczack, and R. Bonaquist. Time-Temperature Superposition Principle for Asphalt Concrete Mixtures with Growing Damage in Tension State. *Journal of the Association of Asphalt Paving Technologists*, Vol. 71, 2002, pp. 559-593.

24. Chehab, G. R., Y. R. Kim, R. A. Schapery, M. Witczack, and R. Bonaquist. Characterization of Asphalt Concrete in Uniaxial Tension Using a Viscoelastoplastic Model. *Journal of the Association of Asphalt Paving Technologists*, Vol. 72, 2003, pp. 315-355.

25. Daniel, J. S., and Y. R. Kim. Development of Simplified Fatigue Test and Analysis Procedure Using a Viscoelastic Continuum Damage Model. *Journal of the Association of Asphalt Paving Technologists*, Vol. 71, 2002, pp. 619-650.

26. Zhang, Z., R. Roque, B. Birgisson, and B. Sangpetngam. Identification and Verification of a Suitable Crack Growth Law. *Journal of the Association of Asphalt Paving Technologists*, Vol. 70, 2001, pp. 206-241.

27. Roque, R., B. Birgisson, B. Sangpetngam, and Z. Zhang. Hot Mix Asphalt Fracture Mechanics: A Fundamental Crack Growth Law for Asphalt mixtures. *Journal of the Association of Asphalt Paving Technologists*, Vol. 71, 2002, pp. 816-827.

28. Sangpetngam, B., B. Birgisson, and R. Roque. Development of Efficient Crack Growth Simulator Based on Hot-mix Asphalt Fracture Mechanics. In *Transportation Research Record: Journal of the Transportation Research Board, No. 1832*, Transportation Research Board of the National Academies, Washington, D.C., 2003, pp. 105-112.

29. Sangpetngam, B., B. Birgisson, and R. Roque. Multilayer Boundary-element Method for Evaluating Top-down Cracking in Hot-mix Asphalt Pavements. In *Transportation Research Record: Journal of the Transportation Research Board, No. 1896*, Transportation Research Board of the National Academies, Washington, D.C., 2004, pp. 129-137.

30. Roque, R., B. Birgisson, C. Drakos, and B. Dietrich. Development and Field Evaluation of Energy-Based Criteria for Top-down Cracking Performance of Hot Mix Asphalt. *Journal of the Association of Asphalt Paving Technologists*, Vol. 73, 2004, pp. 229-260.

31. Kim, J., R. Roque, and B. Birgisson. Integration of Thermal Fracture in the HMA Fracture Model. *Journal of the Association of Asphalt Paving Technologists*, Vol. 77, 2008, pp. 631-662.

32. Mirza, M. W., and M. W. Witczak. Development of a Global Aging System for Short and Long Term Aging of Asphalt Cements. *Journal of the Association of Asphalt Paving Technologists*, Vol. 64, 1995, pp. 393-430.

33. ARA, Inc., *Guide for Mechanistic-Empirical Design of New and Rehabilitated Pavement Structures*. Final Report - NCHRP Project 1-37A. National Cooperative Highway Research Program, Transportation Research Board, Washington, D.C., 2004.

34. Witczak, M. W., and O. A. Fonseca. Revised Predictive Model for Dynamic (Complex) Modulus of Asphalt Mixtures. In *Transportation Research Record: Journal of the Transportation Research Board, No. 1540*, Transportation Research Board of the National Academies, Washington, D.C., 1996, pp. 15-23.

35. Deme, I. J., and F. D., Young. Ste. Anne Test Road Revisited Twenty Years Later. *Proceedings, Canadian Technical Asphalt Association*, Vol. 32, 1987, pp. 254-283.

36. Button, J. W., D. N. Little, Y. Kim, and J. Ahmed. Mechanistic Evaluation of Selected Asphalt Additives. *Journal of the Association of Asphalt Paving Technologists*, Vol. 56, 1987, pp. 62-90.

37. Zhang, Z. *Identification of Crack Growth Law for Asphalt Mixtures Using the Superpave Indirect Tensile Test (IDT)*. PhD Dissertation. University of Florida, Gainesville, 2000.

38. Daniel, J. S., and Y. R. Kim. Laboratory Evaluation of Fatigue Damage and Healing of Asphalt Mixtures. *ASCE Journal of Materials in Civil Engineering*, Vol. 13, No. 6, 2001, pp. 434-440.

39. Kim, B., and R. Roque. Evaluation of Healing Property of Asphalt Mixture. In *Transportation Research Record: Journal of the Transportation Research Board, No. 1970*, Transportation Research Board of the National Academies, Washington, D.C., 2006, pp. 84-91.

40. Si, Z., D. N. Little, and R. L. Lytton. Characterization of Microdamage and Healing of Asphalt Concrete Mixture. *ASCE Journal of Materials in Civil Engineering*, Vol. 14, No.6, 2002, pp. 461-470.

41. Kim, Y. R., D. N. Little, and R. L. Lytton. Fatigue and Healing Characterization of Asphalt Mixtures. *ASCE Journal of Materials in Civil Engineering*, Vol. 15, No.1, 2003, pp. 75-83.

42. Buttlar, W. G., R. Roque, and B. Reid. Automated Procedure for Generation of Creep Compliance Master Curve for Asphalt Mixtures. In *Transportation Research Record: Journal of the Transportation Research Board, No. 1630*, Transportation Research Board of the National Academies, Washington, D.C., 1998, pp. 28-36.

43. Hiltunen, D. R., and R. Roque. A Mechanics-Based Prediction Model for Thermal Cracking of Asphaltic Concrete Pavements. *Journal of the Association of Asphalt Paving Technologists*, Vol. 63, 1994, pp. 81-117.

44. Park, S. W., and Y. R. Kim. Interconversion between Relaxation Modulus and Creep Compliance for Viscoelastic Solids. *ASCE Journal of Materials in Civil Engineering*, Vol. 11, No. 1, 1999, pp. 76-82.

45. Park, S. W., and Y. R. Kim. Fitting Prony-series Viscoelastic Models with Power-law Presmoothing. *ASCE Journal of Materials in Civil Engineering*, Vol. 13, No. 1, 2001, pp. 26-32.

46. Sangpetngam, B. *Development and Evaluation of a Viscoelastic Boundary Element Method to Predict Asphalt Pavement Cracking*. PhD Dissertation. University of Florida, Gainesville, 2003.

47. Myers, L. A., R. Roque, and B. Birgisson. Use of Two-dimensional Finite Element Analysis to Represent Bending Response of Asphalt Pavement Structures. *International Journal of Pavement Engineering*, Vol. 2, 2001, pp. 201-214.

48. Roque, R., A. Guarin, G. Wang, J. Zou, and H. Mork. *Develop Methodologies/Protocols to Assess Cracking Potential of Asphalt Mixtures Using Accelerated Pavement Testing*. Final Report, FDOT-BD545-49, University of Florida, Gainesville, 2007.

49. Roque, R., and W. G. Buttlar. The Development of a Measurement and Analysis System to Accurately Determine Asphalt Concrete Properties Using the Indirect Tensile Mode. *Journal of the Association of Asphalt Paving Technologists*, Vol. 61, 1992, pp. 304-332.

50. Buttlar, W. G., and R. Roque. Development and Evaluation of the Strategic Highway Research Program Measurement and Analysis System for Indirect Tensile Testing at Low Temperatures. In *Transportation Research Record: Journal of the Transportation Research Board, No. 1454*, Transportation Research Board of the National Academies, Washington, D.C., 1994, pp. 163-171.

51. Lytton, R. L., J. Uzan, E. G. Fernando, R. Roque, D. Hiltunen, and S. M. Stoffels. *Development and Validation of Performance Prediction Models and Specifications for Asphalt Binders and Paving Mixes*. SHRP-A-357, Strategic Highway Research Program, National Research Council, Washington, D.C., 1993.

BIOGRAPHICAL SKETCH

Jian Zou was born in Haimen, Jiangsu Province, People's Republic of China, on November 12, 1975. He received a Bachelor of Science degree in civil engineering from Hohai University in 1998, and then worked as a research assistant at the same University.

In August 2001, Jian started a Master of Engineering program in civil engineering at the National University of Singapore. After finishing his master's degree, he joined the Soil and Foundation Pte. Ltd. of Singapore where he served as a civil engineer for about two years.

Jian came to the United States in 2006. He joined the Ph.D. program of the materials group at the University of Florida and worked as a graduate research assistant with his doctoral advisor, Dr. Reynaldo Roque. After completing his Ph.D., he plans to work in academia, government agencies, or private companies in civil engineering.